UNIVERSIDAD MICHOACANA DE SAN NICOLÁS DE HIDALGO

FACULTY OF ELECTRICAL ENGINEERING
DIVISION OF GRADUATED STUDIES

Power Conditioning Applications Through Nonlinear Optimal and Robust Control

THESIS

Presented to obtain the degree of

DOCTOR OF SCIENCE IN ELECTRICAL ENGINEERING

by

Serafin Ramos Paz

Dr. Fernando Ornelas Tellez
Thesis Advisor

Dr. J. Jesús Rico Melgoza
Co-Advisor

Morelia Michoacán, April 2022

POWER CONDITIONING APPLICATIONS THROUGH NONLINEAR OPTIMAL AND ROBUST CONTROL

Los Miembros del Jurado de Examen de Grado aprueban la **Tesis de Doctorado en Ciencias en Ingeniería Eléctrica, Opción en Sistemas de Control** de **Serafín Ramos Paz.**

Dr. J. Aurelio Medina Rios
Presidente del Jurado

Dr. Fernando Ornelas Téllez
Director de Tesis

Dr. J. Jesús Rico Melgoza
Co-director

J. Jesús Rico Melgoza

Dr. Roberto Tapia Sánchez
Vocal

Dr. Manuel Madrigal Martínez
Revisor Externo (ITM)

Dr. Roberto Tapia Sánchez
Jefe de la División de Estudios de Posgrado de la Facultad de Ingeniería Eléctrica. UMSNH
(Por reconocimiento de firmas)

UNIVERSIDAD MICHOACANA DE SAN NICOLÁS DE HIDALGO
Marzo 2022

Power Conditioning Applications Through Nonlinear Optimal and Robust Control

Thesis

Presented to obtain the degree of

DOCTOR OF SCIENCE IN ELECTRICAL ENGINEERING

by

Serafin Ramos Paz

Dr. Fernando Ornelas Téllez

Thesis Advisor

Dr. J. Jesús Rico Melgoza

Thesis Co-Advisor

Universidad Michoacana de San Nicolás de Hidalgo
Faculty of Electrical Engineering
Morelia, Michoacán, México

To my parents Antonio Ramos Yépez and Elsa Mirella Paz Garibay

To my wife Arancha Zamudio Pedraza

For their endless love, support and encouragement.

To Pbro. Dr. Manuel Gonzalez Cruz†

der mich vom Himmel segnet ...

Acknowledgements

I would like to express my sincere gratitude to my thesis advisors Dr. Fernando Ornelas Tellez and Dr. J. Jesús Rico Melgoza, who have left an invaluable mark on my professional career for their motivation and immense knowledge.

I would like to express my gratitude to Dr. J. Aurelio Medina Rios, Dr. Roberto Tapia Sanchez, and Dr. Manuel Madrigal Martinez for their valuable comments, suggestions, and observations to enhance this work, and to my graduate studies professor at the DEP-FIE Dr. Juan Anzurez Marín.

I would like to express my gratitude to my professors from Tecnológico de Monterrey: Msc. Miguel Angel García Ruiz, Msc. Rubén Belmonte Izquierdo, Msc. Daniel Barriga Flores, Msc. Christian David Schindler, Dr. Rosalino Rodriguez Calderon, Prof. Frank Donald Stonehouse and at last but not the least to Dr. Salvador Gonzalez Garcia, who introduced me to the control theory.

My gratitude and admiration to my father Eng. Antonio Ramos Yépez, for his technical contributions to this research.

My gratitude to my mother Elsa Mirella Paz Garibay, for his love, encouragement, example, and motivation.

I would like to thank my wife Arancha for his love, patience, support, and encouragement.

Special Thanks to Dr. Antonio Ramos Paz, for his example, motivation and encouragement.

I would like to thank my sisters Beatriz Ramos Paz, Elsa Mireya Ramos Paz, and Celia Maria Ramos Paz for supporting me throughout my studies and in my life in general.

To all my nephews: Elsa Mirella and Rafael García Ramos, Beatriz and Rodolfo Gómez Ramos and Anna Luisa and Celina Aguilera Ramos.

This research as well as my Doctoral studies were funded by the Mexican Government CONACYT.

Abstract

The electrical power grid is in constant evolution due to the increase in power electronics-based devices, the high-frequency switching of nonlinear loads, and the inverter interfaced renewable power generation systems. This power grid transformation gives rise to new electrical power grid architectures such as the so-called microgrids, which require robust and reliable control schemes to guarantee voltage-frequency regulation and power quality. In this sense, the nonlinear optimal control is presented as a control scheme capable of achieving the desired objectives and, at the same time, optimizing a given performance index, proving to be effective in tracking fast time-varying reference signals in power electronics applications. Additionally, the sliding mode control provides the control scheme with robust properties capable of rejecting external disturbances and parametric uncertainties.

This thesis presents nonlinear optimal and robust control strategies applied for local microgrid controllers and power conditioning applications. On the one hand, concerning the local microgrid control, the microgrid's operation cases during interconnection and isolation mode are considered, including an energy storage system based on supercapacitors. The proposed control scheme can regulate the microgrid voltage and frequency during the isolated mode and the power-sharing between the main utility grid during the grid-connected mode through a nonlinear optimal control strategy. On the other hand, concerning power conditioning applications. The design of nonlinear optimal and robust control algorithms is presented where a nested control strategy based on nonlinear optimal tracking control and super-twisting sliding modes is applied to power electronic converters to provide ancillary services to the electrical power grid in terms of harmonic distortion compensation, voltage regulation, and power factor correction. In addition to the design of the control algorithms, the design of an online fast-convergent harmonic estimator with a decentralized structure is presented that, together with the control schemes proposed in this thesis, allows the dynamic suppression of harmonics and interharmonics that distort the current waveform in a node of the electrical power grid. Simulation and Hardware in the Loop results demonstrate the effectiveness of the control schemes and the harmonic estimator proposed in this thesis.

Resumen

La red eléctrica está en constante evolución debido al aumento de dispositivos basados en electrónica de potencia, la alta frecuencia de conmutación de cargas no lineales y los sistemas de generación basados en energías renovables con interfaz de inversor. Esta transformación de la red eléctrica da lugar a nuevas arquitecturas de redes eléctricas como las denominadas microrredes, que requieren de esquemas de control robustos y fiables para garantizar la regulación de voltaje, frecuencia y la calidad de la energía eléctrica. En este sentido, el control óptimo no lineal se presenta como un esquema de control capaz de lograr los objetivos deseados y, al mismo tiempo, optimizar un índice de desempeño dado, demostrando ser efectivo en el seguimiento de señales de referencia rápidas variantes en el tiempo en aplicaciones de electrónica de potencia. Además, el control por modos deslizantes proporciona al esquema de control propiedades de robustez, lo que permite al sistema de control rechazar perturbaciones externas e incertidumbres paramétricas.

Esta tesis presenta estrategias de control óptimo no lineal y robusto aplicadas a controladores locales de microrredes y aplicaciones de acondicionamiento de potencia. Por un lado, en lo que respecta a los controles locales de microrredes, se consideran los casos de operación de la microrred en modo de interconexión y aislamiento, incluyendo un sistema de almacenamiento de energía basado en supercapacitores. El esquema de control propuesto permite regular el voltaje y la frecuencia de la microrred durante el modo aislado y el intercambio de energía entre la red eléctrica principal durante el modo conectado a la red a través de una estrategia de control óptimo no lineal. Por otro lado, en lo que respecta a las aplicaciones de acondicionamiento de potencia. Se presenta el diseño de algoritmos de control óptimos no lineales y robustos donde se aplica una estrategia de control anidado basada en control de seguimiento óptimo no lineal y modos deslizantes de super-twisting a convertidores electrónicos de potencia para proporcionar servicios auxiliares a la red eléctrica en términos de compensación de distorsión armónica, regulación de voltaje y corrección del factor de potencia. Además del diseño de los algoritmos de control, se presenta el diseño de un estimador de armónicos de convergencia rápida en línea con estructura descentralizada que, junto con los esquemas de control propuestos en esta tesis, permite la supresión dinámica de armónicos e interarmónicos que distorsionan la forma de onda de corriente en un nodo de la red eléctrica. Los resultados de Simulación y Hardware in the Loop demuestran la efectividad de los esquemas de control y el estimador armónico propuesto en esta tesis.

Palabras clave: Acondicionamiento de potencia, armónicos, calidad de la energía, control óptimo, estimación.

Contents

List of Figures

Acronyms

AC Alternating current

APF Active power filter

BSES Backup stored energy system

CICV Constant current-constant voltage

DC Direct current

DFACTS Distribution flexible AC transmission system

DG Distributed generation

DVR Dynamic voltage restorer

EMS Energy management system

FET Field effect transistor

GTO Gate turn-off thyristor

HIL Hardware in the loop

HJB Hamilton-Jacobi-Bellman equation

IGCT Integrated gate commutated thyristor

MPPT Maximum power point tracking

NPCAEE Normalized percentage cumulative amplitude estimator error

NPCAEE Normalized percentage cumulative frequency estimator error

PCC Point of common coupling

PID Proportional-integral-derivative controller

PLL Phase locked loop

PQ Active-reactive power control

PSO Particle swarm optimization

PWM Pulse width modulation

RES Renewable energy systems

SC Supercapacitor

SDRE State-Dependent-Riccati-Equation

SMC Sliding mode control

SOC State of charge

SOSM Second order sliding mode

STA Super-twisting algorithm

SVR Static voltage regulator

TA Twisting algorithm

THD Total harmonic distortion

UPQC Unified power quality conditioner

UPS Uninterruptible power supply

VCVSI Voltage-controlled voltage-source inverter

VF Voltage-frequency control

VSC Voltage source converter

VSC Variable structure Control

Symbols

A amplitude

α angular frequency

ω microgrid's frequency

θ phase angle

σ sliding variable

ϵ tracking error

Φ integrators vector

J performance index

C capacitance

L inductance

r tracking reference

R resistance

S apparent power

P_a active power

Q_r reactive power

$f(x)$ nonlinear function

s measured signal

$\hat{s}$ estimated signal

t time

$\mathcal{S}$ sliding manifold

$\mathbb{T}$ Park's transformation matrix

T period of the signal

$\mathcal{T}$ temperature of the supercapacitor

u^* optimal control law

x state vector

X reactance

List of Publications

Indexed by Journal Citation Reports (JCR)

- S. Ramos-Paz, F. Ornelas-Tellez and J.J. Rico-Melgoza. “Power Quality Enhancement Through Ancillary Services Provided by Power Electronic Converters” in Electric Power System Research, Volume 209, 2022, 107934, ISSN 0378-7796, https://doi.org/10.1016/j.epsr.2022.107934.
- S. Ramos-Paz, F. Ornelas-Tellez and J.J. Rico-Melgoza. “Dynamic Harmonics-Interharmonics Identification and Compensation Through Optimal Control of a Power Conditioning Application” in Electrical Engineering Spinger. 2021. (Under Review).
- F. Ornelas-Tellez, J.J. Rico-Melgoza, R. Morfin-Magana and S. Ramos-Paz, “Optimal Dynamic Harmonic Extraction and Suppression in Power Conditioning Applications” in IEEE Transactions on Industrial Electronics, vol. 67 no. 9, pp 7909-7918, sept. 2020. doi: 10.1109/TIE.2019.2944059.

Patents

- F. Ornelas-Tellez, J. Jesus Rico-Melgoza, S. Ramos-Paz y R. Morfin Magana. “Método Para la Estimación y Supresión Dinámica y Óptima de Armónicos para Aplicaciones Industriales" MX/a/2019/001740.

International Conference Publications

- S. Ramos-Paz, F.Ornelas-Tellez, J.J. Rico-Melgoza, “Dynamic Power Factor Correction Through Power Electronic Converters Optimal Control", 2021 North American Power Symposium (NAPS), 2021, Texas A&M University, College Station, Texas USA.
- S. Ramos-Paz, F. Ornelas-Tellez, J. J. Rico-Melgoza and A. Ramos-Yepez, “A Robust Control Strategy for Voltage Regulation in Electrical Distribution Networks by Means of Power Electronic Converters," 2020 IEEE International Autumn Meeting on Power, Electronics and Computing (ROPEC), 2020, pp. 1-5, doi: 10.1109/ROPEC50909.2020.9258689
- S. Ramos-Paz, F. Ornelas-Tellez, J.J. Rico-Melgoza and E. Sanchez, “Power Quality Improvement Through Distribute Generation Based on Renewable Energy", Clemson University Power System Conference, Clemson, South Carolina, USA, 2020.

- S. Ramos-Paz, F. Ornelas-Tellez and J. J. Rico-Melgoza, “Robust Nonlinear Optimal Control for Voltage-Frequency and Active-Reactive Power Regulation in Microgrids", 2019 North American Power Symposium (NAPS), 2019, pp. 1-6, doi: 10.1109/NAPS46351.2019.9000228.
- E. Rodriguez-Lopez, S. Ramos-Paz, J. J. Rico-Melgoza and F. Ornelas-Tellez, “Parametric Passive-Filter optimization Based on the Determinant Decision Diagram", 2019 IEEE International Autumn Meeting on Power, Electronics and Computing (ROPEC), 2019, pp. 1-6, doi: 10.1109/ROPEC48299.2019.9057047.
- D. Gonzalez-Lopez, S. Ramos-Paz, C. Cordova-Aguilar and F. Ornelas-Tellez, “Nonlinear Optimal Control for a Grid-Connected Photovoltaic System," 2018 IEEE International Autumn Meeting on Power, Electronics and Computing (ROPEC), 2018, pp. 1-7, doi: 10.1109/ROPEC.2018.8661472.

Chapter 1

Introduction

1.1 Motivation

The tremendous technological advances to which we have access today are nothing more than the result of a historical process of incremental and disruptive innovations, motivated by the constant interest of humankind in solving the problems that have arisen at specific historical moments as well as the curiosity and capacity for innovation of the great scientist over the time. The ideas of Thomas Edison (1847-1931) and Nikola Tesla (1856-1943), together with each of the great scientists who preceded them, allowed the massive electrification of large cities at the beginning of the 20th century through the ability to efficiently transport electric power from generation sites to load centers, based on the principle of the use of alternating current (AC) and large synchronous generators [Carlson, 2015]. However, the accelerated population increase demanded more significant amounts of energy, for which cheap and easily accessible generation sources were required, which led to the proliferation of fossil fuels usage for the generation of electrical energy. However, this has caused significant levels of pollution that are unbearable for the world [Gates, 2021, Smil, 2017]. The 2015 Paris agreement of COP21[1] laid the foundations for limiting global warming through agreements adopted by 196 countries. Allowing the implementation of energy policies that promote power generation strategies based on renewable energy. Nonetheless, using these energies has required adapting new technologies to existing electrical power grids, representing a technological challenge that opens the doors to new developments and research.

The first electrical power generation systems based on renewable energies were made through distributed generation systems isolated from the electrical power grid due to technical or economic reasons, mainly in remote areas without access to transmission or distribution lines [Bakke, 2017]. This led to on-site generation schemes, mainly through solar panels and wind generators. This gave rise to a new concept known as microgrids [Hatziargyriou, 2014]. However, the significant decrease in costs associated with the technology necessary for implementing microgrids has encouraged the integration of

[1] *2015 United Nations Climate Change Conference (Paris Agreement).*

large-scale distributed generation systems with the electrical power grid. This fact is causing the traditional electrical power grid to evolve, integrating different elements such as innovative control algorithms, measurement systems, telecommunications, and energy storage devices into a smart grid [Keyhani, 2019]. However, several technical challenges must be overcome concerning the design, operation, and reliability of modern electrical power grids, such as: a) the reliable and economical operation of microgrids with high penetration levels of generation sources based on renewable energy [ESM, 2022]; b) the development of new voltage and frequency control schemes to deal with the increase in power electronics-interfaced distributed generation systems; and c) schedule and dispatch of units under uncertain supply or demand and the determination of appropriate levels of reserves. In the same way, the integration of nonlinear loads and devices based on power electronics, such as electric vehicle charging stations, switched sources, uninterruptible power supply systems, or the operation of the inverter-interfaced renewable-based power generation systems, generates a series of issues in terms of power quality. Such as harmonic distortion, voltage deviations, and inadequate power factor, causing severe problems in the electrical power grid such as overloading of conductors, overheating transformers, untimely tripping of protection systems, or overloading of power factor correction capacitors, among others. However, these problems open the doors to new technological developments, even by using the same renewable energies or the technology associated with them, such as the flexibility offered by the power electronic converters to compensate for diverse power quality issues. The Development these emerging technologies is of interest to achieve the objectives proposed in the energy policies worldwide and provide sustainable energy through a robust electrical power grid, which is an open issue that requires research. In this sense, modern electrical power grids must be provided with reliable and robust control algorithms to successfully integrate the distributed generation sources such as wind, solar, hydrogen, and other renewable resources and to provide ancillary services capable of guaranteeing the power quality of the electrical grid.

1.2 Problem Statement

The increase in the integration of renewable-based power generation sources and the interconnection of nonlinear loads to the electrical power grid has focused the efforts of the scientific community to find technical solutions to adapt the existing electrical power grid to the new prevailing needs. Much effort has been made; however, the complex problems related to the dynamics of the electrical power grid and power electronic converters require innovative solutions capable of efficiently solving power quality problems. Modern electrical power grids must be provided with robust and reliable control algorithms to integrate electrical power generation and storage devices based on

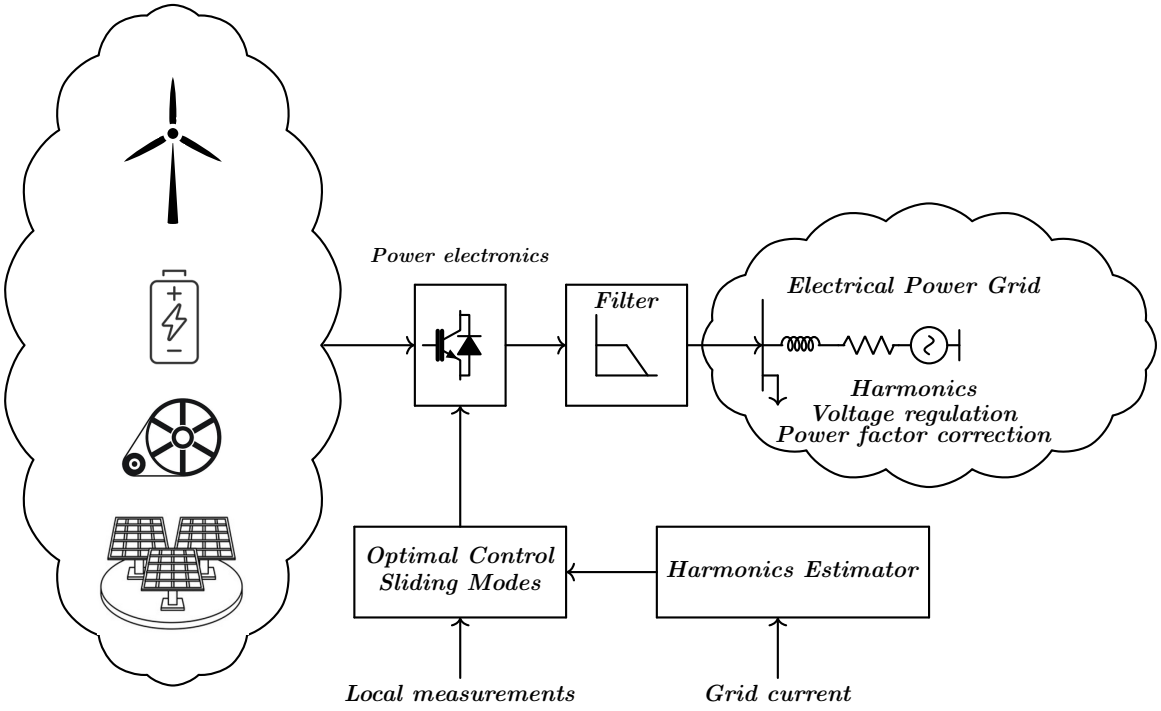

Figure 1.1: Proposed microgrid and power conditioning control scheme.

large-scale renewable energies. Besides, to compensate potential problems in terms of power quality derived from the interconnection of nonlinear loads and the fluctuation in the renewable-based power generation. Traditionally, the operation and control of microgrids use linear controllers, which have limited regions of operation and ignore the nonlinear nature of the power electronic converters and microgrid dynamics. Therefore, in this thesis, the use of nonlinear optimal and robust control strategies applied to the microgrid primary control level through electronic power converters is proposed to deal with the microgrid nonlinear dynamics with possible parametric uncertainties and external disturbances. With the proposed nonlinear optimal and robust control schemes, this thesis aims to control the electrical variables of voltage, frequency, and power exchange during the different microgrid operating modes and provide ancillary services by adding new operational features to the existing infrastructure of the electronic power converters, and thus solve problems in terms of power quality, such as voltage compensation, power factor correction and harmonic distortion suppression.

Figure 1.1 shows this thesis proposal for the use of power electronic converters through appropriate control strategies for microgrid control and power conditioning applications in the electrical power grid.

1.3 Literature review

1.3.1. Historical Background Nonlinear Control

During the 1950s and 1960s, aerospace engineering applications greatly stimulated the development of optimal control theory, where the objective was to drive the system states so that some defined cost function was minimized. Mathematicians in the United States and the Soviet Union extensively studied the time-optimal control problem. In the period from 1953 to 1957, Bellman, Gamkrelidze, Krasovskii, and La Salle developed the basic theory of minimum time problems and presented results concerning the existence and uniqueness, and general properties of time-optimal control [Athans, 2007]. Nonetheless, the classical calculus of variations could not handle the problematic constraints imposed by an optimal control problem, this difficulty led Pontriagin to establish his well-known *maximum principle* [Geering, 2007], and then Boltyanskii and Gamkrelidze gave proof of it. The dynamic programming method [Bertsekas, 2005] developed by Bellman around 1953-1957 may be viewed as an outgrowth of the Hamilton-Jacobi approach to variational problems and then, its use was extended to control problems. The optimal control problem can be solved by using the maximum principle of Pontriagin and the dynamic programming developed by Bellman, which leads to a set of nonlinear partial differential equations named the Hamilton-Jacobi-Bellman (HJB). The solution of the HJB is well-established in solving the optimal control problem for linear systems whose solution results in the Riccati equation. However, the optimal control problem solution applied to nonlinear systems is an open issue. In this sense, the well-known State-Dependent Riccati Equation (SDRE) [Cloutier, 1997] became very popular during the first decade of the twentieth century. The SDRE provides a very effective algorithm for synthesizing nonlinear feedback controllers. Pearson first proposed this method in 1962 and then was expanded by Wernli and Cook in 1975 and later by Mracek, Cloutier, and D'Souza in 1998. The method entails factorizing the nonlinear dynamics into the state vector producing a matrix-valued function that depends on the state itself, then, by doing so, the SDRE fully captures the system nonlinearities, transforming the nonlinear system into a linear-like representation having state-dependent coefficients matrices and minimizing a nonlinear performance index with a quadratic structure. Cloutier, D'Souza, and Mracek's work initiated an increasing use of the SDRE to solve nonlinear optimal control problems, including autopilot designs, guidance control [Sayadi et al., 2018], satellite and spacecraft control process control [Xin and Pan, 2012], or even control of artificial pancreas [Romero-Aragon et al., 2014]. Recently, in the work presented by Ornelas et al. [Ornelas-Tellez et al., 2014], a modification to the nonlinear optimal control scheme is proposed to solve the problem of time-varying reference tracking, which is the theoretical basis on which this thesis is based from the point of view of nonlinear optimal control.

Nonlinear optimal control schemes can be combined with various control techniques to provide the control algorithm with robustness elements, as shown in [Fridman, 2014, Ramos-Paz et al., 2017]. In this sense, sliding mode control is presented as an interesting alternative for the design of robust control algorithms in combination with optimal control. Sliding mode controllers (SMC) [Perruquetti and Barbot, 2002] were developed in the Soviet Union in the framework of variable structure control (VSC). This nonlinear method alters the dynamics of a nonlinear system by the application of switching control [Fridman, 2014]. In the framework of VSC, it was understood that if the controllers are ensuring finite-time arrival to some surface on both sides of the surface, the solution should slide on the surface if it is supposed that the frequency of the switching is infinite. The history of variable structure control dates from the early 50s. By 1980 the significant contributions of classical sliding mode control theory had been made by Prof, Utkin's. By the early '80s, the scientific control community understood that the main disadvantage of SMC was the so-called chattering effect caused by unmodeled dynamics that increase the relative degree of the system. In order to overcome the chattering-effect[2], different ideas appear to improve the performance of SM controllers, such as the second-order sliding mode (SOSM), a concept introduced by Prof. Levant. The simplest SOSM is the so-called twisting algorithm (TA) designed for systems with relative degree two. Nonetheless, the TA algorithm collapses the dynamics of such systems at the origin [Ferrara, 2017]. At the end of the 1980s, generating a continuous control signal without derivatives was the main issue. The super-twisting algorithm (STA) was presented in the early '90s in [Levant, 1993], providing a continuous control signal, generated without using the derivative of the sliding variable, and capable of maintaining a SOSM for a first-order system with Lipschitz[3] bounded uncertainties/disturbances [Khalil, 2002].

1.3.2. Microgrid Control State of the Art

A microgrid can be regarded as a controlled entity within the power system that can be operated as a single aggregated load or generator, also as a small source of power, or as an ancillary service supporting the electrical power grid [Hatziargyriou, 2014]. Microgrids are used in order to facilitate the integration of renewable energy resources (i.e., wind energy, photovoltaic, fuel cells, hydrogen, etc.) through distributed generators (DG). The idea behind the microgrid is that it can be operated based on autonomous subsystems composed of small areas with dedicated or local control schemes [Hatziargyriou, 2014]. Microgrids can be operated in two different modes

[2] *The term "chattering" describes the phenomenon of finite-frequency, finite-amplitude oscillations appearing in many sliding mode implementations. These oscillations are caused by high-frequency switching of a sliding mode controller, exciting unmodeled dynamics in the closed-loop.*

[3] *The Lipschitz condition is defined whereby* $f(t,x)$ *satisfies the inequality* $||f(t,x) - f(t,y)|| \leq L||x-y||$ $\forall(t,x)$ *and* (t,x) *in some neighborhood* (t_0, x_0) *[Khalil, 2002].*

[Bidram et al., 2017]: grid-connected or isolated mode. During each operation mode, the microgrid achieves different control objectives, where the main variables used to control are the voltage, frequency, and the active and reactive power-sharing. On the one hand, during the grid-connected operation mode, the voltage and frequency at the common coupling point (PCC) are dominantly imposed by the host grid. Therefore, the microgrid distributed generation nodes can be employed as real/reactive power sources [Hatziargyriou, 2014], where the control objective is to regulate the instantaneous real and reactive power delivered by the voltage source converter (VSC) at the PCC, or as well the microgrid can be used for power conditioning applications, providing ancillary services such as power factor correction, voltage control or harmonics suppression. This topic will be discussed later in this thesis in the Chapter 4. On the other hand, the microgrid operates as an independent entity during the isolating or stand-alone mode of operation, and the host power grid no longer supports the voltage and frequency. In this sense, the main control objective is the voltage and frequency regulation, which is a prerequisite for the economical and efficient operation of the microgrid, as well as for the correct operation of electrical devices and loads connected to the power grid and the compliance with regulations imposed by the operators of electrical power systems. Therefore, microgrids must be integrated with robust control schemes, capable of compensating for deviations of system voltage and nominal frequency in the presence of uncertainties in the load and distributed generation.

Control Objectives in AC Microgrids

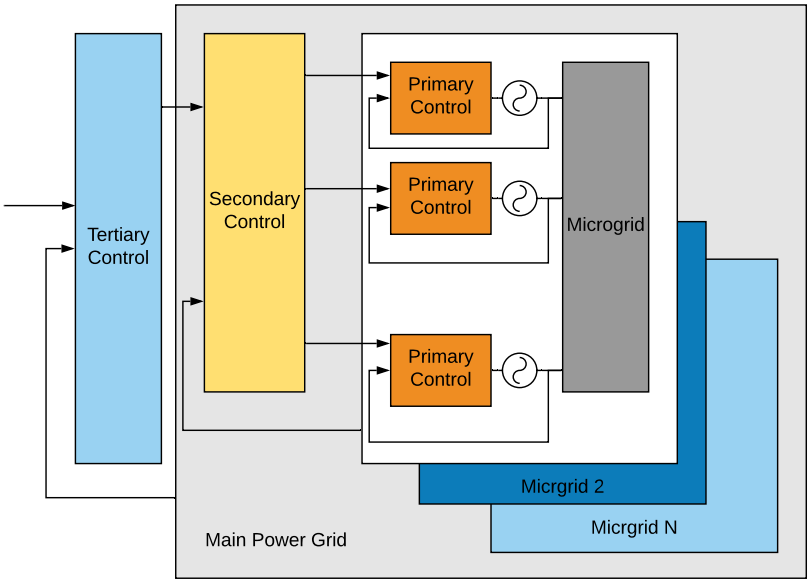

Figure 1.2: Microgrid hierarchical control structure.

In either of the two different microgrid operative modes, grid-connected or stand-alone mode (isolated), the main microgrid control objectives [Bidram et al., 2017] are

the following:

- Voltage and frequency regulation for both operative modes.
- Power flow control between the microgrid and the host grid.
- Microgrid resynchronization with the main grid.
- Proper load sharing and distributed generation coordination.
- Optimization of the microgrid operating cost.

These objectives are achieved at different time scales through a hierarchical control structure based on mainly three different control levels, namely primary, secondary and tertiary control as seen in [Bidram et al., 2017],[Olivares et al., 2014]. The general microgrid hierarchical control structure is depicted in Figure 1.2.

Primary control

The primary control, also known as local or internal control, operates on the fastest time scale and requires the fastest control response. Its main objective is to guarantee the voltage and frequency regulation when the microgrid operates in an isolation mode and the power-sharing during grid-tied operation. The primary control is based on local measurements and does not require communication links. It is designed to accomplish the following control objectives [Hatziargyriou, 2014]:

- To stabilize the voltage and frequency.
- To offer plug-and-play capabilities for the distributed generation and properly active and reactive power-sharing with the main utility grid.

The primary control provides the reference signals for the voltage and current control loops. These inner control loops are commonly referred to as zero-level control; the zero-level control is generally implemented in either active/reactive power control (PQ) or voltage-frequency control mode (VF) [Fan, 2017]. While in the PQ mode, the distributed generation node active and reactive power output is regulated on the predetermined setpoints. By contrast, the distributed generation node operates as a voltage-controlled voltage source-inverter (VCVSI) during the voltage control mode. The primary control determines the voltage reference, conventionally via drop characteristics [Fan, 2017]. It is important to highlight that the power quality of small-scale isolated systems is of particular importance due to the presence of nonlinear and unbalanced loads and the low inertia of the microgrid. Considering a renewable-based microgrid, during the islanded operation mode, without a robust and effective control strategy, the microgrid's voltage and frequency may experience high fluctuations and instabilities due to the high penetration of intermittent renewable energy. In addition, the power electronics along

with the electrical power grid represent a highly nonlinear behavior. In this sense, it is necessary to apply nonlinear and robust control schemes to deal with these systems nonlinear and uncertain nature.

Secondary Control

While the primary control is implemented locally at each independent distributed generator, the secondary control is a centralized controller which restores the microgrid voltage and frequency and compensates for the deviations caused by the primary control. This control level has a slower time response than the primary control. Secondary control is also referred to as the microgrid energy management system (EMS) [Olivares et al., 2014] and is responsible for the reliable and economical operation of the microgrid at either grid-connected or islanded mode. The main objective of the EMS consists of finding the optimal value for the unit commitment and economic dispatch of the DGs. Primary control may cause frequency and voltage deviations even in a steady state. Thus the secondary controller restores the microgrid voltage and frequency and compensates for deviations caused by the primary control loop.

Tertiary Control

The tertiary control is responsible for the microgrid supervision, generation, and forecast. This control level, generally operates on a slow time scale and considers the economic concerns for the optimal operation of the microgrid, and manages the power flow between the microgrid and the main power grid depending on the requirements of the host power grid. For instance, the overall reactive power of a power grid composed of several distributed generation nodes within a microgrid is accomplished by proper coordination through a tertiary control approach. Tertiary control can be considered as part of the main grid, and not the microgrid itself [Olivares et al., 2014]. Therefore this control level will not be discussed further in this thesis.

Microgrid Energy Storage Systems

The energy storage systems [Díaz-González et al., 2016] are often needed with the RES integration in order to buffer the generated electrical power, as well as compliance with the regulations and requirements imposed by the operators of the electrical power grid, as seen in [Winfield et al., 2018]. Therefore energy storage devices, together with power electronic converters, are used as ancillary devices which support the electrical power grid in terms of compensation of voltage fluctuations, isolation events, or energy arbitrage (store energy to be used when the price is at a premium). Nowadays, rechargeable batteries, especially lithium-ion batteries [lit, 2018], are currently a popular option as energy storage devices due to their high energy density and their large

number of charging cycles. Nonetheless, they have limits of relatively low power density and relatively high internal resistance, which could heavily curtail the power delivery capability under large current loading [Díaz-González et al., 2016]. On the other hand, supercapacitors (SC) [Zhang et al., 2018a], also known as ultra-capacitors or double-layer capacitors, are being actively studied and envisaged as a promising energy storage technology due to their outstanding characteristics, as they are their high power density, and a high degree of recyclability as well as their capability to be charged and discharged with high current. It is important to highlight that supercapacitors operate under an electrostatic principle rather than a chemical principle like batteries do. In recent years, supercapacitors have been used in power conversion applications such as controlled electric drives, active power filters, power conditioners, and uninterruptible power supplies (UPS). In recent works, supercapacitors have been employed as the energy storage devices that can be fully charged/discharged within a few seconds, connected to the power conversion system via interfacing bidirectional DC/DC power electronics converters [Sharkh et al., 2014]. In related works, the use of bidirectional DC/DC power electronic converters based on supercapacitors has been reported as seen in [Verma et al., 2011, Grbovic et al., 2010] and [Cornea et al., 2017], where a bidirectional hybrid DC/DC converter based on switched capacitor cells is presented, with a controller design based on the K factor control method in order to regulate the PWM control signal. However, in previous works, the use of linear PI type controllers is predominant, and as a consequence, the regions of operation of the linear controller over a highly nonlinear system are limited. In this sense, due to the highly nonlinear behavior of the power electronic converters used to interface the renewable energy resources and energy storage devices, advanced nonlinear control techniques must be employed, as they are the nonlinear optimal and robust controllers described in this thesis.

1.3.3. Power Conditioning Applications

Power conditioning [Akagi, 2007] is a broad term, which includes all services required by transmission or distribution system operators to enable them to maintain the integrity and stability of the transmission or distribution system as well as the power-quality [Hatziargyriou, 2014]. Modern electrical power grid operators and end-users are becoming more concerned about the power quality issues, such as voltage regulation, harmonic distortion, or power factor [Dugan, 2012], due to the compliance of standards and grid codes requirements [619, 2012],[853, 2018] in addition to the increased use of waveform-sensitive equipment. Traditionally, the different problems associated with power quality have required specific solutions based on different types of infrastructure. In the case of harmonic suppression, active power filters [Ornelas-Tellez et al., 2020] have been widely implemented, for voltage regulation, solutions based on custom power devices [Moghbel et al., 2018] such as dynamic voltage restorers (DVR)

[Rauf and Khadkikar, 2015], static voltage regulators (SVR) or backup store energy systems (BSES) [Housseini et al., 2018] are used, or in the case of power factor correction, the installation of capacitor banks or synchronous condensers are required [Qin et al., 2019]. Nowadays, engineers deal with these power quality issues by using a systemic approach rather than handling individual problems. The constant advances in the integration of distributed energy resources, mainly based on renewables, have brought a series of benefits to both users and operators of electrical power grids. In addition, one of the main characteristics of integrating distributed energy resources is that they are connected to the main utility grid through power electronic converters, providing a wide range of functions. Not only for supplying electrical power or the formation of microgrids but also for power conditioning applications to compensate a series of problems in terms of power quality at a power system node, such as voltage regulation, harmonics compensation, or power factor correction [Hatziargyriou, 2014]. In this sense, power conditioners are based on leading-edge power electronics technology, including power conversion systems and control theory. Therefore, in this thesis, a novel control scheme to add new operational features to the available infrastructure of the DC/AC power electronic converters is presented. Then, through proper control algorithms, it is possible to change the converter control objective when required, depending on the end-user requirements providing ancillary services to the electrical power grid to enhance the power quality.

Harmonics Estimation and Suppression

The proliferation of nonlinear loads has spurred interest in research on various power quality problems related to harmonic pollution in electrical power systems. The reduction of the voltage and current waveform distortion to acceptable levels is a problem in electrical power systems, which has grown concerns due to the increasing use of sensitive waveform equipment [Arrillaga and Watson, 2004] and the requirements of a high-quality level of electric power imposed by the utility grid operators and grid codes. Therefore, to improve the electrical power quality, modern electrical power grids must be equipped with the appropriate controls and devices capable of guaranteeing and fulfilling the power quality standards (i.e., IEEE-519-1992 [std, 1993], or IEC 61000-3, Limits for Harmonic Current Emissions [I.E. Commission, 1998], among others) and to avoid adverse power quality phenomena such as waveform distortion. In this sense, passive filters [Rasol Jannesar et al., 2019], static compensators [Wang et al., 2015], and active power line conditioners [Williams and Hoft, 1991] have been widely used to compensate the adverse harmonic effects causing waveform distortion. This thesis centers on the harmonic identification and the control of active power filters (APF) [Yeetum and Kinnares, 2019], which are power electronic equipment capable of compensating the harmonic distortion and thus enhancing the power quality. The

basic principle of a power electronic converter used for power conditioning applications such as harmonic suppression is to generate the necessary current to compensate the harmonics produced by nonlinear loads such as the power electronics required in the renewable sources integration [Yang et al., 2015] (i.e., wind parks), electric cars charging stations [Khan et al., 2018], among other harmonic sources.

Different harmonic identification schemes have been widely reported in the literature. On the one hand, in the frequency domain, it is possible to highlight the use of the Fast Fourier Transform [Rao, 2010] and the Discrete Fourier Transform based methods [Hwang and Liu, 2014]. Nonetheless, one of the significant limitations of these methods is the required computational burden, which depends on the number of samples considered in a time window and the requirement of a complete cycle of a periodical signal to conduct the analysis. A different approach that also performs the harmonics estimation, is the so-called instantaneous power theory of PQ theory [Akagi, 2007]; However, this approach has been demonstrated to be effective under balanced three-phase signals and presenting challenges for the unbalanced case. Also, a common characteristic of the aforementioned methods is the usage of a moving window of past values, which causes time-delays within the harmonic estimation, making these algorithms not feasible for real-time feedback control application (such as in AFP control) where a dynamic operation of the system is considered rather than a steady-state condition. On the other hand, various online harmonic estimators have been reported, based on different estimation techniques such as adaptive Taylor-based band-pass filter [Radulović et al., 2020], where the harmonic parameters are iteratively estimated through a dynamic phasor model. Nonetheless, the strategy does not suppress the effects of interharmonics completely. Moreover, different estimation algorithms have been widely reported in the literature, such as phase-locked-loop algorithms, including a method for addressing the DC components and notch filters, as seen in [Karimi-Ghartemani et al., 2012]. The continuous-time online adapted frequency-locked loop using a third-order generalized integrator is presented in [Fedele and Ferrise, 2014], while [Chen et al., 2018] reports an integral observer to detect the fundamental and interharmonic components. Also, an approach using Kalman filtering and a state-space model to estimate the frequency of harmonic signals is presented in [Hajimolahoseini et al., 2008], and different observer-based approaches based on the immersion and invariance technique considering the case of multiple frequencies are described in [Carnevale and Astolfi, 2011]. Each of the works mentioned above provides desirable characteristics for harmonic estimation, such as the online implementation, inter-harmonics and frequency estimation, and signal representation in a state-space model. However, the previous works do not present a solution that combines all the characteristics mentioned as this thesis objective. In addition, interesting solutions for the harmonic and interharmonic processing are reported in [Karimi-Ghartemani and Ziarani, 2004, Mojiri et al., 2010]. However, these works are fo-

cused on the detection of harmonics and interharmonics rather than on an identification and suppression scheme in conjunction with control algorithms. These tasks together are the objective of this work. In [Ornelas-Tellez et al., 2019], an optimal harmonic estimator is presented, characterized by the online harmonic content computation of a time-varying signal, which is based on a Kalman-Bucy filter through considering that the frequency is a priori known, and as a result, calculating the amplitudes and phases; in the referred work, the case of interharmonics and frequency estimation is not addressed. In contrast, to [Ornelas-Tellez et al., 2019], this research aims to identify three components: frequencies, amplitudes, and phases of the harmonic and inter harmonic content presented in a distorted waveform, topics that as a whole are not covered in the work above.

Besides the decentralized harmonic identification, power conditioning applications must be equipped with appropriate control algorithms capable of performing tracking of time-varying reference signals, such as in the case of the harmonic reference signals profiles to be suppressed. Different control strategies for power conditioning applications have been reported such as sliding modes [Chen and Fei, 2019], model predictive control [Rameshkunar et al., 2017], or neural networks [Madtharad and Premrudeepreechacharn, 2002]. Nonetheless, this thesis centers on the use of nonlinear optimal control theory, which represents an increasingly relevant role for the synthesis of advanced control systems to determine the control actions that will cause the minimization of a given performance index [Kirk, 2004]. Among the features to be highlighted related with the proposed control method, is that optimal control laws are known to have adequate stability margins, and robustness properties [Sepulchre, 1997, Freeman, 1996, Anderson and Moore, 1990]. In addition, nonlinear optimal control applied to power electronic converters represents an efficient and proven theory capable of tracking fast time-varying reference signals, as seen in [Ornelas-Tellez et al., 2019, Pahlevaninezhad et al., 2012]. Through the proposed methodology presented in this research, it is possible to obtain a state-space model of the signal harmonic content, which can be implemented in a decentralized form, which in contrast to a centralized approach, by dividing the complex problem into simpler subsystems makes easier to tune the parameters since the model is more straightforward and smaller in dimension [Liu et al., 2018]. In addition, having a decentralized structure allows computational techniques to be applied that makes the estimator more efficient for real-time feedback control applications, such as parallel computing [Grama, 2003]. To this end, the proposed harmonic estimator is combined with a harmonic suppression scheme based on the optimal tracking control of a power electronic converter. It is essential to highlight that based on the separation principle[4] [Astrom, 2006]. It is possible to decouple the problem of optimal control and state estimation. Therefore it is reasonable to design the proposed harmonic estimator along with the nonlinear optimal controller.

[4] *The separation principle establishes that the optimal control and state estimation problem can be decoupled and independently addressed.*

Power Factor Compensation

The power factor [Alexander, 2017] is considered to be an indicator of the correct use of electrical power. According to the behavior of the power factor, the operators of the electrical power grid apply a penalty on the consumption rate, mainly for industrial consumers, as established by the electric power supplier in compliance with the grid codes. Within the main causes of a low power factor are electrical installations with a large number of motors, refrigeration and air conditioning equipment, or under-utilization of the electro-mechanical equipment installed, which are mainly inductive loads. In this sense, electric power grid users with low power factors require compensation schemes. Methods of power factor improvement include capacitor banks [Gonzalo et al., 2020], synchronous condensers [Aamir et al., 2019] or phase advancers. However, the previous methods correspond to solutions based on specific equipment to solve the power factor problem. It is important to emphasize that users, mainly of the industrial type, can experience different adverse power quality phenomena. Therefore, the use of specific devices for specific different problems can increase the cost of the necessary infrastructure. In this sense, the control scheme proposed in this work takes advantage of the already available infrastructure of the power electronic converters. Then, through proper control, algorithms allow changing the control objective of the converter if necessary. This permits the converter to participate in power factor correction when required and then change the control objective to be used for something different from supplying power to the utility grid by acting as an ancillary service for microgrids or distribution systems in terms of voltage compensation [Ramos-Paz et al.,],[Molla and Kuo, 2020], harmonics compensation [Ornelas-Tellez et al., 2020], [Zhang and Li, 2016] or in this case power factor correction. It is important to mention that the main objective of this thesis does not intend to use the power that may come from a micro source (based on renewable energy) for the only purpose of power factor correction. Therefore through proper control strategies, it is possible to achieve several control objectives within the same inverter topology, reducing the cost of additional infrastructure. Nowadays, different approaches have been developed to deal with power quality issues, including custom power devices such as the so-called unified power quality conditioner (UPQC) [Dash and Ray, 2018], which is capable of compensating harmonics and voltage variations. However, the technology mentioned above employs two voltage source inverters (VSIs) and cannot compensate the power factor. A different approach used the so-called distribution flexible alternating current transmission systems (DFACTS) [Elmetwaly et al., 2020] for power quality enhancement in isolated microgrids. Nonetheless, they are mainly based on classical PID controllers, which reduce the operational range of such devices to a limited linear region. Specific solutions for power factor correction are given in related work such as [Hashmi et al., 2020], [Mahendran et al., 2017], [Lo

et al., 2008]. However, in none of the previous works, a solution that can be scalable and combinable with the proposed solutions to other power quality problems under the same power electronics configuration is exposed.

This research proposes that through advanced control strategies, such as nonlinear optimal control and sliding mode control, additional features can be added to the power electronic converters to perform different power conditioning tasks such as voltage regulation, harmonic distortion compensation, and power factor correction. This is achieved through a nonlinear and robust control strategy that allows expanding the operating regions of the power electronic converters and the possibility of rejecting parametric or structural uncertainties in the models of microgrids for the interface of power conditioning devices.

1.4 Objectives

1.4.1. General objective:

The design of nonlinear optimal and robust controllers for local microgrid control and power conditioning applications through power electronic converters.

1.4.2. Specific objectives:

- The harmonics/interharmonics estimation.
- Harmonics suppression, voltage regulation, and power factor compensation through power electronic converters control acting as ancillary services.
- Voltage and frequency control for microgrids through nonlinear optimal and robust control.

1.5 Contributions

The original contributions of this thesis are listed as follows:

- The proposal of a novel control strategy, based on nonlinear optimal tracking control as an alternative to the classical microgrid controllers for the voltage, frequency, and power control for the isolated and grid-connected microgrid operative modes.
- The design of a nonlinear-robust control scheme, capable of compensating the voltage variations and the power factor at a power system node, using a nested control-loop strategy based on sliding modes and nonlinear optimal tracking control.

- The proposal of a novel robust control scheme for the voltage, harmonics distortion, or power factor compensation at specific instants, through DC/AC power electronic converters intending to serve as ancillary services to distribution systems or microgrids.
- The design of an n frequencies harmonic and interharmonic identification and suppression scheme which has the following characteristics: a) the harmonic identifier is implemented decentralized and then employed to synthesize an optimal feedback controller based on nonlinear optimal tracking control to dynamically suppress the harmonic content in a distorted waveform in an electrical power system through an active power filter; b) the harmonic and interharmonic identifier design is based on a fast-convergent state estimator with a state-space representation, which does not require one period of the signal, as usually required in Fourier-transform-based methods; c) the harmonic content is computed in the time-domain framework. Therefore, no additional computational burden is necessary to perform any frame transformation.

Table 1.1: Control strategies design and their usage in power conditioning applications.

Contribution	**Highlights**	**Typical applications**
Harmonics estimation and suppresion	Fast convergence; Fast frequency variations estimation; Suitable for real-time implementations; Decentralized structure; Real-time implementation.	PWM electric motor drives, PMU´s for distribution systems, power quality measurement instruments.
Nonlinear Control	Real-time implementation; Robustness against unknown system parameters;	Shunt active power filters; Voltage regulation in industrial facilities with distributed generation; Power factor correction in industrial facilities with distributed generation.

Table 1.1 summarizes the main characteristics of the power conditioning designs proposed in this research, as well as suggested potential applications.

1.6 Methodology

The methodology of this research work is the design of nonlinear optimal and robust controllers for power conditioning applications and their use in different case studies to experiment and analyze the results by considering the following topics:

1. Primary control, Inverter Output Control.
2. Voltage and frequency control.
3. Active/reactive power control.
4. Energy storage system control.
5. Ancillary services for power conditioning applications.

For the power conditioning applications control and design methodology includes the following steps:

- The Harmonics estimation and compensation assessment through a decentralized harmonic estimator and nonlinear optimal control of DC/AC power electronic converter.
- The power factor compensation assessment through nonlinear optimal control and sliding modes.
- The voltage regulation assessment through nonlinear optimal control and sliding modes.

1.7 Thesis Outline

This thesis is organized as follows.

Chapter 2 Theoretical Framework

This Chapter introduces important concepts for developing microgrid control strategies. The fundamentals of nonlinear systems, along with the nonlinear control algorithms based on sliding mode and nonlinear optimal control, are described in detail, as well as the mathematical background for signal modeling based on Fourier series is presented. Moreover, the power electronic converters modeling is described in this Chapter.

Chapter 3 Control of Distributed Energy Resources in Microgrids

This Chapter presents the design of microgrid local control strategies based on nonlinear optimal tracking control. Moreover, this chapter addresses the microgrid isolated mode and grid-connected mode control problems, considering the voltage and frequency control during an isolation event and the power-sharing during the grid-connected mode. In addition, a control scheme for an energy storage system based on supercapacitors is presented. Simulation results demonstrate the effectiveness of the proposed nonlinear

optimal tracking controller for the microgrid control objectives.

Chapter 4 Microgrid Power Conditioning Applications

This Chapter presents different control strategies for microgrid power conditioning applications such as ancillary services to compensate a series of problems in terms of power quality, such as harmonic distortion, power factor correction, and voltage regulation, through a holistic approach. Additionally, the design of a fast-convergent state-estimator for harmonics and inter-harmonics with a decentralized structure is presented. Hardware in the loop and simulations results demonstrate the effectiveness of the proposed harmonic estimator as well as the capabilities of the power electronic converters to provide microgrid ancillary services.

Chapter 5 Conclusions

Finally, this Chapter presents the conclusions of this thesis and recommends future work.

Chapter 2

Theoretical Framework

In this Chapter, the theoretical foundations of the mathematical tools used in the following Chapters of this thesis are exposed. In a first instance, the concept of the Fourier series for the representation of periodic signals is given. Subsequently, the nonlinear systems and a class of nonlinear systems representation is introduced. Then the design of nonlinear optimal tracking and robust controllers will be presented, mainly based on nonlinear optimal control and sliding modes. Finally, the modeling of the power electronic converters used in this thesis will be presented, and implemented along with the exposed control schemes to achieve the control objectives in microgrids and power conditioning applications.

2.1 Fourier Series

Traditionally, power transmission and distribution systems are based on alternating current AC, a periodic sinusoidal signal with constant amplitude, frequency, and phase parameters. However, these parameters can be distorted due to the presence of external disturbances to the electrical power grid, which produces the superposition of harmonic components to the fundamental signal. In this sense, it is necessary to mathematically represent a periodic signal in the presence of harmonic distortion. A powerful tool for the mathematical representation of this type of signals is the so-called Fourier series [Tolstov, 1962].

Consider a signal $s(t)$ with period T approximated by its associated Fourier series as

$$s(t) = \frac{a_0}{2} + \sum_{n=1}^{N} \left[a_n \cos(2n\pi f t) + b_n \sin(2n\pi f t) \right] \tag{2.1}$$

where f is the frequency variable, $N \geq 1$ is the number of harmonics contained in the signal (with $N \to \infty$), a_0 is the average value of the function, and a_n, b_n are the coefficients of the series (named Euler coefficients [Tolstov, 1962]), which are the rectangular components of the n-th harmonic, computed as follows.

$$
\begin{aligned}
a_0 &= \frac{1}{T}\int_0^T s(t)dt \\
a_n &= \frac{2}{T}\int_0^T s(t)\cos\left(\frac{2\pi nt}{T}\right)dt \\
b_n &= \frac{2}{T}\int_0^T s(t)\sin\left(\frac{2\pi nt}{T}\right)dt.
\end{aligned}
\tag{2.2}
$$

Then, assume that signal (2.1) can be presented by

$$
s(t) = \frac{a_0}{2} + \sum_{n=1}^{N} A_n \sin(\alpha_n\, t + \theta_n) \tag{2.3}
$$

where

$$
A_n = \sqrt{a_n^2 + b_n^2} \qquad \text{and} \qquad \theta_n = \tan^{-1}\left(\frac{b_n}{a_n}\right) \tag{2.4}
$$

are A_n the amplitude of the sinusoidal function, $\alpha_n = 2\pi nf$ the angular frequency and θ_n is the phase angle[1]. This mathematical representation will be used later in this thesis to design an harmonic estimator.

2.2 Nonlinear Systems

Given a dynamic system is necessary to obtain its mathematical representation. In modeling dynamic systems, it is possible to have two different approaches: the approach of a linear system and that of a nonlinear system. Most of the problems from linear systems have found solutions since linear systems have relatively simple closed analytical solutions to many control problems as seen in [Chen, 2013]. Among them are the LQR, pole placements, and PID control. In most cases, practical applications are also based on linear controllers and handle nonlinearities by using linearized models. The nonlinear control design is challenging to face many control engineering areas, including electric power systems. Advances in future control performance will come from accommodating the nonlinear nature of the systems more directly. Therefore, this thesis proposes a nonlinear controller design to deal with the nonlinear behavior of the microgrid power electronic converters in a full range considering dynamics that linear controllers may ignore.

2.2.1. Nonlinear System Representation

When formulating a system model, important terms are the state variables which are the minimum set of variables $x_1, x_2, \ldots, x_n$ uniquely defining the system state. The

[1] *Note that the voltage and current waveforms in AC electrical systems can be described (or approximated) by* (2.1) *for a given number of* N.

state variables are written as a vector $x = [x_1, x_2, \ldots, x_n]^T$ referred as the state vector. A system may be static, when its state variables $x_1, x_2, \ldots, x_n$ are time invariant, or dynamic, when they are functions of time, that is $x_1(t), x_2(t), \ldots, x_n(t)$. This thesis is devoted to the analysis of dynamic systems modelled by a finite number of first order coupled ordinary differential equations of the form

$$\begin{aligned} \dot{x}_1 &= f_1(t, x_1, \ldots, x_n, u) \\ \dot{x}_2 &= f_2(t, x_1, \ldots, x_n, u) \\ &\vdots \quad \vdots \\ \dot{x}_n &= f_n(t, x_1, \ldots, x_n, u) \end{aligned} \tag{2.5}$$

where $\dot{x}_i$ denotes the derivative of x_i with respect to the variable t and u is a specified input variable. By using vector notation it is possible to write the n first order differential equations (2.5) as one n-dimensional first-order vector differential equation in a compact form as

$$\dot{x} = f(t, x, u). \tag{2.6}$$

Henceforth, a good part of this thesis will deal with the state equation without the explicit presence of the input u, that is, the so-called unforced state-equation [Khalil, 2002].

$$f(x) = f(t, x). \tag{2.7}$$

The unforced state equation will be used later in this thesis for the design of state estimators, as seen in Chapter 4. For simplicity of notation, henceforth, the time dependence on (2.6) and (2.7) will be omitted.

SDCF a Class of Nonlinear Systems

With the aim of finding a solution to the nonlinear optimal control problem, this thesis is focused on a class of nonlinear systems that can be described in terms of a nonlinear input-affine[2] representation and then rewritten into the so-called state-dependent coefficient factorization (SDCF). Therefore, consider a nonlinear system given as

$$\dot{x} = f(x) + B(x)u + D, \qquad \text{with} \qquad y = h(x) \tag{2.8}$$

where x, u and y are the state vector, the control input and the system output to be controlled, respectively and D is a known bounded external disturbance term. From

[2] *A nonlinear system in which the input appears linearly is called input-affine nonlinear system [Sontag, 1998]. The general form of an input affine nonlinear system is given by a vector differential equation $\dot{x} = f(x) + g(x)u$. It is important to mention that this structure is rather general in describing dynamical systems and is suitable for the design of nonlinear controllers.*

(2.8), assume that the nonlinear maps $f(x)$ and $h(x)$ are sufficiently smooth to be rewritten into the state-dependent coefficient factorization[3] [Cloutier, 1997], for which the system factorization can be obtained as $f(x) = A(x)x$ and $h(x) = C(x)x$. Based on these conditions, system (2.8) can be represented as

$$\dot{x} = A(x)x + B(x)u + D, \qquad \text{with} \qquad y = C(x)x. \tag{2.9}$$

Notice that the possible factorizations of $A(x)$ and $C(x)$ are not unique. Therefore, to obtain adequate control structures, the aforementioned factorizations must fulfill the controllability and observability properties as described in [Topputo et al., 2015]. It is essential to mention that the SDCF represents a nonlinear dynamic system in terms of a linear-like structure. Nonetheless, the SDCF is not a linearization of the system, and despite the factorization, the nonlinear nature of the system is preserved. In addition, the SDCF is required in order to solve the nonlinear optimal control problem through the associate state-dependent Riccati equation as seen in [Ornelas-Tellez et al., 2014].

2.3 Nonlinear Optimal Control

In an optimal control problem for a dynamic system described as (2.6), the control objective is to find an admissible control input $u : [t_0, t_\infty] \to \Omega \subseteq \mathbb{R}^m$ generating the corresponding state trajectory $x : [t_0, t_\infty] \to \mathbb{R}^n$ such that the cost functional J is minimized. This thesis solves the nonlinear optimal control problem through the State-Dependent-Riccati Equation (SDRE), which is the solution of the Hamilton-Jacobi-Bellman (HJB) equation. Therefore considering a nonlinear system described as (2.6), then it is possible to rewrite it into the SDCF as (2.9) to solve their associated SDRE.

2.3.1. Nonlinear Optimal Tracking Controller Design

For the optimal tracking controller synthesis, the cost functional associated with system (2.9), is defined by

$$J = \frac{1}{2}\int_{t_0}^{\infty} \left(\epsilon^T Q \epsilon + u^T R u\right) dt \tag{2.10}$$

being ϵ the tracking error defined as

$$\epsilon = r - C(x)x \tag{2.11}$$

[3] *It is worth mentioning that* (2.9) *includes the case of a linear-time invariant (LTI) system, where* $A(x)$ *and* $B(x)$ *(which are the factorized system matrices) become constant matrices; accordingly, the optimal control methodology can be directly employed in LTI systems.*

where r is the desired reference that the system output y must track, with positive definite and symmetric matrices Q and R that, respectively, weight the controller performance. Where matrix Q weights the tracking error minimization and R the control expenditure. Therefore, the objective of the nonlinear optimal tracking controller is to determine a nonlinear control law $u^*(x)$ for (2.9) such that the system output tracks the desired reference signal, and at the same time, achieve the minimization of (2.10). The optimal control solution for SDCF systems is described in the following theorem taken from [Ornelas-Tellez et al., 2014].

Theorem 1. *Assuming controllability and observability for system* (2.9)*, the nonlinear optimal control law*

$$u^*(x) = -R^{-1}B^T(x)(Px - z) \tag{2.12}$$

guarantees the trajectory tracking for system (2.9) *output toward the desired reference* r*, where matrix* P *is obtained from the solution of*

$$\dot{P} = -C^T(x)QC(x) + PB(x)R^{-1}B^T(x)P - A^T(x)P - PA(x) \tag{2.13}$$

while z *is the solutuion of*

$$\dot{z} = -\left[A(x) - B(x)R^{-1}B^T(x)P\right]^T z - C^T(x)Qr + PD \tag{2.14}$$

with the respective boundary conditions $P(\infty) = 0$ *and* $z(\infty) = 0$*. The controller* (2.12) *is said to be optimal in the sense minimizing the cost functional* (2.10)*, which has an optimal value function given by*

$$J^* = \frac{1}{2}x^T(t_0)Qr + \frac{1}{2}z^T(t_0)x(t_0) + \varphi(t_0) \tag{2.15}$$

where φ *is the solution of the scalar differential function*

$$\dot{\varphi} = -\frac{1}{2}r^TQr + \frac{1}{2}z^TB(x)R^{-1}B^T(x)z. \tag{2.16}$$

Proof. *See Appendix A.* □

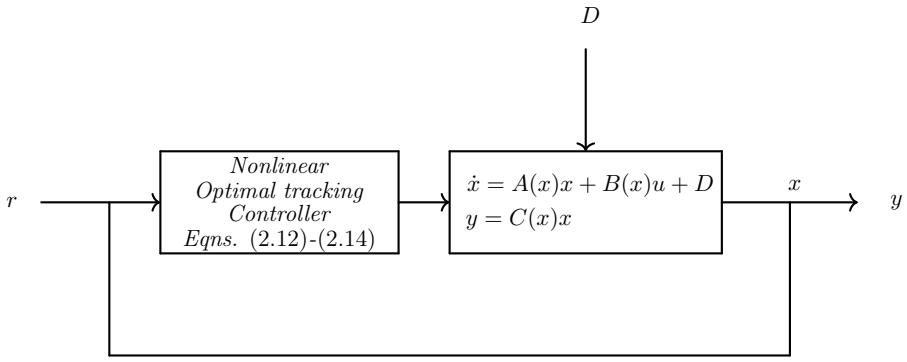

Figure 2.1: Nonlinear optimal tracking control scheme (block diagram).

The nonlinear optimal tracking controller implementation is described in terms of a control block diagram as depicted in Figure 2.1.

2.3.2. Nonlinear Optimal Control: A Robust Approach

Notice that the nonlinear optimal tracking controller (2.12)-(2.14) requires the complete knowledge of the system (2.9) in terms of its parameters related with matrices $A(x), B(x)$ and $C(x)$ which for practical applications may be uncertain or unknown in addition to the fact that the system may be subject to bounded external disturbances. Although optimal control provides robustness properties in terms of its phase margin [Astrom, 2006], if a more robust control design is required, it is possible to improve the nonlinear optimal tracking controller to reject parametric uncertainties and external disturbances by adding an integral control action to the controller. The nonlinear optimal tracking control design is defined as follows. Consider a nonlinear system described in the general form by a set of differential equations as

$$\begin{aligned} \dot{x} &= f(x) + g(x)u + D \\ y &= h(x) \end{aligned} \tag{2.17}$$

where $x \in \mathbb{R}^n$ is the state vector, $u \in \mathbb{R}^m$ is the control input vector, $y \in \mathbb{R}^p$ is the system output vector, and D is a bounded unknown disturbance term; now consider the following assumption.

Assumption 1. Functions $f(x)$ and $h(x)$ are sufficiently smooth and they can be decomposed into the so-called state-dependent coefficient factorization (SDCF)(2.9).

Therefore under Assumption 1, system (2.17) can be rewritten as

$$\begin{aligned} \dot{x} &= A(x)x + B(x)u + D \\ y &= C(x)x. \end{aligned} \tag{2.18}$$

The main objective of the nonlinear optimal robust tracking controller is to make the system output to track a desired reference signal in the presence of bounded external disturbances and, at the same time, achieve an optimization criterion mathematically described by a given performance index. In this sense, consider the tracking error (2.11), then assuming that system (2.17) may be perturbed or uncertain, an integral term is added in order to provide robustness properties to the controller defined as

$$\dot{\Phi} = -\epsilon \tag{2.19}$$

where $\Phi \in \mathbb{R}^p$ is a vector of integrators for system (2.17) with p outputs and ϵ is an error vector. Therefore, an augmented system can be stated, which includes the integral vector as

$$\begin{aligned} \dot{x}_a &= A_a(x_a) + B_a(x_a)u + D_a \\ y_a &= C_a(x_a)x_a \end{aligned} \tag{2.20}$$

where the augmented state vector and matrices are defined as

$$\dot{x}_a = \begin{bmatrix} \dot{\Phi} \\ \dot{x} \end{bmatrix} = \begin{bmatrix} -\epsilon \\ A(x)x + B(x)u + D \end{bmatrix}, \qquad A_a(x_a) = \begin{bmatrix} 0 & C(x) \\ 0 & A(x) \end{bmatrix} \tag{2.21}$$

$$B_a(x_a) = \begin{bmatrix} 0 \\ B(x) \end{bmatrix}, \qquad C_a(x_a) = \begin{bmatrix} 0 & C(x) \end{bmatrix}, \qquad D_a = \begin{bmatrix} -r \\ D \end{bmatrix}. \tag{2.22}$$

The nonlinear optimal robust controller for (2.20) is designed considering the following assumptions:

Assumption 2. The pair $[A_a(x_a), B_a(x_a)]$ is controllable and the pair $[A_a(x_a), C(x_a)]$ is observable.

Assumption 3. The state vector x_a is available for feedback[4].

Under Assumptions 1-3, the nonlinear optimal and robust control law results in

$$u^* = -R^{-1}B_a(x_a)(Px_a - z) \tag{2.23}$$

where (2.23) achieves robust trajectory tracking control for system (2.17) along the desired trajectory r as established in [Ornelas-Tellez et al., 2013]. Where P is the

[4] *Assumption 2 is related to the existence and uniqueness of the Riccati equation solution, while Assumption 3 implies that the full state vector is available for measurements, but when a state is unavailable, and observer can be implemented for estimating the full state vector.*

solution of the state-dependent Riccati differential equation and z is the solution of vector differential equation, respectively given by

$$\dot{P} = -Q_a + PB_a(x_a)R^{-1}B_a^T(x_a)P - A_a^T(x_a)P - PA_a(x_a) \tag{2.24}$$

$$\dot{z} = -\left[A_a(x_a) - B_a(x_a)R^{-1}B_a^T(x_a)P\right]^T z(x_a) + PD_a - C_a(x_a)^T Qr \tag{2.25}$$

with boundary conditions $P(\infty) = 0$ and $z(\infty) = 0$. For system (2.17), the proposed nonlinear optimal and robust control law [5] (2.23) is said to be optimal in the sense of minimizing the performance index given by

$$J = \frac{1}{2}\int_0^\infty \left(\Phi^T Q_I \Phi + \epsilon^T Q \epsilon + u^T R u\right) dt \tag{2.26}$$

where Q_I is a matrix weighting the integrators gains for Φ, Q is a positive definite matrix weighting the performance of the state vector in terms of the tracking error, and R is a positive definite matrix weighting the control effort. That is, if more importance is given to the tracking error performance, a greater value for Q must be selected, or by reducing the value of R the control expenditure will be reduced.

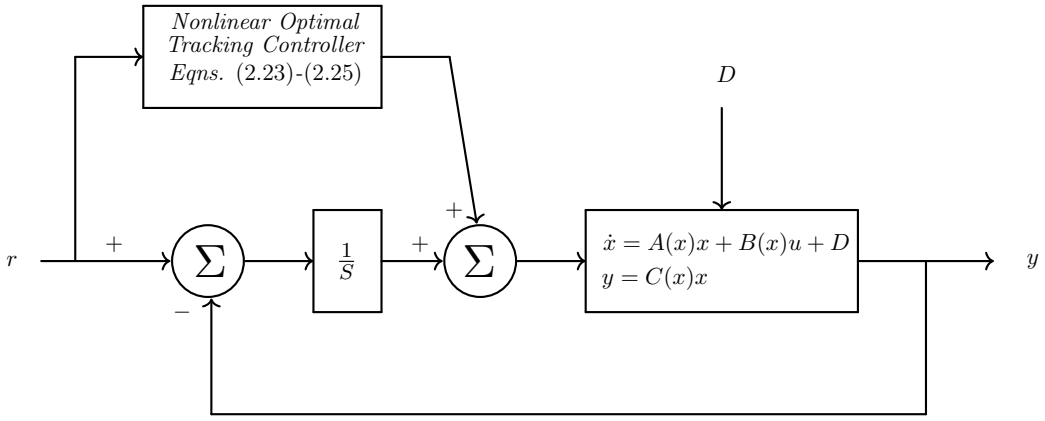

Figure 2.2: Nonlinear optimal tracking robust control scheme (block diagram).

The nonlinear optimal robust tracking controller (2.23)-(2.25) implementation is described in terms of a control block diagram as depicted in Figure 2.2.

2.4 Sliding Mode Control

In the formulation of any practical control problem, there will always be a discrepancy between the actual plant and its mathematical model. These discrepancies arise from unknown external disturbances, parametric uncertainties, and unmodeled

[5] *The proof of the stability and convergence of this controller can be seen in [Moreno and Osorio, 2008]. It is worth mentioning that by the addition of an integral term, the controller gains robustness properties. Nonetheless, the infinite gain margin of the optimal controller is lost according to the Nyquist criterion [Franklin et al., 2010]. Therefore, proper tuning of the controller gains must be performed in order to avoid oscillations or instability issues.*

dynamics. Therefore designing control algorithms capable of providing the desired performance under disturbances or uncertainties is a challenging task. Controllers which deal with these issues are called robust controllers. One particular approach to robust control design is the so-called sliding mode control. Unlike nonlinear optimal control, the sliding mode control approach is not model-based. In this sense, the control by sliding modes offers a robust control strategy in the face of uncertain dynamics and models, which can be controlled through the appropriate design of a sliding variable depending on the desired control objectives.

2.4.1. Sliding Mode Controller Design

Systems driven by sliding mode control (SMC) can be described by a set of nonlinear discontinuous differential equations. Since the classical solutions of differential equations do not hold for the case of sliding mode control, two different approaches are typically used in order to analyze systems under SMC: the Filippov's method and the equivalent control [Ferrara, 2017]. In order to illustrate the sliding mode control concept, consider a nonlinear system described as follows.

$$\dot{x} = f(t, x, u) \tag{2.27}$$

being x the state vector and u the control input. Assume that $f(\cdot)$ is sufficiently smooth and differentiable with respect to x. Then, consider a function $\sigma(x)$ to be defined as the sliding variable, which is the output variable, and assume that it is differentiable. Let define the sliding manifold or surface with the following restriction in the state space:

$$\mathcal{S} = \{x : \sigma(x) = 0\} \tag{2.28}$$

The ideal sliding mode occurs on the manifold (2.28) if the state $x(t)$ evolves in the time satisfying the condition.

$$\sigma(x(t)) = 0, \qquad \forall t > t_r \tag{2.29}$$

where t_r is a finite time. During the sliding motion, the system dynamics are restricted to move along the manifold (2.28), and thus this restricted movement implies the order reduction of the system. If the control $u = u(x)$ in (2.27) is discontinuous, then the resulting closed-loop system takes the form:

$$\dot{x} = f^c(x) \tag{2.30}$$

where $f^c : \mathbb{R}^n \to \mathbb{R}^n$ is discontinuous with respect to the state vector.

Sliding Manifold Design

Consider a first-order scalar system defined as

$$\dot{x} = f(x) + u \tag{2.31}$$

where x is the state vector, u is the control input and $f(\cdot)$ is an uniformly bounded function such that $|f(x)| \leq \Gamma^+$, where Γ^+ is a positive scalar. The sliding mode control objective is to bring to zero in a finite-time the states of the system in spite of the dynamics of $f(x)$. To reach this control objective, a discontinuous control function of the state is introduced. Then, the so-called conventional sliding mode control is defined as

$$u = -\gamma \operatorname{sign}(\sigma(x)) \tag{2.32}$$

where $\sigma(x) \in \mathbb{R} \to \mathbb{R}$ is called the sliding variable, and γ is a constant that satisfies the restriction $\gamma > \Gamma^+$. One of the major drawbacks of conventional sliding modes is the discontinuous control function (2.32), which induces the chattering effect at the system output, which is an undesirable characteristic for practical applications.

Super-twisting Algorithm

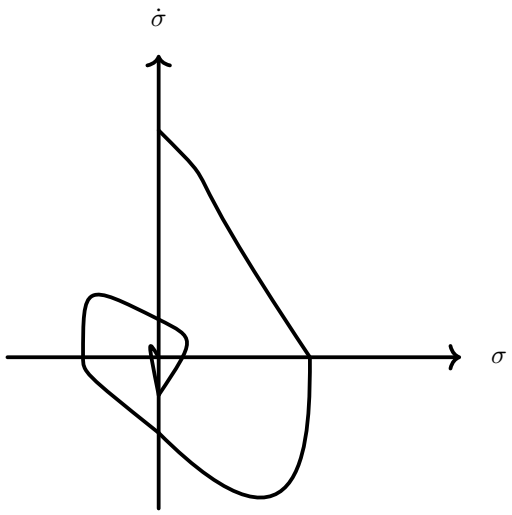

Figure 2.3: Super-twisting algorithm phase trajectory.

The discontinuous high-frequency switching sliding mode control is designed to drive the sliding variable to zero, which yields the solution to the output tracking problem $y(t) \to y_c(t)$ as the time increases, despite the presence of bounded disturbances $\varphi(y, \dot{y}, t)$. In many cases, high-frequency switching control is impractical, and continuous control is necessary. The super-twisting algorithm has been developed to control systems

with a relative degree one [Khalil, 2002] in order to avoid the chattering effect in variable structure control. Also, in this case, the trajectories on the 2-sliding plane are characterized by a twisting around the origin (see Figure 2.3). In this sense, the continuous control law $u(t)$ is constituted by two terms; the first term is defined by means of its discontinuous time derivative, while the other is a continuous function of the available sliding variable. The super-twisting controller design is given as follows. Consider the first-order nonlinear system

$$\dot{x} = f(x,t) + u \tag{2.33}$$

Where x is the state vector, u is a scalar input to be defined and $f(x,t)$ is a C^1 function with a bounded first order derivative, i.e.

$$||\dot{f}(x,t)||_\infty \leq \Gamma_1, \qquad \Gamma_1 \leq \infty \tag{2.34}$$

Where Γ_1 is an upper-bounded scalar function. If the sliding function is defined as $\sigma = x$. Then, the super-twisting controller takes the following form

$$\begin{aligned} u &= -\lambda_1 |\sigma|^{1/2} \text{sign}(\sigma) + u_1 \\ \dot{u}_1 &= -\lambda_2 \ \text{sign}(\sigma). \end{aligned} \tag{2.35}$$

Where λ_1 and λ_2 are positive constants that are chosen such that:

- $\lambda_2 > \Gamma_1$
- λ_1 is chosen such that, there exists a pair of positive matrices $\mathcal{P}$ and $\mathcal{Q}$ such that $\mathcal{P} = \mathcal{P}^T > 0$ and $\mathcal{Q} = \mathcal{Q}^T > 0$. Then the following Lyapunov equation has a solution given by

  $$\mathcal{P}M + M^T\mathcal{P} = -\mathcal{Q} \tag{2.36}$$

  where

  $$M = \begin{bmatrix} -\lambda_1 & 1 \\ -2\left(\lambda_2 - \Gamma_1\right) & 0 \end{bmatrix}. \tag{2.37}$$

Accordingly with [Moreno and Osorio, 2008], when the super-twisting controller (2.35) is applied to system (2.33) satisfying the inequality (2.34), then the sliding variable σ and its first-order derivative are enforced to converge to zero after a finite time transient. Notice that the super-twisting algorithm (2.35) does not require any information on the time derivative of the sliding variable. In addition, the following properties are exhibited by the super-twisting control formulation [Sctessel et al., 2012]:

- The super-twisting controller (2.35) is a second order sliding mode control, since it drives both $\sigma, \dot{\sigma} \to 0$ in finite time.

- The super-twisting controller (2.35) is continuous since both $\lambda_1|\sigma|^{1/2}\text{sign}(\sigma)$ and the term $\lambda_2 \int \text{sign}(\sigma)dt$ are continuous. Now, the high-frequency switching term $\text{sign}(\sigma)$ is hidden under the integral.

2.5 Nonlinear Optimal Tracking Control in Combination with Sliding Modes Controller

The objective of this research focuses on microgrid local control and power conditioning applications through power electronic converters, which present nonlinear dynamics in conjunction with their interaction with the electrical power grid. In this sense, this thesis proposes a novel control scheme based on nested control loops to control the electrical power grid variables such as voltage and power factor through the power electronic converter control, as will be described later in this thesis in Chapter 4. Thus, in this section, a nested control scheme based on the combination of nonlinear optimal control and sliding modes is presented.

2.5.1. Controller Design

The proposed nested control scheme is described as follows. Consider two coupled nonlinear dynamic systems with different time scales and different dynamic responses. The system with the fastest time response will be called the inner system, and the system with the slowest time response will be the external system. The control objective is to regulate an external system variable by tracking a given reference signal. In this sense, it is proposed to design a sliding variable defined as

$$\sigma = r_1 - x_1 \tag{2.38}$$

where r_1 is the external control reference, which for the particular case of microgrid control, could be provided by a higher hierarchy microgrid control level, and x_1 is the state variable to be controlled. The sliding variable (2.38) enters to a super-twisting sliding mode controller (2.35) whose output commands a reference control signal to the inner control loop based on nonlinear optimal tracking controller (2.12)-(2.14), which directly controls the inner system dynamics and produces an output signal that couples both systems dynamics.

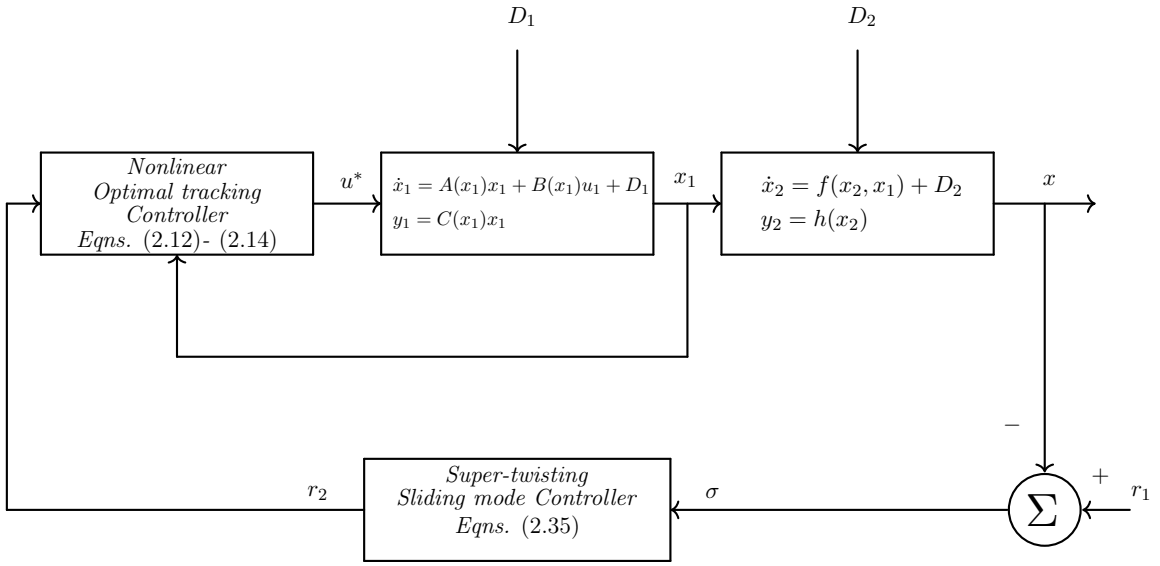

Figure 2.4: Nonlinear optimal tracking robust control scheme (block diagram).

The proposed nonlinear optimal tracking controller in combination with sliding modes is described in terms of a control block diagram as depicted in Figure 2.4. It is essential to mention that the inner control loop based on nonlinear optimal tracking control is a model-based approach that requires the complete knowledge of the system. Nonetheless, for the particular application of microgrid control and power conditioning applications, the power electronic converter dynamic model is known since it depends mainly on the filter design. Therefore, under this assumption, it is possible to directly apply the nonlinear optimal tracking controller to the power electronic converter with a reference signal commanded by an outer control loop based on super-twisting sliding modes. Then, the external control loop is based on sliding modes because it is intended to control a microgrid variable dependent on an unknown dynamic model. In this sense, sliding modes are capable of controlling uncertain systems by means of the proper design of the sliding variable.

2.6 Power Electronic Converters Modelling

The integration of distributed generation sources based on renewable energy to the electrical power grid relies on power electronic converters, which allow transforming electrical power into different formats to transport it through transmission and distribution power grids or the consumption at load centers. This section presents the modeling of the power electronics elements, which are the critical components for microgrid and power conditioning designs used to achieve the desired control objectives. Such as the inverters in their single-phase and three-phase configurations, the Boost converter, Buck converter, and the bidirectional converter. In addition, a mathematical tool that facilitates the representation and modeling of the aforementioned power electronic converters is presented.

2.6.1. The dq0 Transformation

The analysis of three-phase electrical systems introduces considerable complexity in solving machine and power system problems. An appropriate transformation of the variables obtains a much simpler form, leading to a reduced order system (in terms of its dynamic model). In this sense, the direct-quadrature-zero dq0 transformation is a tensor that rotates the reference frame of a three-phase element. This transformation can be used to rotate the reference frame of the AC waveforms. Therefore, they can be represented as DC signals to simplify the calculations and then perform an inverse transformation to recover the actual three-phase system in the abc frame. To perform the dq0 transformation, consider a three-phase time-domain quantity, for example, voltage or current in a three-phase system. Let these three quantities to be denoted as $x_a(t)$, $x_b(t)$ and $x_c(t)$. The transformation from the abc phase variables to the dq0 variables can be written in the following matrix form

$$\mathbb{T} = \frac{2}{3}\begin{bmatrix} \cos\theta & \cos\left(\theta - \frac{2\pi}{3}\right) & \cos\left(\theta + \frac{2\pi}{3}\right) \\ -\sin\theta & -\sin\left(\theta - \frac{2\pi}{3}\right) & -\sin\left(\theta + \frac{2\pi}{3}\right) \\ \frac{1}{2} & \frac{1}{2} & \frac{1}{2} \end{bmatrix} \tag{2.39}$$

and

$$x_{dq0} = \mathbb{T} x_{abc} \tag{2.40}$$

where the transformed vectors are defined as

$$x_{dq0} = \begin{bmatrix} x_d & x_q & x_0 \end{bmatrix}^T \qquad x_{abc} = \begin{bmatrix} x_a & x_b & x_c \end{bmatrix}^T \tag{2.41}$$

The angular variable θ is selected arbitrarily; it can be a function of the time where $\omega = \frac{d\theta}{dt}$. The choice of ω leads to different transformation matrices. In the case of an unspecified ω, the resulting reference frame is called an arbitrary reference frame. One may additionally choose a stationary reference frame, where $\omega = 0$, is a synchronous rotating reference frame.

Notice that the transformation $\mathbb{T}$ in (2.40) can be visualized as a projection of three stationary vectors with lengths x_a, x_b and x_c and separated by 120° onto a reference frame where the d and q axes are shown in Figure 2.5. By using the dq0 transformation the following expressions are defined

$$\begin{bmatrix} x_d \\ x_q \\ x_0 \end{bmatrix} = \frac{2}{3}\begin{bmatrix} \cos\theta & \cos\left(\theta - \frac{2\pi}{3}\right) & \cos\left(\theta + \frac{2\pi}{3}\right) \\ -\sin\theta & -\sin\left(\theta - \frac{2\pi}{3}\right) & -\sin\left(\theta + \frac{2\pi}{3}\right) \\ \frac{1}{2} & \frac{1}{2} & \frac{1}{2} \end{bmatrix} \begin{bmatrix} x_a \\ x_b \\ x_c \end{bmatrix} \tag{2.42}$$

And the inverse transformation is given by

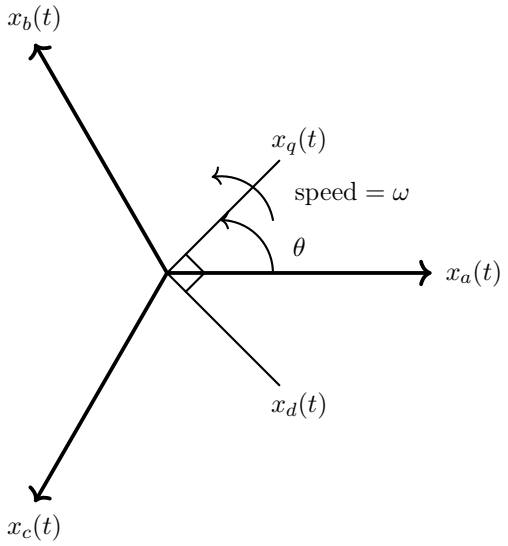

Figure 2.5: Visualization of the dq0 transformation with an arbitrary reference frame.

$$\begin{bmatrix} x_a \\ x_b \\ x_c \end{bmatrix} = \begin{bmatrix} \cos\theta & -\sin\theta & 1 \\ \cos\left(\theta - \frac{2\pi}{3}\right) & -\sin\left(\theta - \frac{2\pi}{3}\right) & 1 \\ \cos\left(\theta + \frac{2\pi}{3}\right) & -\sin\left(\theta + \frac{2\pi}{3}\right) & 1 \end{bmatrix} \begin{bmatrix} x_d \\ x_q \\ x_0 \end{bmatrix} \tag{2.43}$$

The dq0 transformation will be used in the subsequent section of this Chapter to model the grid-connected three-phase converter more straightforwardly. It is essential to mention that the fundamental reason to transform the three phase instantaneous voltages and currents into the dq0 reference frame is to reduce the number of dynamic equations of the system to simplify computations. In addition, linear control approaches use the dq0 transformation to convert the time-varying magnitudes of an electrical system into constant variables in a rotatory reference frame, and by doing so, linear controllers like PID control which are not capable of tracking efficiently time-varying reference signals now in the new reference frame can track the signals. However, one of the main limitations of the dq0 transformation is the assumption of the existence of a balanced three-phase system.

2.6.2. Inverter Filter Selection

An L filter or LCL filter is usually placed between the inverter and the grid to attenuate the switching frequency and the harmonics produced by the grid-connected inverter. There are several types of filters, the simplest variant is the L inductive filter connected to the inverter's output. Nonetheless, combinations like LC and LCL filters are also used. Each of these configurations has advantages and disadvantages relative to one another. Below three filter configurations and their main features are presented.

L Filter

The L filter is a first-order filter with an attenuation of $20dB$/decade over the whole frequency range. The L filter application is suitable for converters with high switching frequency. In addition, the L filter significantly decreases the dynamics of the system filter in comparison with LCL filters. The L filter topology for grid-connected inverters is depicted in Figure 2.6.

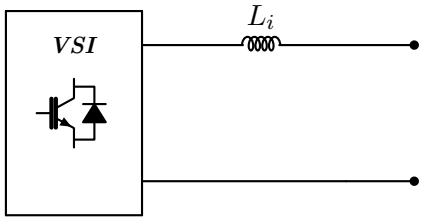

Figure 2.6: L filter topology for grid connected inveters.

LC Filter

The LC filter is a second-order filter, which has a better damping behavior in comparison with the L filter. The second-order filter provides $40dB$/decade of attenuation after the cut-off frequency. Nonetheless, it presents a peaking at the resonant frequency. On the one hand, the high capacity of this filter has a positive effect on power quality (in terms of the harmonic reduction [Mahamad et al., 2004]). On the other hand, a high inductance value is required to achieve demanded cut-off frequency of the filter. In addition, the resonant frequency of the LC filter is dependent on the grid impedance, which is a not desired characteristic for practical implementations of power electronic converters. The LC filter topology is described in Figure 2.7.

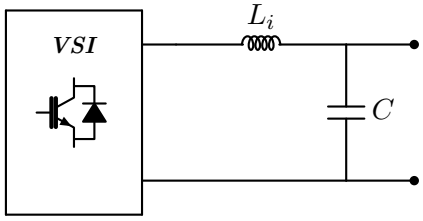

Figure 2.7: LC filter topology for grid connected inveters.

LCL Filter

An LCL filter is often used to interconnect an inverter to the main utility grid in order to filter the harmonics produced by the inverter. The attenuation of the LCL filter is $60dB$/decade for frequencies above the resonant frequency. Therefore, a lower switching frequency for the converter can be used. The LCL filter also provides a better coupling between the filter and the grid impedance and a lower current ripple across

the inductor. Nonetheless, the LCL filter increases the system order in comparison with a simple L filter. However, the LCL filter has been widely reported to be an effective filter for grid-connected inverters. Proper selection of the values of the inductor and capacitor for an LCL filter is an important criterion in order to improve the power quality. The LCL filter topology for a grid-connected inverter is described in Figure 2.8.

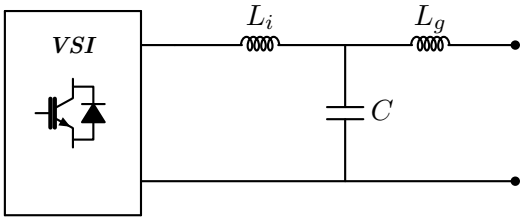

Figure 2.8: LCL filter topology for grid connected inveters.

To design LCL filters, several characteristics of the filter have to be considered, such as the current ripple, switching ripple attenuation, size of the filter, etc. The parameters required to design the filter circuit are the DC link voltage V_{dc}, fundamental voltage output of the inverter V_i, V_p the per-phase voltage, the rated active power P_n, switching frequency f_s, and the fundamental grid frequency f_g. The LCL filter design is based on the following steps:

1. Compute the base impedance Z_b, base inductance L_b, base capacitance C_b and rated peak-to-peak current I_{max} as

$$Z_b = \frac{V_p^2}{P_n}, \qquad L_b = \frac{Z_b}{2\pi f_g}, \qquad C_b = \frac{1}{2\pi f_g Z_b} \tag{2.44}$$

2. Choose the desired ripple attenuation ΔI_{max} and calculate the minimum value of the inverter-side inductor as

$$L_s = \frac{V_{dc}}{6 f_s \Delta I_{max}}, \tag{2.45}$$

where

$$\Delta I_{max} = 0.1 I_{max}, \qquad \text{with} \qquad I_{max} = \frac{P_n \sqrt{2}}{3 V_p} \tag{2.46}$$

3. Select the value of the capacitor. The filter capacitor is designed considering the maximum power factor variation at the grid side of 5%, resulting the filter

capacitance $C_f = 0.05C_b$. This is

$$C_f \leq k_c C_b \tag{2.47}$$

where k_c is chose generally as 5% or lower.

4. Select the desired current ripple reduction by choosing the adequate grid-side inductor L_g parameter in terms of the inverter-side inductor L_i as

$$L_g = \frac{\sqrt{\frac{1}{k_a^2}} + 1}{\omega_{sw}^2 C_f} \tag{2.48}$$

where k_a is the per-unit desired attenuation rate, and ω_{sw} is the switching frequency angular speed. In most cases the grid-side inductor is designed considering a 20% of the inductor value connected at the inverter side. This will provide a better attenuation at the frequency above the 50th harmonic and can be calculated as in [Mallick, 2020], thus the grid side inductor is computed as follows

$$L_g = 0.2L_i \tag{2.49}$$

5. Compute the resonance frequency f_r, and verify if it is within the established limits to avoid resonance issues (which can be harmful to the electrical network), where f_r is computed as follows

$$f_r = \sqrt{\frac{L_s + L_g}{L_s L_g C}}, \qquad \text{and} \qquad 10f_g \leq f_r \leq \frac{1}{2}f_s \tag{2.50}$$

It is important to mention that there are different approaches to calculate the parameters of an LCL filter, for which optimization techniques can even be used depending on the filter response, as shown in [Rodriguez-Lopez et al., 2019].

2.6.3. Pulse Width Modulation

In order to convert the control signals into drive pulses of the power electronics devices, that control the amplitude and frequency of the output voltage of a VSI, a modulation strategy such as pulse width modulation (PWM) [Holmes, 2003] is necessary. In this sense, for PWM inverters, the following control is possible:

- Linear control of the fundamental output voltage.
- Control of frequency of the fundamental output voltage.

- Control of the harmonics included in the output voltage.

To improve the performance of power electronics control, a variety of PWM techniques have been proposed ever since the sinusoidal pulse width modulation (SPWM) was first introduced in 1964 [Kim, 2017]. For this research, the considered PWM technique, generates pulses for a carried-based PWM converters using a two level topology based on conmmutated devices (FET's, GTO's or IGBT's) of single or three-phase bridges. The pulses are generated by comparing a triangular carrier waveform to a reference modulated signal, based on the following rule:

- Voltage reference v_{ref} > triangular carrier : upper switch is turn on.
- Voltage reference v_{ref} < triangular carrier : lower switch is turn on.

The amplitude, phase, and frequency of the reference signal are used to set the output voltage of the inverter bridge triggered by the PWM signals. The two pulses firing the two switching devices of a given arm bridge are complementary. Figure 2.9 shows the two pulses generated by the PWM when it's programmed to control a one-arm bridge.

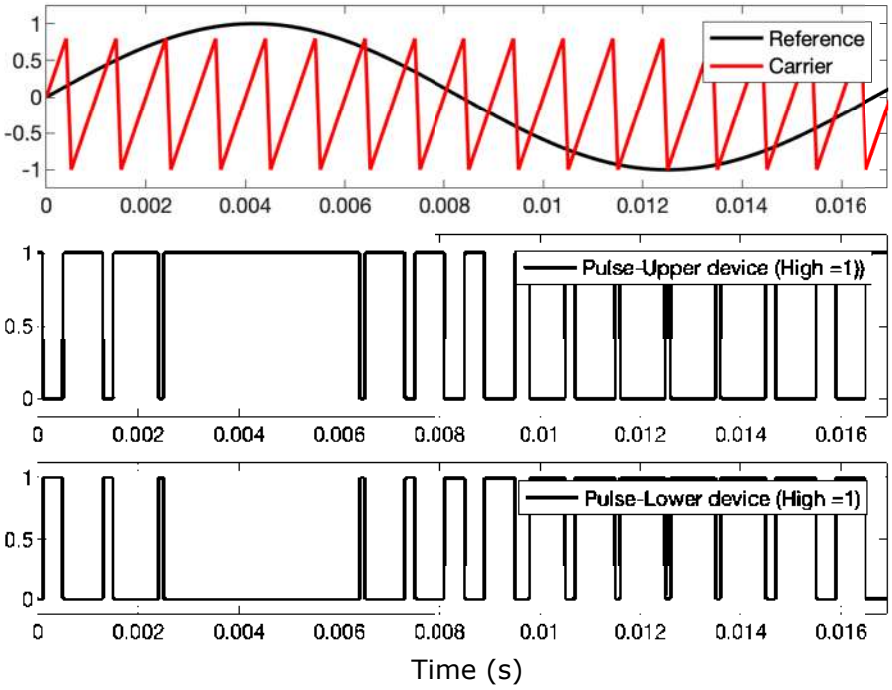

Figure 2.9: Pulse width modulation in converter bridge.

The devices for power electronic converters applications are selected according to the required power capacity and switching frequency. The GTO thyristor and IGCT have a high-power handling capability, but their switching frequency is very low, being below 1 kHz. The IGBT is now most widely used for medium- to high-power applications. Some of the IGBTs have switching frequencies up to 100 kHz, but most are normally below 20 kHz. The MOSFET, which can support a high switching frequency beyond 100

kHz, is the most suitable device for small-power applications. For inverter applications, commonly a higher switching frequency leads to fewer harmonics [Kim, 2017], fixed frequency PWM-based power electronic converters have tipical values of 20 kHz to 100 kHz. In this research it is considered the use of IGBT power electronic based devices.

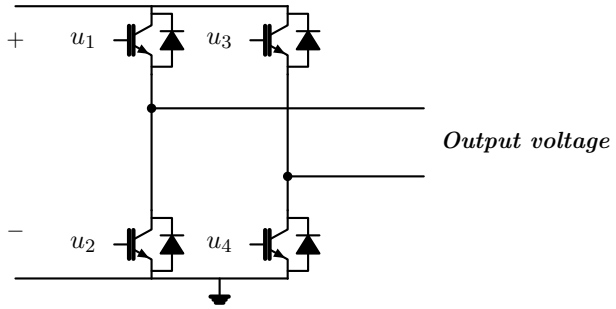

Figure 2.10: Two arm bridge (4 pulses) configuration.

Figure 2.10 shows the self-commutated devices of a two arm bridge. The four pulses are generated by a PWM technique where pulses 1 and 3 fire the upper devices of the first and second arm while pulses 2 and 4 fire the lower devices.

2.6.4. Single-Phase Inverter

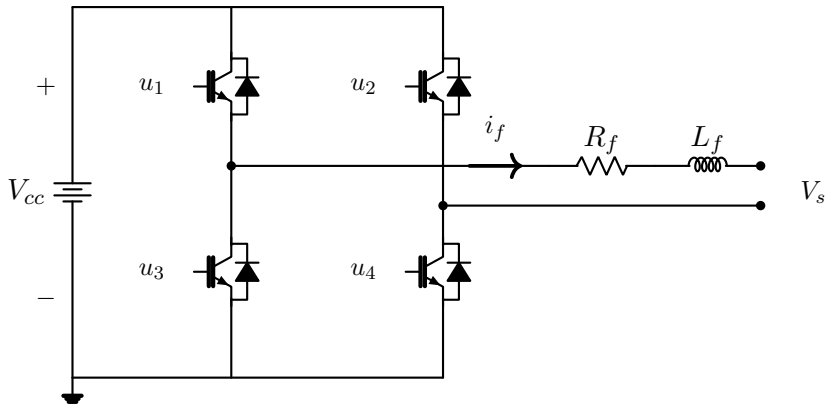

Figure 2.11: Single phase inverter with L filter.

One of the critical elements used in the subsequent Chapters of this thesis is the single-phase inverter. This element can convert the DC power, which may be derived from a renewable energy resource (i.e., battery, solar panel), into AC waveform. The inverter is built of switching devices activated through a proper modulation technique (i.e., pulse width modulation PWM); thus, the way in which the switching takes place in the inverter produces the required output. A two-level inverter is considered in combination with the proper filter, which will be later used in order to fulfill the microgrid local control objectives and power conditioning applications such as ancillary

services. For this thesis and the further application of this converter as an active power filter, a simple L filter is considered to simplify the system dynamics.

Single Phase Inverter Dynamic Model

Consider the circuit configuration as described in Figure 2.11. Then, the single-phase inverter with L filter dynamic model is expressed by

$$L_f \frac{di_f}{dt} = -R_f i_f + V_{cc} u - V_s \tag{2.51}$$

where i_f is the output inverter current, V_{cc} is the source DC voltage, V_s is the AC node voltage, L_f and R_f are the inverter output filter inductance and resistance, respectively, and $u \in [0, 1]$ is the control input used to modulate the PWM duty cycle in the inverter. It is important to notice that the dynamic model (2.51) is suitable for the nonlinear optimal tracking controller (2.12)-(2.14) described in the previous section, and it will be later used for power conditioning applications within this thesis. In addition, it is possible to implement different configurations of power electronic converters, such as multilevel converters [Can and Sayan, 2018]. In this work, a two-level power electronic converter is used with an inductive output filter as a shunt current source, which in combination with the proposed nonlinear optimal controller, can provide a wide range of ancillary services to a power system node, such as harmonics and reactive power compensation while taking advantage of the existing infrastructure of typical industrial applications such as distributed generation systems.

2.6.5. The Grid-Tied Three-Phase Inverter

A three-phase inverter circuit (see Figure 2.12) converts the DC power supply into three-phase AC power output, where the three arms are normally shifted by an angle of 120° to generate a three-phase signal. In this thesis, it is considered the LCL filter connected at the three-phase inverter output to reduce the harmonic distortion and effectively couple the DC power source and the electrical power grid.

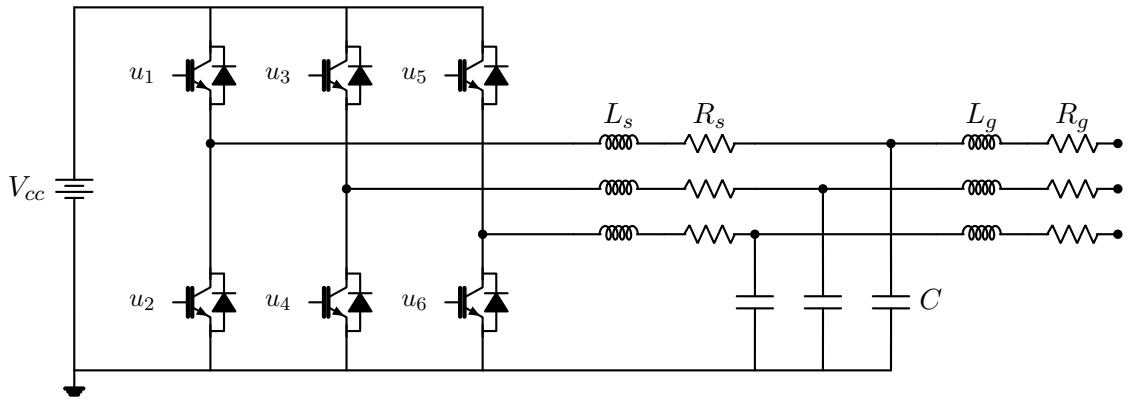

Figure 2.12: Three-phase grid-connected inverter.

Three-Phase Inverter Dynamic Model

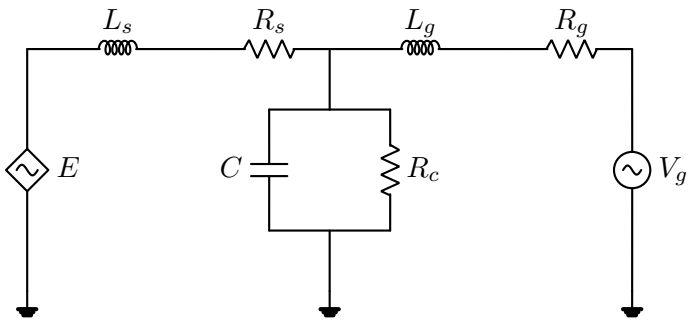

Figure 2.13: Single-phase equivalent circuit of a grid-tied power electronics converter with an LCL filter.

For simplicity of calculations, consider the single-phase equivalent circuit for the grid-connected three-phase inverter with a LCL filter as seen in Figure 2.13, where the dynamic equations of the circuit per phase are modeled on the abc reference frame by applying the Kirchhoff laws are given by

$$\begin{aligned}
\frac{di_s}{dt} &= \frac{1}{L_s}E - \frac{R_s}{L_s}i_s - \frac{1}{L_s}V_c \\
\frac{di_g}{dt} &= -\frac{R_g}{L_g}i_g + \frac{1}{L_g}V_c - \frac{1}{L_g}V_g \\
\frac{dV_c}{dt} &= \frac{1}{C}i_s - \frac{1}{R_cC}V_c - \frac{1}{C}i_g
\end{aligned} \tag{2.52}$$

where L_s, R_s are inductance and resistance on the inverter-side respectively, C is the filter capacitor in parallel with the internal capacitor resistance R_c, L_g and R_g are the inductance and equivalent resistance on the grid-side respectively, E represents the output voltage of the three-phase inverter, V_g is the AC voltage of the utility grid, i_s is the current flowing through the LC branch on the inverter side, i_g is the current flowing through the utility-grid branch and V_c is the voltage on the filter capacitor. In order to simplify the number of dynamic equations of the system and for the later control purposes, the dynamic equations (2.52) are transformed into the dq0 reference frame through the Park's transformation (2.40), resulting in the following system of equations.

$$\begin{aligned}
\frac{di_{sd}}{dt} &= -\frac{R_s}{L_s}i_{sd} + \frac{1}{L_s}E_d - \frac{1}{L_s}V_{cd} + \omega i_{sq} \\
\frac{di_{sq}}{dt} &= -\frac{R_s}{L_s}i_{sq} + \frac{1}{L_s}E_q - \frac{1}{L_s}V_{cq} - \omega i_{sq} \\
\frac{di_{gd}}{dt} &= -\frac{R_g}{L_g}i_{gd} + \frac{1}{L_g}V_{cd} - \frac{1}{L_g}V_{gd} + \omega_{i_{gq}} \\
\frac{di_{gq}}{dt} &= -\frac{R_g}{L_g}i_{gq} + \frac{1}{L_g}V_{cq} - \frac{1}{L_g}V_{gq} - \omega i_{gd} \\
\frac{dV_{cd}}{dt} &= -\frac{1}{R_c C}V_{cd} + \frac{1}{C}i_{sd} - \frac{1}{C}i_{gd} + \omega V_{cq} \\
\frac{cV_{cq}}{dt} &= -\frac{1}{R_c C}V_{cq} + \frac{1}{C}i_{sq} - \frac{1}{C}i_{gq} - \omega V_{cd}.
\end{aligned} \tag{2.53}$$

For control purposes, the utility grid voltage can be mathematically modeled as a known disturbance term, generated by an exosystem represented as

$$\frac{dV_{gd}}{dt} = 0 \qquad \frac{dV_{gq}}{dt} = 0 \tag{2.54}$$

with initial conditions $V_{gd}(0) = V_p$ and $V_{gq}(0) = 0$, where V_p is the amplitude of the sinusoidal waveform V_g. The three-phase inverter will be used in the subsequent Chapters of this thesis, along with a nonlinear robust controller in order to provide an effective solution for the power-sharing between the microgrid distributed generation units and the main utility grid.

2.6.6. The Boost Converter

Previous to a DC to AC conversion process, the electrical power derived from a constant DC power source or a renewable energy resource such as a solar panel or battery needs to be stepped up. In this sense, the Boost converter or step-up converter [Mohan, 2003] is a DC-DC power electronic device that steps up a DC voltage input to its output while stepping down the current.

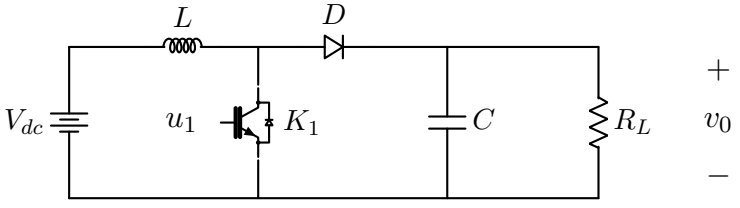

Figure 2.14: Boost-converter.

Boost Converter Dynamic Model

According to Figure 2.14, the dynamics of the Boost converter can be described as follows [Khalil, 2015]. When the switch K_1 is in the $u_1 = 1$ position, the dynamic model of the system is

$$L\frac{di_L}{dt} = V_{dc}, \qquad C\frac{dv_o}{dt} = -\frac{v_o}{R_L} \tag{2.55}$$

while the switch is in the position $u_1 = 0$, the model yields to

$$L\frac{di_L}{dt} = -v_o + V_{dc}, \qquad C\frac{dv_o}{dt} = -i_L - \frac{v_o}{R_L}. \tag{2.56}$$

Then, equation (2.55) and (2.56) can be written as

$$\begin{aligned} L\frac{di_L}{dt} &= -(1-u_1)v_o + V_{dc} \\ C\frac{dv_o}{dt} &= (1-u_1)i_L - \frac{v_o}{R_L} \end{aligned} \tag{2.57}$$

where u_1 is a discrete variable that takes the values 0 or 1, R_L is the load resistance, i_L is the current flowing through the coil L with an internal resistance r and v_o is the output voltage measure at C. Notice that the Boost converter experiences a non-minimum phase behavior [6] with respect to a voltage output, then in order to deal with the non-minimum phase behavior of the system, a current output is selected as the control variable, where the desired current reference is given by

$$i_{ref} = \frac{V_{ref}^2}{V_{dc}R_L} \tag{2.58}$$

where V_{ref} is the reference voltage for the DC bus, V_{dc} is the DC voltage in the power supply side, and R_L is the load resistance connected to the DC bus.

2.6.7. The Bidirectional Buck-Boost Converter

The bidirectional converter is one of the main components for connecting energy storage systems in microgrids since it allows the power exchange between the energy storage unit and the DC bus in a microgrid.

[6] *The minimum phase property is described for linear systems when all the zeros of the transfer functions have negative real parts. Non-minimum phase system: It is a system in which some of the poles and zeros may lie on the right side of the s-plane [Khalil, 2002].*

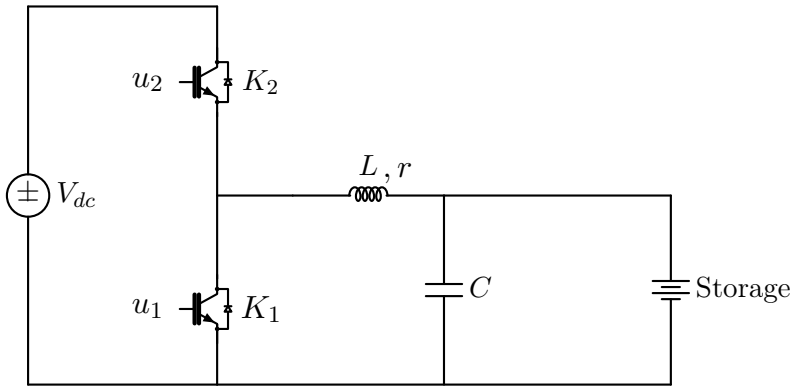

Figure 2.15: Proposed bidirectional Buck-Boost converter.

One of the most common power electronic configurations is the bidirectional DC/DC power electronic converter, as seen in Figure 2.15, which is formed by a Buck and a Boost circuit in an anti-parallel configuration as seen in [Pinto et al., 2013],[Xiao-li and Da-qiang, 2012]. This converter is among the most widely used type of bidirectional converters and is recognized to be the basic structure of the bidirectional power converters. The operation of the proposed configuration is divided in two modes; charging mode and discharging mode. For this thesis, from now on, it will be considered an energy storage device based on supercapacitors, where the supercapacitor array can be modeled by its equivalent electrical circuit as seen in [Zhang et al., 2018b].

Supercapacitor Dynamic Model

Consider the bidirectional power electronic converter as seen in Figure 2.15.

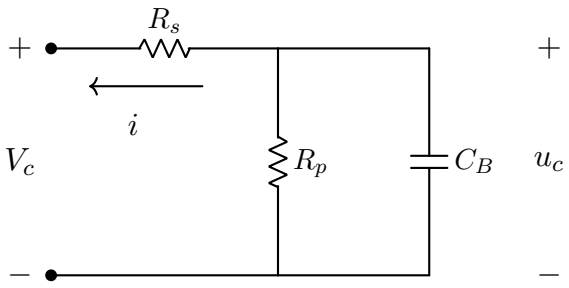

Figure 2.16: Supercapacitor equivalent model.

Equivalent circuit models for supercapacitors, employ parameterized RC networks to mimic the electrical behavior of the supercapacitor and the ease of implementation in terms of ordinary differential equations. The most common supercapacitor model is depicted in Figure 2.16, which is the simplest supercapacitor model with an equivalent circuit represented by a resistor connected in series with a capacitor with another added parallel resistor which emulates the self-discharge supercapacitor phenomenon. The dynamic model of the classical supercapacitor model is described as follows.

$$\begin{aligned} \frac{du_c}{dt} &= -\frac{1}{C_B R_p} u_c + \frac{1}{C_B} i \\ V_c &= u_c + i R_s \end{aligned} \tag{2.59}$$

where V_c denotes the output voltage of the supercapacitor model, R_s is the internal resistance including the electrolyte resistance and contact resistance, R_p is used in order to simulate the self-discharge phenomenon, u_c is the voltage across the capacitor and i is the charging current. More complex models to represent the dynamics of supercapacitors can be obtained from the literature as seen in [Zhang et al., 2018a, Zhang et al., 2018b]. However, this will depend on the physical phenomena to analyze, such as the state of charge (SOC) of the capacitor or its thermal characteristics, more details about supercapacitor modeling can be consulted in [Zhang et al., 2018b].

Bidirectional Converter Charging Mode

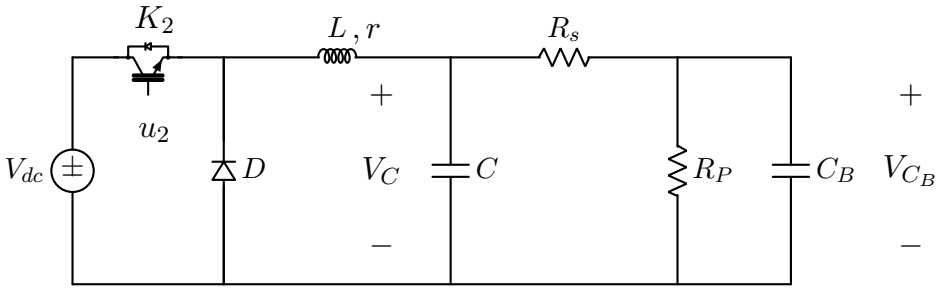

Figure 2.17: Bidirectional converter charging mode.

During the charging mode of the bidirectional DC/DC power converter the switch K_2 is controlled by a PWM signal ($u_2 \in \{0, 1\}$) while the switch K_1 is open $u_1 = 0$. Therefore, the bidirectional converter is operated as a Buck converter, and the power flows from the DC bus to the energy storage device. Then, the dynamic model of the converter becomes as follows.

$$\begin{aligned} L\frac{di_L}{dt} &= -r i_L - V_C + V_{dc} u_2 \\ C\frac{dV_C}{dt} &= i_L - \frac{1}{R_s} V_C + \frac{1}{R_s} V_{C_B} \\ C_B\frac{dV_{C_B}}{dt} &= \frac{1}{R_s} V_C - \left(\frac{1}{R_s} + \frac{1}{R_p}\right) V_{C_B} \end{aligned} \tag{2.60}$$

During the charging mode, the control objective is to regulate the current flowing through the coil considering the configuration as described in Figure 2.17.

Bidirectional Converter Discharging Mode

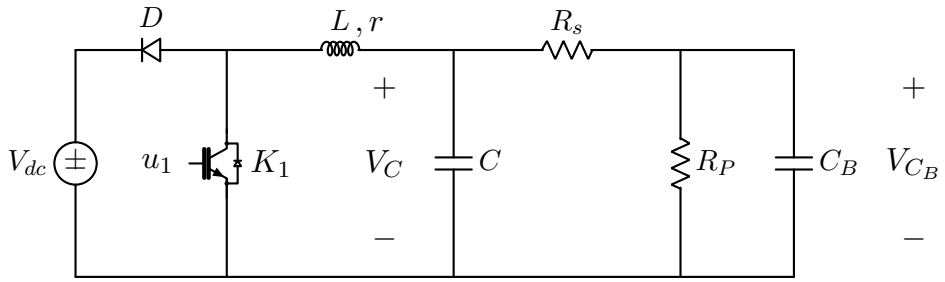

Figure 2.18: Bidirectional converter discharging mode.

While discharging, the bidirectional DC/DC power converter operates as a Boost converter. During this configuration, only the switch K_1 is controlled by a PWM signal ($u_1 \in \{0, 1\}$) while the switch K_2 is open ($u_2 = 0$). Therefore the power flows from the energy storage device to the DC bus considering the following dynamic model as depicted in Figure 2.18. Therefore, the dynamic model of the bidirectional converter becomes

$$\begin{aligned} L\frac{di_L}{dt} &= -ri_L - V_C + (1-u_1)V_{dc} \\ C\frac{dV_C}{dt} &= i_L - \frac{1}{R_s}V_C + \frac{1}{R_s}V_{C_B} \\ C_B\frac{dV_{C_B}}{dt} &= \frac{1}{R_s}V_C - \left(\frac{1}{R_s} + \frac{1}{R_p}\right)V_{C_B}. \end{aligned} \tag{2.61}$$

Bidirectional Control Structure

Intending to have a complete system in terms of charging and discharging operative modes of the bidirectional DC/DC power converter, it is possible to consider the following dynamic model.

$$\begin{aligned} L\frac{di_L}{dt} &= -ri_L - V_C + \Theta V_{dc} \\ C\frac{dV_C}{dt} &= i_L - \frac{1}{R_B}V_C + \frac{1}{R_b}V_{C_B} \\ C_B\frac{dV_{C_B}}{dt} &= \frac{1}{R_B}V_C - \left(\frac{1}{R_B} + \frac{1}{R_p}\right)V_{C_B} \end{aligned} \tag{2.62}$$

where Θ is the control input given by

$$\Theta = (\zeta u_1 + (1-\zeta)(1-u_2)) \tag{2.63}$$

The parameter ζ is defined in order to switch between the two operative mode of the bidirectional converter where

- $\zeta = 1 \rightarrow$ Buck operative mode.
- $\zeta = 0 \rightarrow$ Boost operative mode.

It is essential to mention that the function ζ can be generated by a higher control level entity (intelligent controller) which, based on the measured information, decides whether to change the bidirectional converter structure and then apply the proper local controller. The bidirectional power electronic converter along with a proposed intelligent controller, will be used in the next Chapter of this thesis to include an energy storage device to the proposed microgrid distributed generation nodes and provide ancillary services.

2.7 Summary

In this Chapter, the mathematical tools necessary for representing nonlinear systems and signals are exposed. The nonlinear optimal control theory, sliding modes controllers, and the modeling of electronic power converters are presented, which will be used in the subsequent Chapters of this thesis to achieve the proposed objectives such as the primary local control of microgrids and power conditioning applications to provide ancillary services.

Chapter 3

Control of Distributed Energy Resources in Microgrids

In this Chapter, the use of primary or local control strategies applied to power electronic interfaced converters in microgrids is presented. The primary local control objective is to regulate voltage and frequency (VF control) during the microgrid isolation mode and the active and reactive power sharing (PQ control) to the host electrical power grid during the microgrid interconnected mode. These objectives are achieved through nonlinear and robust control strategies based on nonlinear optimal tracking control and super-twisting sliding modes. In addition, the nonlinear optimal control of an energy storage system based on supercapacitors is presented.

3.1 Microgrid Local Controllers

Distributed generation units produce either a DC or AC power to the electrical power grid or local loads through a power electronic interface (PEI). In this sense, the direct integration of distributed generation units requires the development of robust and reliable control strategies applied to power electronic converters during the different microgrid operative modes. This is done through a hierarchical control structure. In this Chapter, emphasis will be placed on the design of primary controllers or local controllers for power electronic interfaced converter for microgrids.

Definition 3.1.1 (Local Controller)**.** The microgrid local control includes total hardware control of the distributed generator's internal voltage/current control loops, which stabilizes the DGs by measuring and controlling the local signals. In addition, local controllers provide efficient voltage and frequency control in case of islanded operation, ancillary services during the interconnected mode, and deal efficiently with frequency and voltage variations during transitions from interconnected to islanded operation and vice versa [Hatziargyriou, 2014].

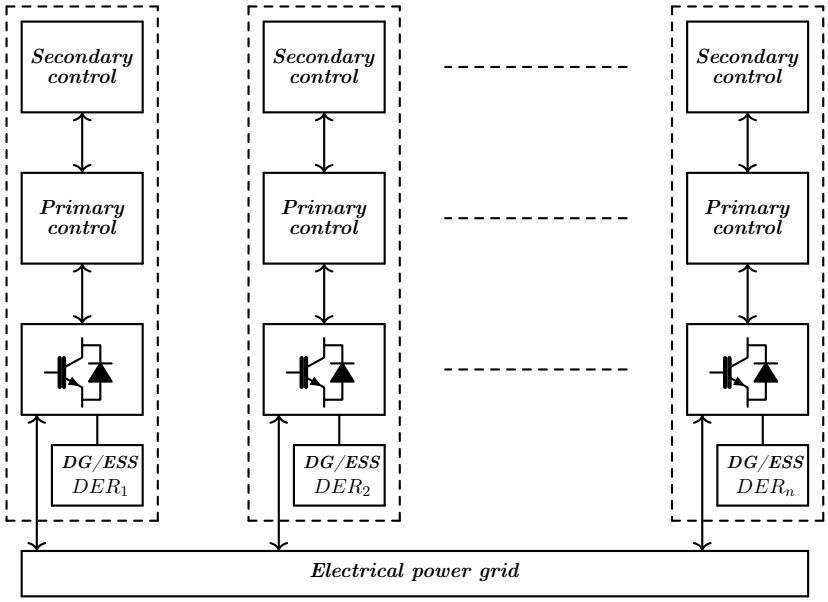

Figure 3.1: Schematic diagram of a decentralized microgrid control structure with local controllers.

According to Definition 3.1.1, the microgrid local controllers are the inner control loops within a microgrid hierarchy that directly acts over the power electronic converter output with a specific control objective. The implementation of primary or local controllers in a microgrid is exemplified in Figure 3.1, where a set of distributed generation nodes operate in a parallel configuration within a microgrid, each with local controllers, achieving various control objectives. In addition, if it is necessary, a higher hierarchical control level can coordinate the operation of the distributed generation nodes through communication links. A design approach for local controllers in microgrid based on nonlinear optimal control will be shown below.

3.1.1. Primary Control, Inverter Output Control

Consider a microgrid configuration as depicted in Figure 3.2, which consists of a distributed generator unit (i.e., fuel cell, photovoltaic array, battery, etc.) generating power at a DC level, connected with a three-phase inductive-resistive load through a power electronic converter, along with an LCL output filter. It is considered that the microgrid can be operated at either one of the different operative modes, isolated mode or grid-connected mode by the opening or closing of the breakers, which connect the microgrid to the main utility grid or host grid with voltage V_g through a distribution line with the elements L_g and R_g per phase.

The Isolated Microgrid Model

The dynamic model for the isolated microgrid as depicted in Figure 3.2, when the breakers are opened considering a single phase, is computed by applying the Kirchhoff

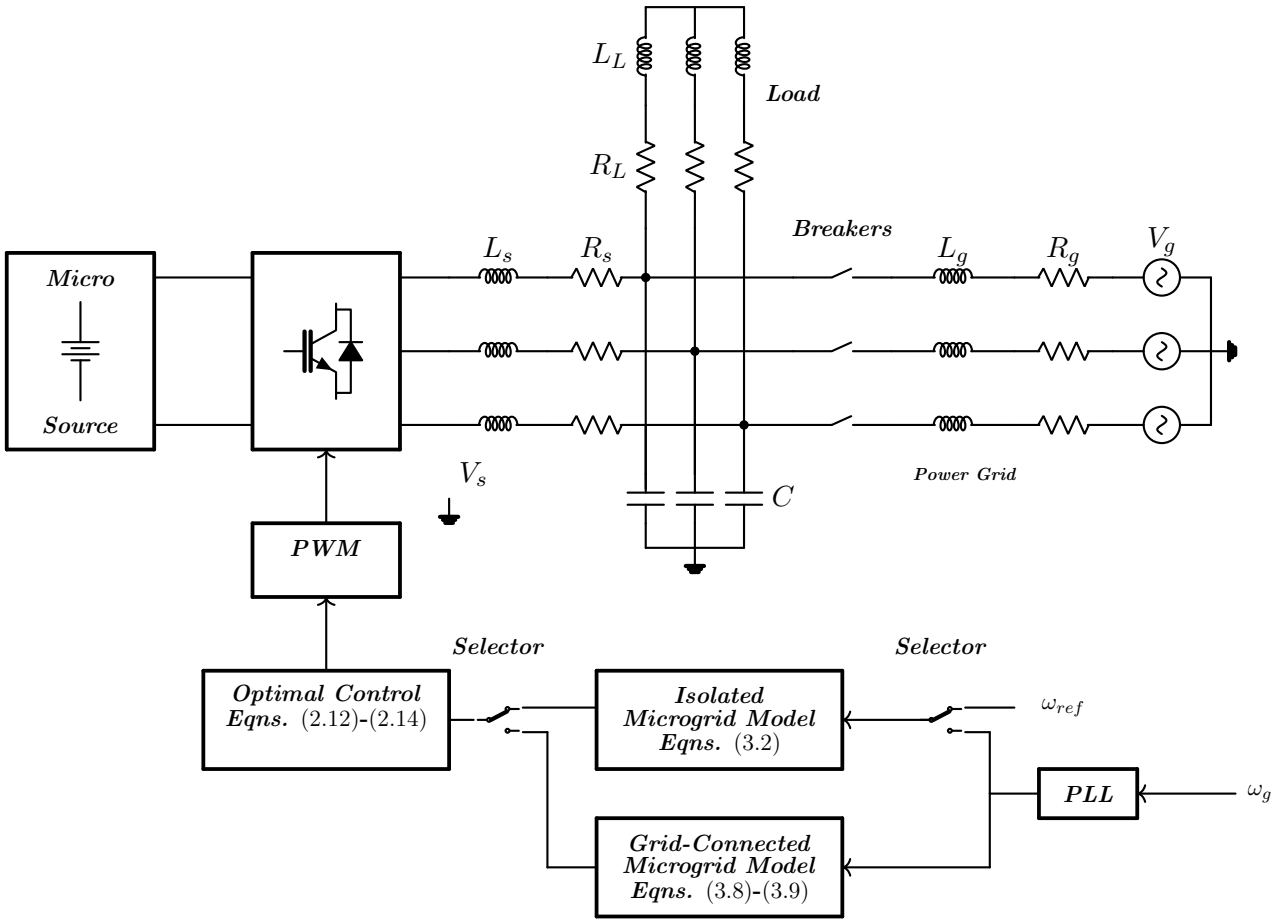

Figure 3.2: Proposed microgrid control system configuration.

law as follows:

$$\begin{aligned} L_s \frac{di_{L_s}}{dt} &= V_s - i_{L_s} R_s - V_c \\ C \frac{dV_c}{dt} &= i_{L_s} - i_{L_L} \\ L_L \frac{di_{L_L}}{dt} &= V_c - R_L i_{L_L} \end{aligned} \tag{3.1}$$

where V_s is the inverter output voltage, L_s and R_s are the inverter side inductor and resistance, respectively, i_{L_s} is the output current of the inverter, L_L and R_L are the load inductance and resistance, respectively[1], i_{L_L} is the load current and V_c is the voltage at the filter capacitor. In order to have a three-phase system representation, system (3.1) is transformed into the dq0 frame with the following representation

[1] *For this explanation, an RL load is considered, since its the most typical case for industrial and residential consumers.*

$$
\begin{aligned}
\frac{di_{L_{sd}}}{dt} &= \frac{1}{L_s}V_{s_d} - \frac{R_s}{L_s}i_{L_{sd}} - \frac{1}{L_s}V_{c_d} + \omega i_{L_{sq}} \\
\frac{di_{L_{sq}}}{dt} &= \frac{1}{L_s}V_{s_q} - \frac{R_s}{L_s}i_{L_{sq}} - \frac{1}{L_s}V_{c_q} - \omega i_d \\
\frac{dV_{c_d}}{dt} &= \frac{1}{C}i_{L_{sd}} - \frac{1}{C}i_{L_{L_d}} + \omega V_{c_q} \\
\frac{dV_{c_q}}{dt} &= \frac{1}{C}i_{L_{sq}} - \frac{1}{C}i_{L_{L_q}} - \omega V_{c_d} \\
\frac{di_{L_d}}{dt} &= \frac{1}{L_L}V_{c_d} - \frac{R_L}{L_L}i_{L_{L_d}} + \omega i_{L_{L_q}} \\
\frac{di_{L_q}}{dt} &= \frac{1}{L_L}V_{c_q} - \frac{R_L}{L_L}i_{L_{L_q}} - \omega i_{L_{L_d}}
\end{aligned}
\tag{3.2}
$$

where ω is the rotating reference frequency for the Park's transformation (2.40). Then system (3.2), can be rewritten into the state-space representation as (2.9), by choosing a state vector defined as

$$
x = \begin{bmatrix} i_{L_{sd}} & i_{L_{sq}} & V_{c_d} & V_{c_q} & i_{L_{Ld}} & i_{L_{Lq}} \end{bmatrix}^T \tag{3.3}
$$

with the matrices

$$
A(x) = \begin{bmatrix}
-\frac{R}{L} & \omega & -\frac{1}{L} & 0 & 0 & 0 \\
-\omega & -\frac{R}{L} & 0 & -\frac{1}{L} & 0 & 0 \\
\frac{1}{C} & 0 & 0 & \omega & -\frac{1}{C} & 0 \\
0 & \frac{1}{C} & -\omega & 0 & 0 & -\frac{1}{C} \\
0 & 0 & \frac{1}{L} & 0 & -\frac{R_L}{L_L} & \omega \\
0 & 0 & 0 & \frac{1}{L_L} & -\omega & -\frac{R_L}{L_L}
\end{bmatrix} \tag{3.4}
$$

$$
B(x) = \begin{bmatrix}
\frac{1}{L} & 0 & 0 & 0 & 0 & 0 \\
0 & \frac{1}{L} & 0 & 0 & 0 & 0
\end{bmatrix}^T \tag{3.5}
$$

$$
C(x) = \begin{bmatrix}
0 & 0 & 1 & 0 & 0 & 0 \\
0 & 0 & 0 & 1 & 0 & 0
\end{bmatrix}^T . \tag{3.6}
$$

Notice that for the isolated operative mode, the system output variables are the V_{c_d} and V_{c_q} voltages, this is, with the objective of regulating the microgrid voltage. In addition, the microgrid frequency ω is included as a system parameter in matrix (3.4). Thus, for control purposes, the microgrid frequency can be either generated by a PLL or predefined by the system operator as described in Figure 3.2. It is important to mention that the distributed generation node (considered to be from renewable sources) for the analysis presented in this research, can be modeled as a constant direct current voltage source, assuming a previous stage of power electronics converters that allows the voltage regulation in a direct current bus link. Additionally, slow variations at

generation node within the time window of analysis are considered.

The Grid Connected Model

The model of the grid-connected microgrid (as seen in Figure 3.2) is obtained when the breakers are closed, and then the DG is connected through a distribution line with the three-phase utility or host grid. Then the dynamic system equations are computed as

$$\begin{aligned} L_s\frac{di_{L_s}}{dt} &= -R_s i_{L_s} - V_c + V_s \\ C\frac{dV_c}{dt} &= i_{L_s} - i_{L_L} - i_{L_g} \\ L_L\frac{di_{L_L}}{dt} &= V_c - R_L i_{L_L} \\ L_g\frac{di_{L_g}}{dt} &= -R_g i_{L_g} + V_c - V_g \end{aligned} \tag{3.7}$$

where i_{L_g} is the grid side current, R_g and L_g are the line resistance and inductance respectively and V_g is the utility grid voltage.Then, system (3.7) in the abc frame has the following representation in the dq0 frame

$$\begin{aligned} \frac{di_{L_{sd}}}{dt} &= -\frac{R_s}{L_s}i_{L_{sd}} - \frac{1}{L_s}V_{c_d} + \frac{1}{L_s}V_{s_d} + \omega i_{L_{sq}} \\ \frac{di_{L_{sq}}}{dt} &= -\frac{R_s}{L_s}i_{L_{sq}} - \frac{1}{L_s}V_{c_q} + \frac{1}{L_s}V_{s_q} - \omega i_{L_{sd}} \\ \frac{dV_{c_d}}{dt} &= \frac{1}{C}i_{L_{sd}} - \frac{1}{C}i_{L_L d} - \frac{1}{C}i_{L_{gd}} + \omega V_{c_q} \\ \frac{dV_{c_q}}{dt} &= \frac{1}{C}i_{L_{sq}} - \frac{1}{C}i_{L_L q} - \frac{1}{C}i_{L_{gq}} - \omega V_{c_d} \\ \frac{di_{L_{Ld}}}{dt} &= \frac{1}{L_L}V_{c_d} - \frac{R_L}{L_L}i_{L_{Ld}} + \omega i_{L_{Lq}} \\ \frac{di_{L_{Lq}}}{dt} &= \frac{1}{L_L}V_{c_q} - \frac{R_L}{L_L}i_{L_{Lq}} - \omega i_{L_{Ld}} \\ \frac{di_{L_{gd}}}{dt} &= -\frac{R_g}{L_g}i_{L_{gd}} + \frac{1}{L_g}V_{c_d} - \frac{1}{L_g}V_{g_d} + \omega i_{L_{gq}} \\ \frac{di_{L_{gq}}}{dt} &= -\frac{R_g}{L_g}i_{L_{gq}} + \frac{1}{L_g}V_{c_q} - \frac{1}{L_g}V_{g_q} - \omega i_{L_{gd}}. \end{aligned} \tag{3.8}$$

Since the microgrid operates in a grid-connected mode with the utility grid, the microgrid's dynamic model must consider the power grid's dynamics. For control purposes, in order to fit a structure suitable for the nonlinear optimal controller design, the electrical power grid is proposed to be mathematically modeled as a known disturbance represented by a set of differential equations via an exo-system described as

$$\frac{dV_{gd}}{dt} = 0, \qquad \frac{dV_{gq}}{dt} = 0. \tag{3.9}$$

With initial conditions $V_{gd}(0) = V_p$ and $V_{gq}(0) = 0$, where V_p is the amplitude of the sinusoidal waveform V_g. In addition, one of the objectives of the grid-connected distributed generator is the active and reactive power-sharing, with the main utility grid regulating the DG's active and reactive power injected into the AC bus. In this sense, the active and reactive power must be considered as the system output and modeled in the dq0 reference frame. Therefore, the active and reactive power of the system are defined as nonlinear functions of the state as follows:

$$\begin{aligned} P_a &= \frac{3}{2}\left(V_{gd} i_{L_{gd}} + V_{gq} i_{L_{gq}}\right) \\ Q_r &= \frac{3}{2}\left(V_{gq} i_{L_{gd}} - V_{gd} i_{L_{gq}}\right). \end{aligned} \tag{3.10}$$

It is worth mentioning that the nonlinear output (3.10) of the system (3.8) is one of the main reasons why it is necessary to apply a nonlinear control strategy in order to regulate the active and reactive output power of the system. Thus by selecting a state vector as

$$x = \left[i_{L_{sd}}\ i_{L_{sq}}\ V_{c_d}\ V_{c_q}\ i_{L_{Ld}}\ i_{L_{Lq}}\ i_{L_{gd}}\ i_{L_{gq}}\ V_{gd}\ V_{gq}\right]^T \tag{3.11}$$

system (3.8)-(3.10) can be represented into the SDCF structure (2.9) considering the following state-dependent matrices.

$$A(x) = \begin{bmatrix} -\frac{R_s}{L_s} & \omega & -\frac{1}{L_s} & 0 & 0 & 0 & 0 & 0 & 0 & 0 \\ -\omega & -\frac{R_s}{L_s} & 0 & -\frac{1}{L_s} & 0 & 0 & 0 & 0 & 0 & 0 \\ \frac{1}{C} & 0 & 0 & \omega & -\frac{1}{C} & 0 & -\frac{1}{C} & 0 & 0 & 0 \\ 0 & -\frac{1}{C} & -\omega & 0 & 0 & -\frac{1}{C} & 0 & -\frac{1}{C} & 0 & 0 \\ 0 & 0 & \frac{1}{L_L} & 0 & -\frac{R_L}{L_L} & \omega & 0 & 0 & 0 & 0 \\ 0 & 0 & 0 & \frac{1}{L_L} & -\omega & -\frac{R_L}{L_L} & 0 & 0 & 0 & 0 \\ 0 & 0 & \frac{1}{L_g} & 0 & 0 & 0 & -\frac{R_g}{L_g} & \omega & -\frac{1}{L_g} & 0 \\ 0 & 0 & 0 & \frac{1}{L_g} & 0 & -\frac{R_g}{L_g} & -\omega & 0 & 0 & -\frac{1}{L_g} \\ 0 & 0 & 0 & 0 & 0 & 0 & 0 & 0 & 0 & 0 \\ 0 & 0 & 0 & 0 & 0 & 0 & 0 & 0 & 0 & 0 \end{bmatrix} \tag{3.12}$$

$$B(x) = \begin{bmatrix} \frac{1}{L_s} & 0 & 0 & 0 & 0 & 0 & 0 & 0 & 0 & 0 \\ 0 & \frac{1}{L_s} & 0 & 0 & 0 & 0 & 0 & 0 & 0 & 0 \end{bmatrix}^T$$

$$C(x) = \frac{3}{2}\begin{bmatrix} 0 & 0 & 0 & 0 & 0 & 0 & V_{gd} & V_{gq} & 0 & 0 \\ 0 & 0 & 0 & 0 & 0 & 0 & V_{gq} & -V_{gd} & 0 & 0 \end{bmatrix}.$$

For the grid-connected mode, it is important to mention that the system output is chosen in order to generate nonlinear functions of the state as they are the active and reactive power in the dq0 frame. Then it is possible to apply a nonlinear optimal and robust control technique (2.23)-(2.25) for both microgrid operative modes.

3.1.2. Simulation Results

The proposed microgrid control scheme is based on the block diagram shown in Figure 3.2, which depicts the control structure of the microgrid during the isolating and grid-connected operative mode, where a phase-locked loop (PLL)[2] is used in order to synchronize the operative frequency ω of the microgrid with the main power grid frequency ω_{grid}. Nonetheless, for the isolated condition (if required), it is possible to define a different operative frequency ω_{ref} to the system depending on the load requirements (i.e., 60 or 50 Hz). Then according to the operating condition, one of the two different microgrid models: (3.2) for the VF controller or (3.8)-(3.9) for the PQ controller is chosen, and then the nonlinear optimal and robust control law (2.23)-(2.25) is calculated and the control law is modulated via a PWM strategy in order to control a three-phase full-bridge inverter, which interfaces the DGs node (i.e., battery, fuel cell, PV array) to the load during the isolated condition or to the main power grid as an ancillary service for active and reactive power compensation as will be discussed in Chapter 4.

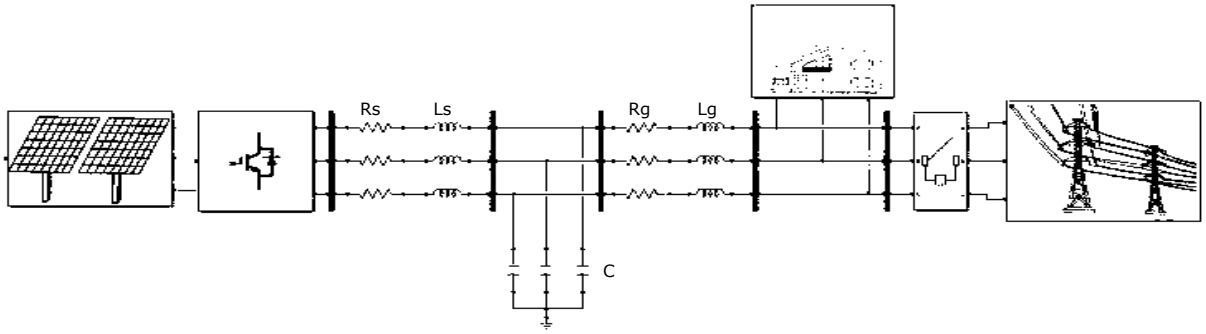

Figure 3.3: Proposed microgrid configuration.

A Simulation was carried out by using MATLAB/Simulink®, considering the proposed microgrid models (3.2) and (3.8)-(3.9), with the system parameters as described in Table 3.1. Then the microgrid simulation was conducted as follows:

[2] *Wherein literature different efficient and fast phase-locked loop mechanism (PLL) have been reported, as seen in [Ghartemani, 2014], even, specialized electrical simulation tools include PLL as part of their simulation libraries (e.g., MATLAB/Simulink)®.*

Table 3.1: Microgrid system parameters, [Fan, 2017]

Main parameters of the simulated system	
Filter	$L_s = 0.04H$, $R_s = 0.02\Omega$ $C = 1000\mu F$.
Load	$R_L = 3\Omega$, $L_L = 0.01H$
Grid	$V_g = 120V_{rms}$, $R_g = 0.02\Omega$ $L_g = 0.04H$

The Microgrid Voltage and Frequency Control

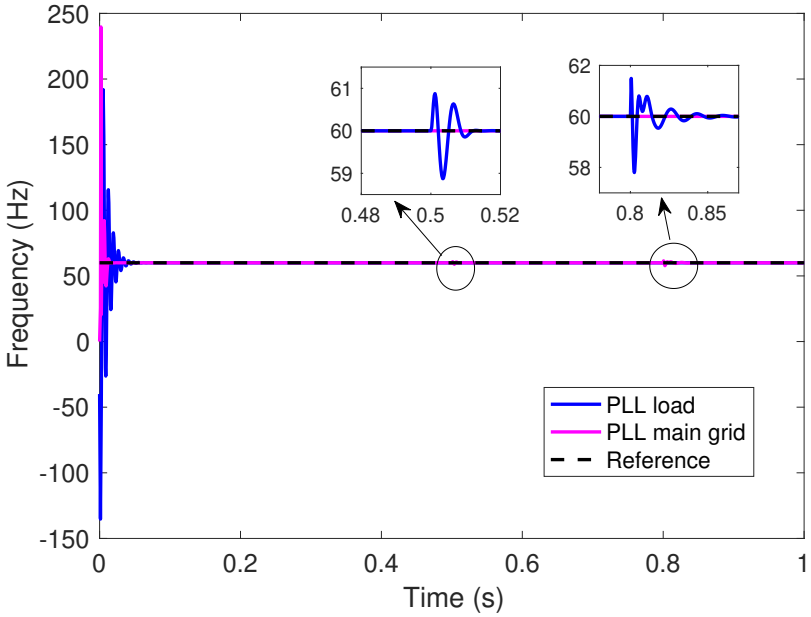

Figure 3.4: Measured frequency of the load during the isolated microgrid operation.

During the isolated operation mode, the microgrid frequency ω can be operated either synchronized with the main utility grid ω_{grid} given by a PLL or given by an arbitrary frequency reference ω_{ref}. In order to verify the effectiveness of the frequency control, a PLL estimates the grid frequency ω_{grid} and then is used as the reference signal to the controller as seen in Figure 3.4, where the load frequency is synchronized with the main power grid at $60Hz$, at $t = 0.5$ it is possible to appreciate how the controller compensates the sudden load change and continues regulating the frequency $f = 60$ Hz at the reference set point synchronized with the main utility grid. At the beginning of the simulation, a transitory effect can be seen in estimating the frequency; this is due to the PLL of the simulation block since it requires a convergence time since it was not initialized in steady state conditions. Firstly during the isolated operation mode a three-phase load was connected to the DG where the main control objective

is to regulate the load voltage and frequency, by applying the nonlinear optimal and robust control law (2.23)-(2.25) with the controller gains defined as $Q = [10, 0; 0, 10]$, $R = [10, 0; 0, 10]$, $Q_{I_1} = 1000$ and $Q_{I_2} = 1000$.

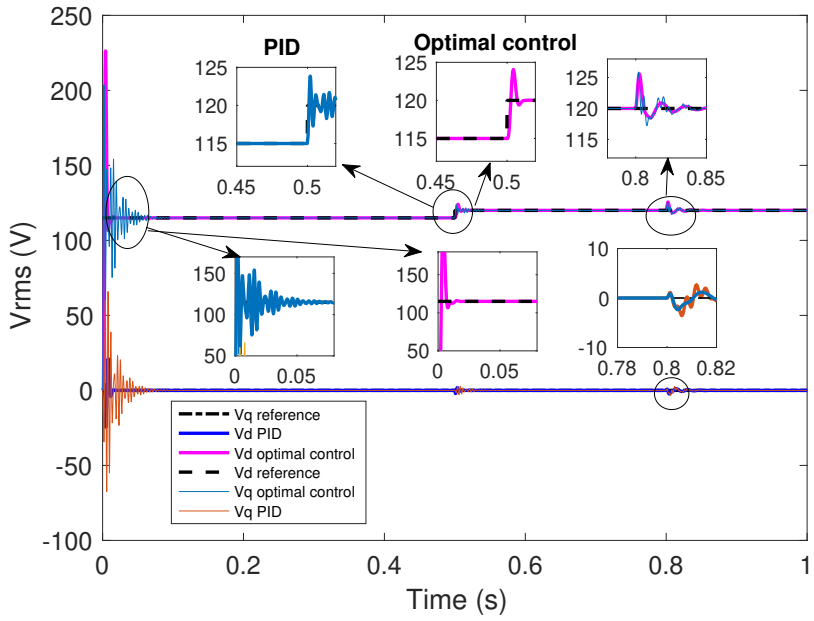

Figure 3.5: Load voltage regulation during the isolated microgrid operation in the dq0-frame.

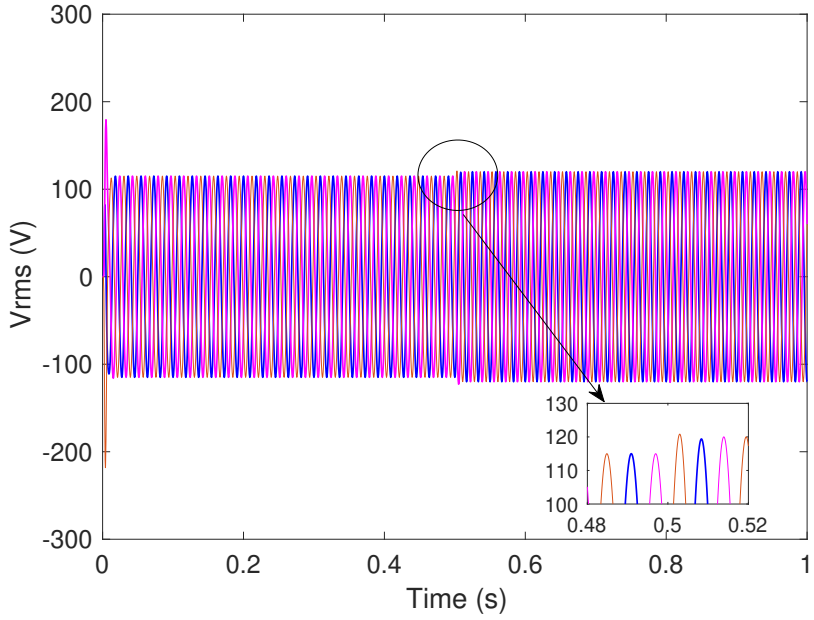

Figure 3.6: Load voltage regulation during the isolated microgrid operation mode in the abc frame.

Figure 3.5 depicts the load voltage regulation in the dq0 frame where the $q-$ axis voltage was set to zero and $d-$ voltage changes the reference according to $t < 0.5s \rightarrow$

$v_d = 115Vrms$ and $t > 0.5s \rightarrow v_d = 120Vrms$. In order to demonstrate the control tracking capabilities, and the robustness properties of the nonlinear optimal robust controller (2.23)-(2.25), a sudden load change was simulated by considering load steps changing the resistance and inductance load from $R_L = 3$ to $R_L = 6$ and $L_L = 0.01H$ to $L_L = 0.1H$ respectively at $t = .8s$, which are uncertain parameters and the controller was able to compensate. Also, a PID simulation based on the nested-control loops is presented in order to compare the performance of the proposed nonlinear control scheme against a classical linear controller. Figure 3.6 depicts the voltage regulation in the abc frame, wherein the zoom area it is possible to appreciate the voltage regulation to the desired set point.

Microgrid Active/Reactive Power Control

During the grid-connected operation mode, the control objective changes since the load voltage and frequency are imposed by the main utility grid. Therefore, for this operative condition, the control objective is to inject or absorb active/reactive power according to predefined reference set points (or commanded by an outer control loop as will be described in Chapter 4). The nonlinear optimal robust controller (2.23)-(2.25) is used with the controller gains selected as $Q = [10, 0; 0, 10]$, $R = [500, 0; 0, 500]$, $Q_{I_1} = 1000$ and $Q_{I_2} = 1000$.

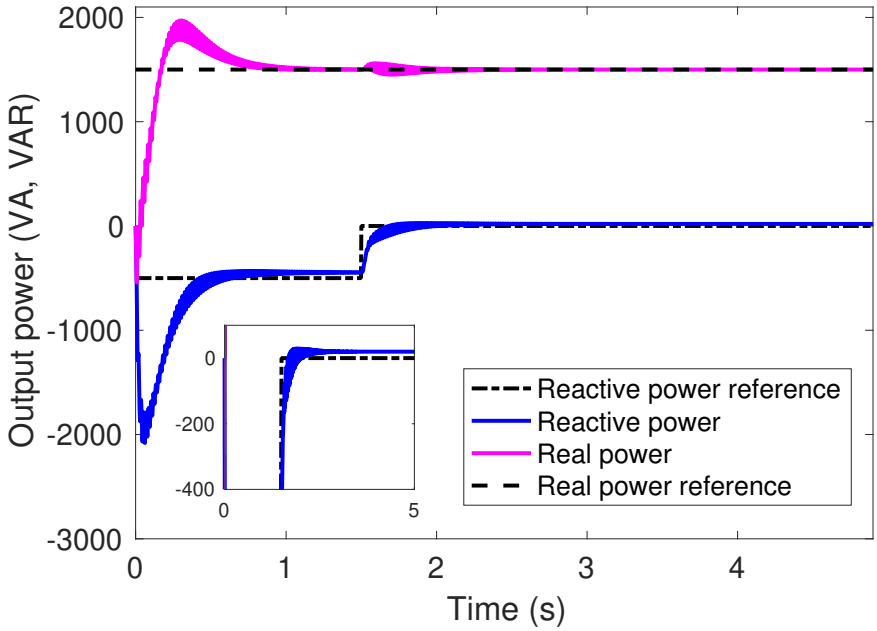

Figure 3.7: Active and reactive output power of the system during the grid-connected microgrid operation mode.

In order to demonstrate the effectiveness of the proposed microgrid power controller,

a constant active power reference $P_a = 1.5$ KW is injected into the main utility grid while the reactive power Q_r firstly absorbs 500 VAR and then is set to zero VAR, as seen in Figure 3.7. The reactive power absorption demonstrates the capability to absorb reactive power, which is an important result that will be applied later to provide microgrid ancillary services.

It is worth mentioning that the main objective of the nested voltage and current control loops used for microgrid control scheme based on linear controllers as seen in [Fan, 2017],[Hatziargyriou, 2014], it is to regulate the microgrid circulating current. Nonetheless, by using the proposed nonlinear optimal and robust controller is possible to modulate the control effort or even establish a quote for the control expenditure to avoid excessive currents. For the case of the isolated mode, the proposed control strategy offers advantages against the nested voltage and current control loops in terms of optimizing the error and control expenditure and the simplicity and robustness of the controller capable to reject parametric uncertainties. For the case of the grid-connected operation mode, the nonlinear output of the system can be controlled in terms of a tracking problem by following the maximum power point tracking MPPT [Sangwongwanich and Blaabjerg, 2019], which could extend the results given in this section and its considered for future research.

3.2 Energy Storage System Control

This section presents the application of a nonlinear optimal control strategy for an energy storage system within a DC microgrid based on renewable energy, which includes an energy storage device built on supercapacitors. The main objective of the proposed control strategy is the voltage regulation over a DC bus link, which is possible by the compound microgrid architecture where a supercapacitor-based energy storage device is interfaced through a bidirectional DC/DC power electronic converter, which is commanded by an intelligent controller that selects the proper operative modes of the bidirectional DC/DC converter (charging/discharging mode) in order to regulate the DC bus link voltage and the supercapacitor charging strategy. It is essential to mention that within a microgrid based on renewable energies, the proposed storage unit aims to compensate fluctuations or interruptions at the generation due to renewable energies during a predefined time interval based on the capacity of the energy storage unit. Simulation results demonstrate the effectiveness of the proposed control strategy, emulating a distributed generation loss and the backup from the energy storage device.

3.2.1. Proposed Energy Storage System Configuration

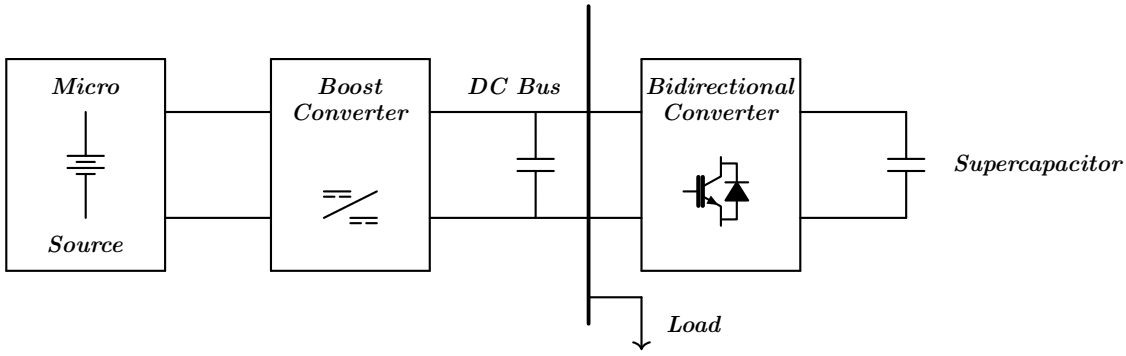

Figure 3.8: Proposed microgrid energy storage system with supercapacitors.

The proposed energy storage system, as depicted in Figure 3.8, considers the objective of efficiently transferring electric power between the microgrid subsystems, where the different subsystems can store, generate or consume electric power. In order to achieve the energy transfer between the microgrid elements, a common practice is to assume that the power system operates under a steady-state condition, as described in [Sanchez-Squella et al., 2010]. Then the electric power demanded by the multiports (which are the componets connected to the microgrid) is transformed into current or voltage references. Traditionally these references are controlled via nested control loops mainly based on PID linear controllers as seen in [Ahshan et al., 2020, Xiao et al., 2015]. Due to the linear controller, the different time responses are decoupled into fast and slow dynamics, with limited operational ranges. Nonetheless, during transients or when fast dynamic responses are required, the performance of classical linear controllers might be far from satisfactory. In this sense, this thesis proposes the use of nonlinear optimal and robust controllers to effectively achieve the electric power transfer between an energy storage device and the microgrid multiports. It is worth mentioning that this thesis considers the use of supercapacitors or double-layer capacitors as an energy storage device, which are envisaged as a promising energy storage technology with desirable characteristics such as power density and a high degree of recyclability [Zhang et al., 2018a].

3.2.2. Supercapacitor Design Specifications

For the proper design of an energy storage system based on supercapacitors, the first step is to size the supercapacitors array necessary to satisfy the energy demand based on the voltage drop that the microgrid DC bus may experience. The supercapacitor sizing procedure is conducted as follows.

Supercapacitor Sizing

Due to the requirements to compensate the fluctuation or interruption in the energy generation by renewable sources, it is necessary to design the storage unit based on the energy capacity to guarantee voltage regulation in the microgrid during a specific time interval. In this sense, for the case of supercapacitors, this energy depends on the size of the capacitor, which is obtained through series and parallel capacitor arrangements. The sizing procedure of a supercapacitor based on its energy requirements is described below. Consider the supercapacitor model (2.59), then the energy stored in the supercapacitor at a specific moment (neglecting the supercapacitor series resistance) can be expressed as

$$E_{sc} = \frac{1}{2} C_{sc} V_{sc}^2 = \frac{1}{2} \frac{N_{p_{sc}}}{N_{s_{sc}}} C_{sc} V_{sc}^2 \tag{3.13}$$

where V_{sc} is the supercapacitor array voltage, $N_{p_{sc}}$ and $N_{s_{sc}}$ are the number of parallel and series supercapacitor branches respectively and C_{sc} is a single supercapacitor capacity. It is important to notice that the energy stored in a supercapacitor is directly proportional to the square of the voltage as described in (3.13). In addition, losses in the DC-DC Boost converter power and internal losses due to the equivalent resistance need to be taken into account (a topic that is beyond the scope of this research). Therefore considering the allowable limits in which the discharging process takes place, then the variation of the energy ΔE_{sc} stored in the supercapacitor array is defined as

$$\Delta E_{sc} = \gamma \frac{1}{2} C_{eq} \left[V_{sc_{max}}^2 - V_{sc_{min}}^2 \right] \tag{3.14}$$

being C_{eq} is the equivalent supercapacitor array capacitance, γ is the supercapacitor pack efficiency, $V_{sc_{max}}$ and $V_{sc_{min}}$ are the maximum and minimum supercapacitor pack voltage, respectively.

Supercapacitor State of Charge Calculation

Precise metering of the supercapacitor state of charge (SOC) can allow the energy management systems or intelligent chargers to make a better use of the supercapacitor stored power without incurring on supercapacitor overcharge or over-discharge and other potential hazards. Different from conventional capacitors, supercapacitors exhibit a nonlinear relationship between the supercapacitor terminal voltage and the SOC. Different estimation techniques are used for SOC estimation, such as artificial neural networks [Zhao et al., 2020] and Kalman filter methods [CHI, 2013]. Nonetheless, for the purposes of this thesis, the extended Kalman filter (EKF) [Huang et al., 2018] will be used for SOC estimation technique[3].

[3] *It is important to mention that the development of SOC estimation techniques is beyond the scope of this thesis since this thesis is focused on the control algorithm design for the power electronic converters.*

Extended Kalman Filter

The extended Kalman filter algorithm has demonstrated to be an efficient and robust observer for nonlinear systems, as in the case of voltage and temperature in supercapacitors. For SOC estimation via Kalman filter, it is necessary to consider the supercapacitor extended model which includes the thermal and SOC dynamics as seen in [CHI, 2013] described as

$$\begin{aligned} \dot{\mathcal{X}} &= f(\mathcal{X}, u) + \mathcal{W}(t) \\ \mathcal{Z} &= h(\mathcal{X}, u) + \mathcal{V}(t) \end{aligned} \tag{3.15}$$

where f and h are nonlinear functions of the extended states and the system input, $\mathcal{X}$ is an extended state vector consisting of the estimated states, $\mathcal{Z}$ is the measured output, $\mathcal{W}$ is the process noise, and $\mathcal{V}$ is the measured noise. In this sense, the supercapacitor extended model considering the thermal effects and the SOC dynamics, written into the space-state representation is given by

$$\begin{aligned} \begin{bmatrix} \dot{\text{SOC}} \\ \dot{V}_1 \\ \dot{V}_2 \\ \dot{\mathcal{T}} \end{bmatrix} &= \begin{bmatrix} 0 & 0 & 0 & 0 \\ 0 & -\pi^2 \frac{1}{\tau} & 0 & 0 \\ 0 & 0 & -4\pi^2 \frac{1}{\tau} & 0 \\ 0 & \frac{\pi^2 V_1 C}{2C_{heat}\tau} & \frac{2\pi^2 V_2 C}{C_{heat}\tau} & -\frac{Ah}{C_{heat}} \end{bmatrix} \begin{bmatrix} \text{SOC} \\ V_1 \\ V_2 \\ \mathcal{T} \end{bmatrix} + \begin{bmatrix} \frac{1}{C(V_{c,max} - V_{c,min})} \\ \frac{2}{C} \\ \frac{2}{C} \\ \frac{2k_b a T}{eC_{heat}} + \frac{R_s i}{C_{heat}} \end{bmatrix} i \\ &\quad + \begin{bmatrix} 0 \\ 0 \\ 0 \\ \frac{AhT_0}{C_{heat}} \end{bmatrix} \mathcal{W}(t) \\ V_T &= \begin{bmatrix} V_{c,max} - V_{c,min} & 1 & 1 & 0 \end{bmatrix} \begin{bmatrix} \text{SOC} \\ V_1 \\ V_2 \\ \mathcal{T} \end{bmatrix} + R_s i + V_{c,min} + \mathcal{V}(t) \end{aligned} \tag{3.16}$$

where C is the capacitance, τ is a time constant, $\mathcal{T}$ is the temperature of the supercapacitor, $\mathcal{T}_0$ is the ambient temperature, C_{heat} is the heat capacitance of the supercapacitor, A is the effective heat transfer area of the supercapacitor and h is the heat transfer coefficient of the supercapacitor. It is important to mention that despite the complexity of the model, the supercapacitor states can be estimated through a nonlinear estimator such as the Kalman filter.

However, efficient Kalman filter algorithms are available in different software suites toolboxes such as MATLAB/Simulink®.

3.2.3. The Energy Storage Control Scheme

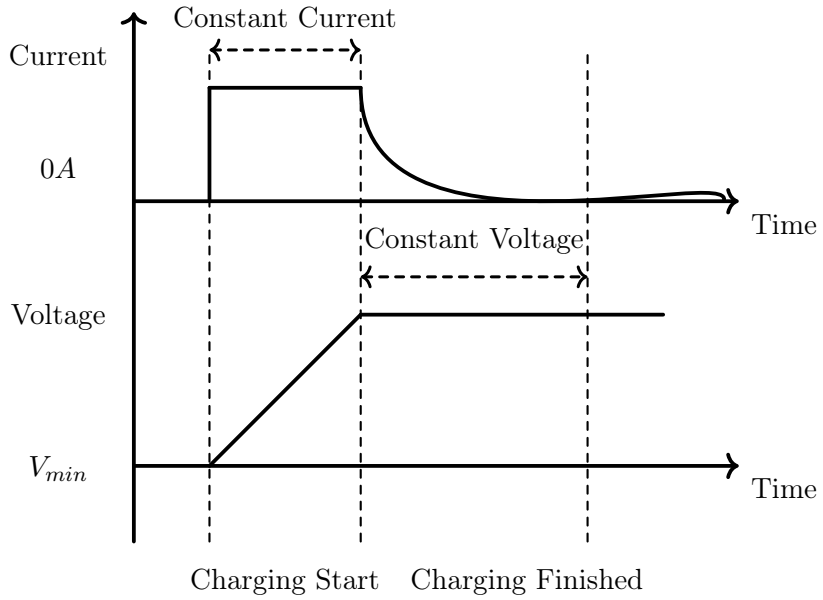

Figure 3.9: Supercapacitor charging cycle.

Various methodologies are used to charge a supercapacitor, such as the constant current/constant voltage (CICV) method [Chun et al., 2018] which is one of the most commonly used techniques shown in Figure 3.9. Where the SC is charged to a target voltage, therefore accurately charging controllers needs to be implemented in order to avoid overcharging by means of appropriate control strategies. Through a combination of constant current and constant voltage methods, the charger limits the current to a preset level until the supercapacitor reaches its nominal voltage, and then the current reduces as the supercapacitor becomes fully charged. This method is illustrated in Figure 3.9. Excessive current or voltage can reduce the lifetime of supercapacitors. When charged with a constant current, a supercapacitor will hold a voltage that rises linearly with time. Supercapacitors can typically accept a wide range of charging currents, reducing the need for precision current control but still requiring that charging stops when the device reaches its maximum rated voltage. Typically, charging is performed during an initial constant-current charging phase followed by a constant-voltage phase, as seen in Figure 3.9. During the constant-current phase, supercapacitor chargers typically measures the output current by monitoring the voltage across an external sensing resistor. An internal voltage regulator provides precise control over the voltage charging strategy. Despite supercapacitors offer a limited voltage output, designers often combine supercapacitors in series to achieve higher voltage levels during normal operation. However, basic differences in individual supercapacitors can lead to voltage imbalances that can degrade the lifetime of these devices or even to damage them.

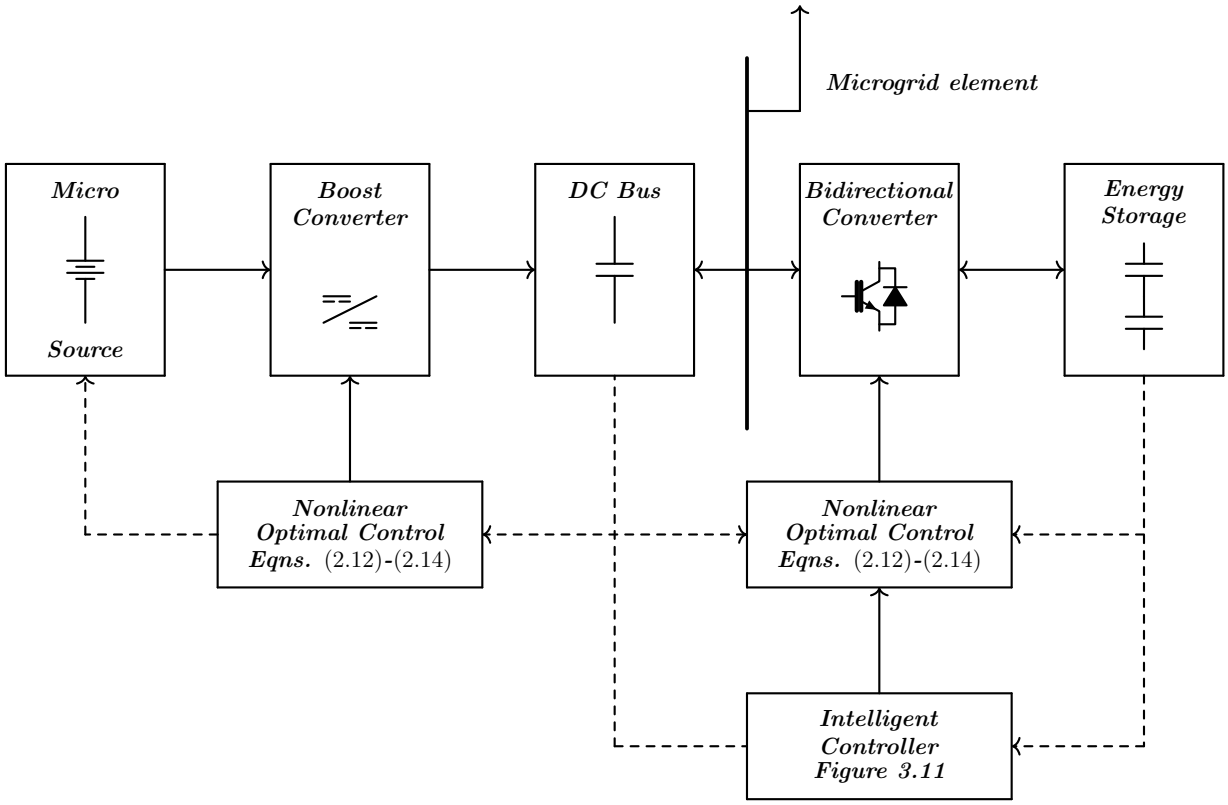

Figure 3.10: Proposed microgrid system configuration with energy storage system.

3.2.4. A Case of Study: Energy Storage System Based on Supercapacitors

Consider the microgrid configuration as depicted in Figure 3.10, which represents the proposed dynamic energy storage configuration under study. The microgrid consists of a distributed generation unit (i.e., photovoltaic plant, fuel cell, flywheel), which generates electrical power at a specific DC level. Then the voltage generated by the distributed generation unit is converted into a higher DC level through a Boost converter to regulate the voltage on the DC bus through the nonlinear optimal control strategy (2.12)-(2.14). Likewise, a bidirectional power electronic converter and an electric load are connected to the DC bus (or to a later stage of the microgrid, such as a power electronic inverter). The bidirectional power electronic converter controls the power flow between the energy storage system based on supercapacitors and the DC bus through an intelligent controller that determines the system status and commands reference signals to a local nonlinear optimal control scheme as described in Figure 3.11.

Boost Converter

Consider the Boost converter dynamic model (2.57). Where the switching variable u_1 is a high-frequency square-waveform of period T and duty cycle $\mu \in (0, 1)$. In this sense, averaging can be used to approximate (2.57). Therefore the dynamics of the Boost

converter averaged model can be rewritten as

$$\begin{aligned} L\frac{di_L}{dt} &= -(1-\mu)v_o + V_{dc} \\ C\frac{dv_o}{dt} &= (1-\mu)i_L - \frac{v_o}{R_L}. \end{aligned} \tag{3.17}$$

Therefore, in order to have a suitable model representation for the application of the nonlinear optimal tracking control scheme, it is possible to rewrite (3.17) into the SDCF (2.9) by selecting the state vector as

$$x = \begin{bmatrix} i_L & v_o \end{bmatrix} \tag{3.18}$$

then system (3.17) can be described as

$$\begin{aligned} \begin{bmatrix} \dot{x}_1 \\ \dot{x}_2 \end{bmatrix} &= \begin{bmatrix} 0 & -\frac{1}{L} \\ \frac{1}{C} & -\frac{1}{CR_L} \end{bmatrix} \begin{bmatrix} x_1 \\ x_2 \end{bmatrix} + \begin{bmatrix} \frac{v_o}{L} \\ -\frac{i_L}{C} \end{bmatrix} u \\ y &= \begin{bmatrix} 1 & 0 \end{bmatrix} \begin{bmatrix} x_1 \\ x_2 \end{bmatrix}. \end{aligned} \tag{3.19}$$

Hereinafter, for control purposes, the averaged control signal μ will be represented as a control input signal u.

Bidirectional Power Electronic Converter

The bidirectional power electronic converter averaged model is defined as follows.

$$\begin{aligned} \frac{di_L}{dt} &= -\frac{r}{L}i_L - \frac{1}{L}v_B + \frac{V_{bus}}{L}\mu \\ \frac{dv_B}{dt} &= \frac{1}{C}i_L - \frac{1}{R_sC}v_B + \frac{1}{R_sC}v_C \\ \frac{dv_C}{dt} &= \frac{1}{R_sC_b}v_B - \left(\frac{1}{R_pC_b} + \frac{1}{R_sC_b}\right)V_{dc} \end{aligned} \tag{3.20}$$

where i_L, v_B and v_C are the inductor current, the capacitor voltage, and the supercapacitor voltage, respectively, the function μ is the average value of Θ. By selecting a state vector as

$$x = \begin{bmatrix} i_L & v_B & v_c \end{bmatrix} \tag{3.21}$$

The state-space representation of the bidirectional power electronic converter (3.20) is given as

$$\begin{bmatrix} \dot{x}_1 \\ \dot{x}_2 \\ \dot{x}_3 \end{bmatrix} = \begin{bmatrix} -\frac{r}{L} & -\frac{1}{L} & 0 \\ \frac{1}{C} & -\frac{1}{R_B C} & \frac{1}{R_B C} \\ 0 & \frac{1}{R_B C_B} & -\left(\frac{1}{R_B C_B} + \frac{1}{R_p C_B}\right) \end{bmatrix} \begin{bmatrix} x_1 \\ x_2 \\ x_3 \end{bmatrix} + \begin{bmatrix} \frac{V_{dc}}{L} \\ 0 \\ 0 \end{bmatrix} u \tag{3.22}$$

with the system output

$$y = \begin{bmatrix} 0 & 1 & 0 \end{bmatrix} \begin{bmatrix} x_1 \\ x_2 \\ x_3 \end{bmatrix}. \tag{3.23}$$

The Intelligent Charger Controller

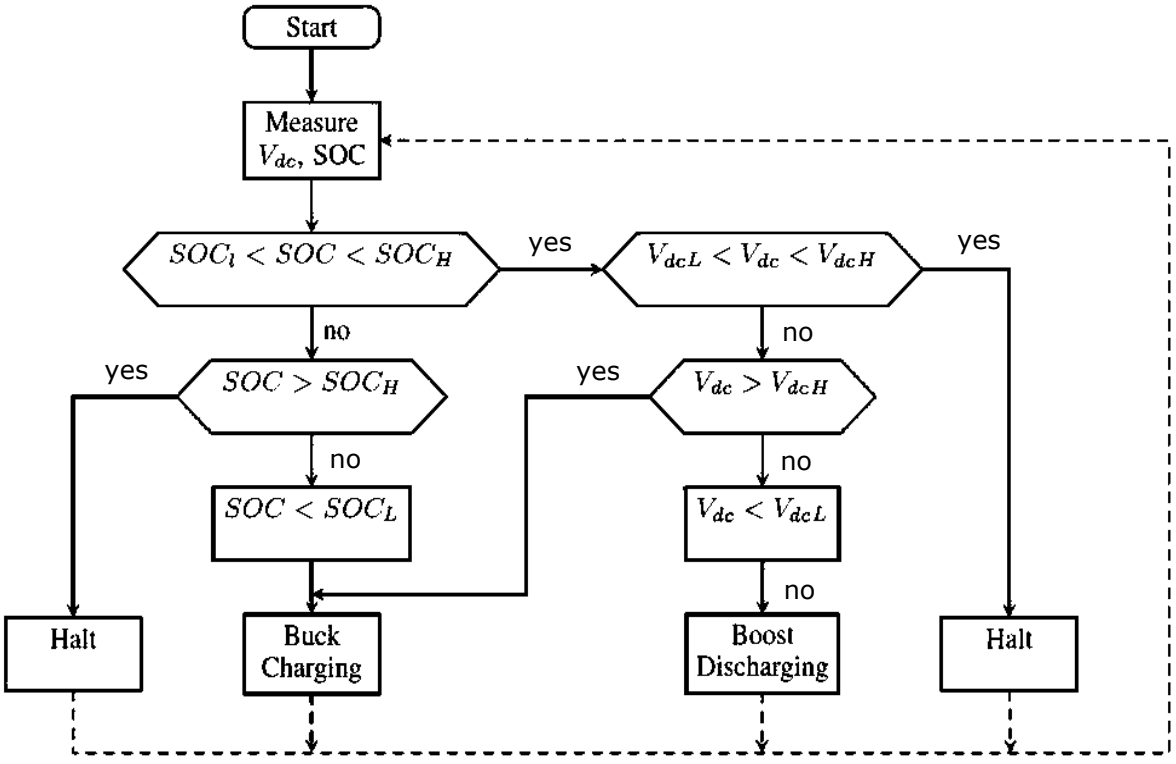

Figure 3.11: Intelligent controller system flowchart.

Given the nature of the bidirectional converter, it is necessary to switch between the two operating modes of the bidirectional converter to achieve the charge and discharge of the storage unit. In this sense, it is necessary to use a PWM-type modulation strategy which is proposed for this thesis, as shown in Figure 3.12, where ζ is a function defined in order to commute between the Buck and Boost structure of system (3.20). For this thesis, it is proposed that the command signal ζ is provided by a higher control

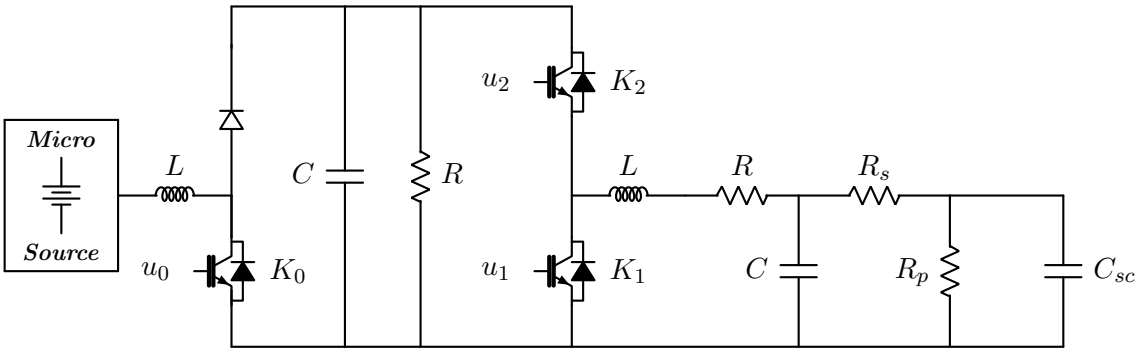

Figure 3.13: Proposed microgrid energy storage system with supercapacitors.

entity (intelligent controller) which decides whether to commute between the different converter operative modes based on local measurements as seen in Figure 3.11.

The intelligent charging controller described in Figure 3.11 is based on the measurement of the supercapacitor SOC, analyzing if it is within the operating limits (SOC_l, SOC_H), as well as the voltage level in the direct current link V_{dc}. Depending on the available resources in terms of energy, the bidirectional converter will switch its structure between: a) buck type converter to charge the supercapacitor if the SOC is lower than the established limit and if the voltage level in the DC link allows it; or b) the converter will behave as a Boost type converter to regulate the voltage in the direct current link if the energy capacity of the supercapacitor allows it.

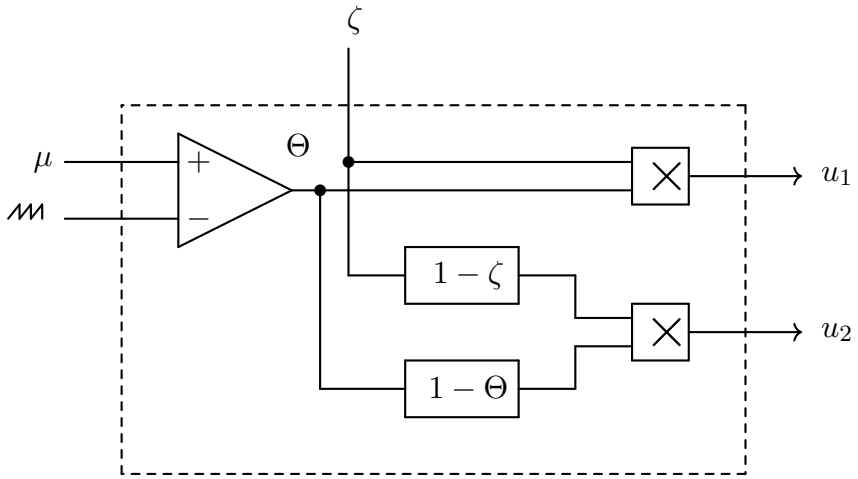

Figure 3.12: Proposed PWM scheme.

3.2.5. Simulation Results

In order to demonstrate the effectiveness of the proposed energy storage control scheme, a simulation-based on MATLAB/Simulink® was conducted as follows; Consider the energy storage microgrid system configuration as depicted in Figure 3.13 with the system parameters shown in Table 3.2, which consists of a distributed generation node,

Table 3.2: Energy storage system parameters, [Rachid et al., 2017].

Main parameters of the simulated system	
Boost converter	$L_b = 0.0586H$
DC bus	$R = 10\Omega$, $C = 10000\mu F$
Bidirectional converter	$L_c = 0.0586H$, $R_c = 0.1\Omega$ $C_c = 700\mu F$
Supercapacitor	$R_s = 0.06\Omega$, $R_p = 1k\Omega$ $C_{sc} = 60F$

generating electrical power at a DC level where the case of an abrupt interruption at the generation-side is considered. The objective of the proposed system is to regulate the voltage in the DC bus of the microgrid to a higher voltage level than that generated by the distributed generation node. At the same time, depending on an intelligent control strategy, recharge an energy storage unit based on supercapacitors using the charging strategy described in Figure 3.9. Additionally, at the moment of interruption in the generation, the control scheme must regulate the voltage on the DC bus through the stored energy. It is essential to mention that the supercapacitor was sized according to the sizing procedure described in this Chapter, considering a 15s voltage interruption, a reference voltage of $300V$, and the load power consumption, considering the supercapacitor parameters given in [Rachid et al., 2017]. The nonlinear optimal control strategy (2.12)-(2.14) shown in Figure 3.10 is considered for this simulation.

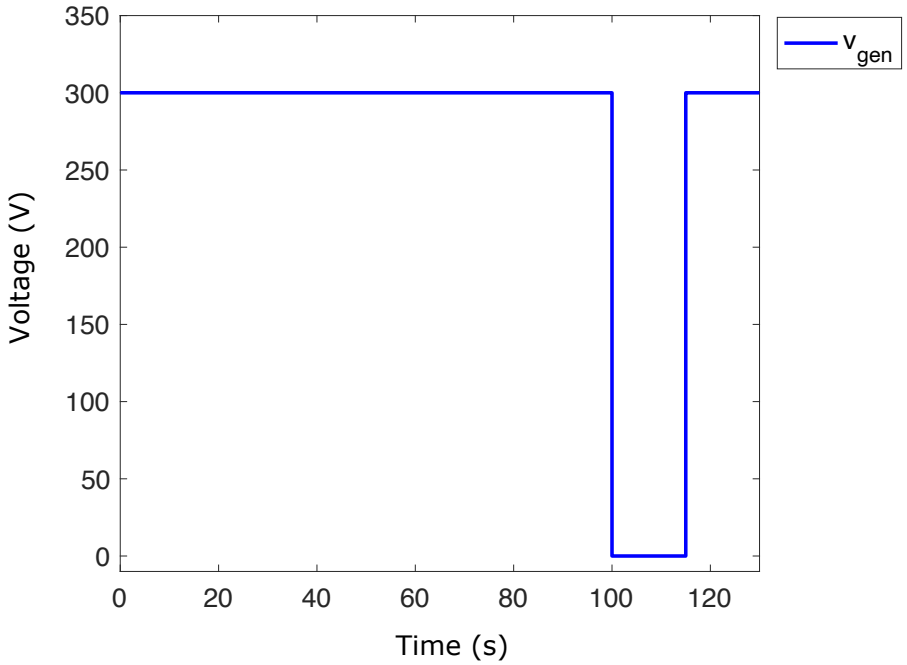

Figure 3.14: Distribute generation voltage interruption.

Figure 3.14 shows the voltage generated at the distributed generation unit, where during $t < 100s$ there is a generation voltage of 300V DC. Later, in an interval of

15s, an abrupt disconnection occurs at the generation (which commonly occurs when the distributed generation node voltage level is less than a preset threshold voltage.), and later, at $t > 115s$, the voltage is restored to the same level of 300V DC. It is important to mention that this behavior emulates the dynamics of a generation source based on renewable energy, where the system may be disconnected as it does not have a generation voltage level higher than a threshold voltage.

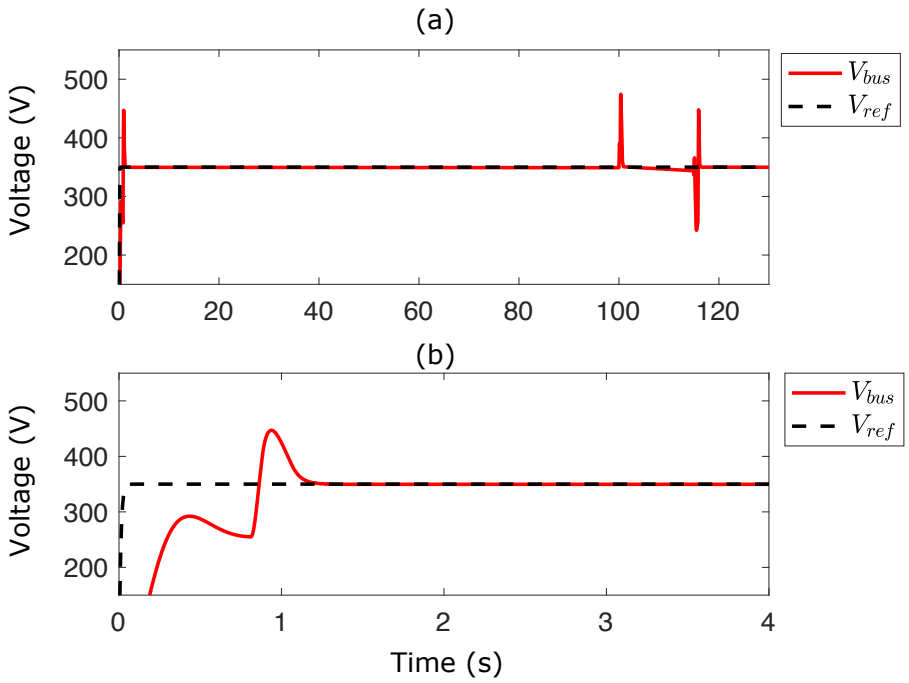

Figure 3.15: (a) DC bus voltage regulation; (b) transient response of DC bus link voltage regulation.

Figure 3.15 shows the voltage regulation on the DC bus at a level of 350V. This is through the action of the Boost converter boosting the generation voltage through the nonlinear optimal control strategy (2.12) - (2.14). In Figure 3.15, it can be observed how after a small transient (due to the initial voltage conditions of the DC bus link), the voltage regulation is achieved at the desired level. Additionally, during the time interval $100 < t < 115s$ the voltage regulation is achieved in the event of the abrupt disconnection of the generation node, through the energy stored in the storage unit, the transients show the disconnection instants of the generation source and the moment when it is reconnected switching the backup source with the generation node. It is important to highlight the performance of the nonlinear optimal tracking controller minimizing the steady state error regulating to a predefined voltage level at the DC bus link. However, to avoid the activation of protection systems due to transients in the voltage regulation on the DC bus, the controller gains can be adjusted in order to obtain the desired response, however the error in steady state can be compromised.

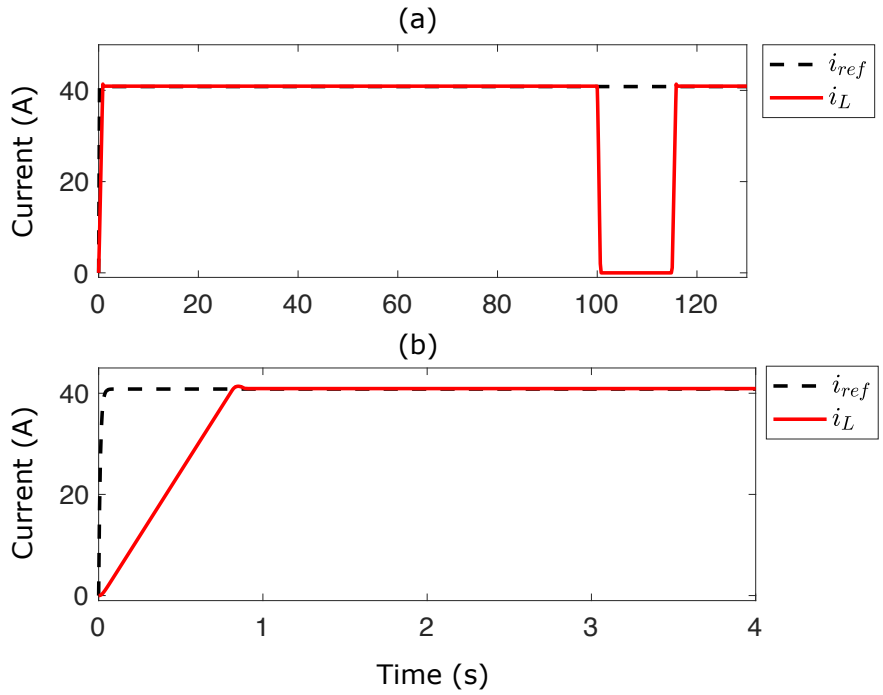

Figure 3.16: (a) Nonlinear optimal tracking current control; (b) zoom region of the transient response.

It is important to mention that given the nonminimum phase nature of the Boost converter, the voltage control is performed indirectly through a current control loop as described in equation (4.35). In such a way that by means of the reference voltage in the DC bus $V_{ref} = 350V$, the generation voltage V_{DC} and the DC bus resistance, a current reference of $i_{ref} = 40A$ is required. Figure 3.16 shows that by means of the nonlinear optimal control strategy (2.12) - (2.14) with the controller gains parameters selected as $Q = 100$ and $R = 1$, the reference current is tracked and as a consequence the voltage regulation is achieved as shown in Figure 3.15. During the interval $100 < t < 115s$, it is shown how the current drops to zero, this is due to the disconnection of the distributed generation node and at that moment, the Boost converter (from the distributed generation side) does not inject current to the DC bus link.

Figures 3.17 and 3.18 show the nonlinear optimal tracking control over the bidirectional converter of the energy storage unit based on supercapacitors, where according to the intelligent control scheme shown in Figure 3.11. It is considered that while the distributed generation node regulates the voltage in the DC bus through the Boost converter, the charging process of the storage unit begins. In this sense, the bidirectional converter behaves like a Buck converter, which by means of the constant current-constant voltage charging strategy shown in Figure 3.9, the charging current that flows from the DC bus to the supercapacitor is first regulated with charging current reference $i_{ref} = 5A$ shown in Figure 3.17. Later, when the nominal voltage level of the supercapacitor $V_{sc} = 300V$ is reached, the current drops to zero, and the voltage is regulated shown in

Figure 3.18. For the bidirectional control scheme, the nonlinear optimal control was designed considering the control gains selected as $Q = 10$ and $R = 1$.

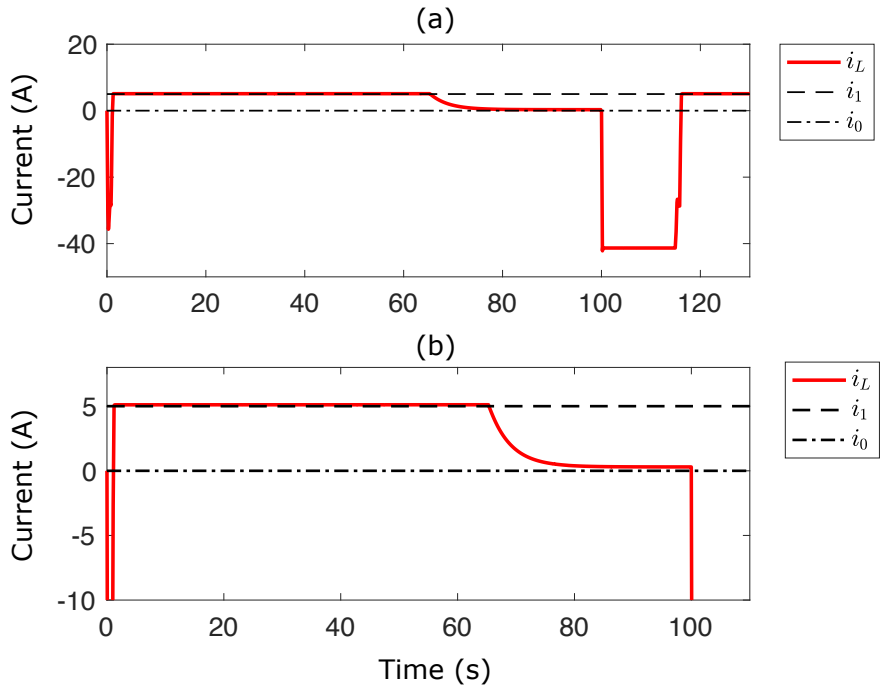

Figure 3.17: Supercapacitor constant current charging process.

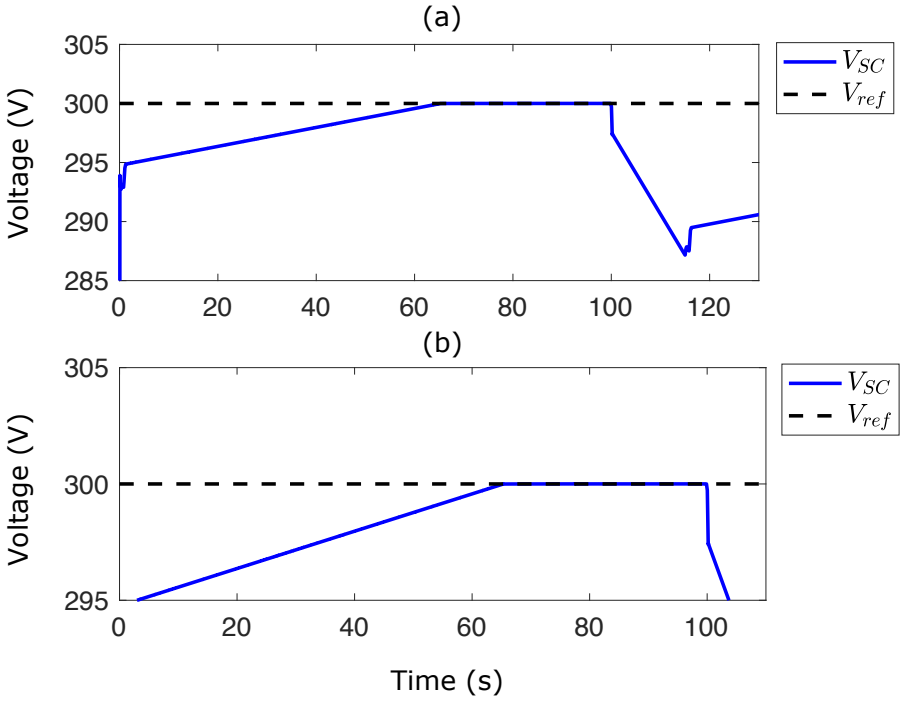

Figure 3.18: Supercapacitor constant voltage charging process.

3.3 Summary

This Chapter describes the nonlinear optimal control strategies to design local controllers of power electronic converters in microgrids. In a first instance, the control of a microgrid is shown during two microgrid operative modes: grid-connected and isolated modes. Simulation results show how efficiently the nonlinear optimal control guarantees the different control objectives in both microgrid modes of operation, the injection of power to the grid and the microgrid voltage and frequency regulation. Finally, in this Chapter, a control scheme for an energy storage unit based on supercapacitors was presented, whereby applying an optimal nonlinear control scheme, it is possible to regulate the voltage in a DC bus of a microgrid in the event of an abrupt disconnection of the generation node. Simulation results exhibit the effectiveness of the proposed energy storage system control scheme. It is important to highlight that the design of the energy storage unit presented in this Chapter can be considered as a block or element of a microgrid that can be combined with other microgrid devices such as power electronic converters to provide ancillary services to the electrical power grid.

Chapter 4

Microgrid Power Conditioning Applications

During the grid-connected mode, microgrids can contribute to the overall power-grid control, facilitating the power system operation by providing ancillary services for power-quality enhancement. In this sense, this Chapter presents nonlinear optimal and robust control strategies to provide ancillary services to the electrical power grid in terms of harmonic compensation, voltage regulation, and dynamic power factor correction through power electronics converter nonlinear optimal and robust control in addition with fast and efficient harmonic estimation algorithms. These approaches are first described independently, and then a holistic solution will be presented later to demonstrate that by using a single power electronic converter it is possible to achieve the proposed control objectives jointly.

4.1 The Harmonics Compensation Assessment

This section proposes an online identification and compensation scheme for a distorted waveform's harmonic and interharmonic content in electrical circuits. The proposed novel identification scheme allows the simultaneous estimation of the harmonic components' frequency, amplitude, and phase. One of the main characteristics of the proposed online identification scheme is how the harmonics and interharmonics are estimated using a fast-convergent state estimator based on the state-space representation of the harmonic content. The proposed estimator has a decentralized approach that relies on an efficient implementation, a relevant result for real-time feedback control applications, such as active power filters control. The decentralized structure allows, if needed, the selective harmonic suppression. This section exposes a case study of identifying and suppressing the harmonic and interharmonic content produced by a three-phase load connected to the electrical power grid. To demonstrate the effectiveness of the proposed estimator, hardware-in-the-loop and simulation results validate the identifier effectiveness to determine in real-time the harmonic content and how it can

be used to reduce the total harmonic distortion through a nonlinear optimal tracking control scheme.

4.1.1. The Decentralized Convergent Harmonic Estimator

In order to identify the harmonic components that distort the current waveform in an electrical system, this thesis proposes the design of a fast convergent harmonic estimator with a decentralized structure, which is obtained through the following development. Assume that signal (2.3) can be presented in a state-space representation, and considering the single case, i.e. when $N = 1$ and $a_0 = 0$, then by employing the trigonometric identity $\sin(a + b) = \sin(a)\cos(b) + \sin(b)\cos(a)$ to (2.3), one obtains

$$s = A\cos(\theta)\sin(\alpha\, t) + A\sin(\theta)\cos(\alpha\, t). \tag{4.1}$$

Then, consider the signal (4.1) rewritten as

$$s = A\cos\theta\bar{\omega}_1 + A\sin\theta\bar{\omega}_2 \tag{4.2}$$

where $\bar{\omega}_1 = \sin\alpha t$ and $\bar{\omega}_2 = \cos\alpha t$. Then by taking the corresponding time derivative, it is possible to state that $\dot{\bar{\omega}}_1 = \alpha\bar{\omega}_2$ and $\dot{\bar{\omega}}_2 = -\alpha\bar{\omega}_1$. By proposing the change of variables $\omega_1 = \frac{\bar{\omega}_1}{\alpha}$ and $\omega_2 = \bar{\omega}_2$, the dynamics of (4.2) becomes

$$\begin{aligned} \dot{\omega}_1 &= \omega_2 \\ \dot{\omega}_2 &= -\alpha^2\omega_2 \\ s &= A\alpha\cos\theta\omega_1 + A\sin\theta\omega_2. \end{aligned} \tag{4.3}$$

Introducing a parameter λ to scale the magnitude of the signal, and defining $z_1 = \lambda\omega_1$ and $z_2 = \omega_2$, one obtains

$$\begin{aligned} \dot{z}_1 &= \lambda z_2 \\ \dot{z}_2 &= -\frac{\alpha^2}{\lambda} z_1 \\ \dot{z}_3 &= 0 \end{aligned} \tag{4.4}$$

where the new variable z_3 is included to model the angular frequency, which is considered to be constant, with initial condition $z_3(0) = \alpha^2$. Finally, signal (4.2) can be obtained from (4.4) through the output

$$s = \frac{k_1}{\lambda} z_1 + k_2 z_2 \tag{4.5}$$

with $k_1 = A\alpha\cos\theta$ and $k_2 = A\sin\theta$, where z_1, z_2 and z_3 are the state variables, and parameters $k_1, k_2 \neq 0$, and $\lambda \neq 0$ are used to scale the signal magnitude. In the case

of that signal s includes a DC component[1], as described in (2.1) through $a_0/2$, the following differential equation can be added to (4.4) as $\dot{z}_0 = 0$ with the initialization $z_0(0) = a_0/2$. Notice that the frequency α is included as a state variable by means of $\dot{z}_3 = 0$, which means that the rate of change of frequency (ROCOF) is assumed to be constant, but of unknown value. Therefore, it is of interest the state estimation of z_1, z_2 and the angular frequency z_3, by means of $\hat{z}_1$, $\hat{z}_2$ and $\hat{z}_3$, respectively. By considering the structure of (4.4) and defining $\hat{z} = \begin{bmatrix} \hat{z}_1 & \hat{z}_2 & \hat{z}_3 \end{bmatrix}^T$, the state estimator can be stated as:

$$\begin{aligned} \dot{\hat{z}}_1 &= \lambda \hat{z}_2 + \frac{\lambda}{k_2}(s - \hat{s}) \\ \dot{\hat{z}}_2 &= -\frac{\hat{z}_1\, \hat{z}_3}{\lambda} + \xi(s - \hat{s}) \\ \dot{\hat{z}}_3 &= -\gamma \hat{z}_1 (s - \hat{s}) \\ \hat{s} &= \frac{k_1}{\lambda}\hat{z}_1 + k_2 \hat{z}_2 \end{aligned} \tag{4.6}$$

where $\lambda, \xi, \gamma > 0$ and k_1 and $k_2 \neq 0$ are parameters to be determined to ensure that the error convergence is $\lim_{t\to\infty} e = 0$, with $e = s - \hat{s}$. The estimator (4.6) considers the frequency estimation as described in [Obregon-Pulido et al., 2002], in addition, the proposed estimator considers the frequency determination in a decentralized way as well as the amplitude and phase for each harmonic component. For such purpose, consider that signal (4.1) can be obtained from the output of (4.4), then the following relationship is fulfilled

$$A\cos(\theta)\sin(\alpha\, t) + A\sin(\theta)\cos(\alpha\, t) = \frac{k_1}{\lambda} z_1 + k_2 z_2 \tag{4.7}$$

which by taking its term-by-term time derivative, it follows that

$$A\,\alpha\cos(\theta)\cos(\alpha\, t) - A\,\alpha\sin(\theta)\sin(\alpha t) = \frac{k_1}{\lambda}\dot{z}_1 + k_2 \dot{z}_2 = k_1 z_2 - k_2 \frac{\alpha^2}{\lambda} z_1. \tag{4.8}$$

Representing the left-hand side of (4.7) and (4.8) by their respective trigonometric identities, i.e. $A\sin(\alpha\, t + \theta)$ and $A\,\alpha\,\cos(\alpha\, t + \theta)$, respectively, and defining

$$\begin{aligned} b_1 &= \frac{k_1}{\lambda} z_1 + k_2 z_2, \\ b_2 &= k_1 z_2 - k_2 \frac{\alpha^2}{\lambda} z_1 \end{aligned} \tag{4.9}$$

then it is possible to state (4.7)–(4.8) by the following equations system

$$\begin{aligned} A\sin(\alpha\, t + \theta) &= b_1 \\ A\alpha\cos(\alpha\, t + \theta) &= b_2. \end{aligned} \tag{4.10}$$

[1] *This thesis considers AC applications with sinusoidal electrical waveforms without DC components. So, it is assume that the value of a_0 is zero.*

By solving (4.10), the amplitude A and phase angle θ of the harmonic content is determined, respectively, as

$$A = \frac{\sqrt{\alpha^2 b_1^2 + b_2^2}}{\alpha} \tag{4.11}$$

and

$$\theta = \arctan\left(\frac{\alpha\, b_1 - b_2 \tan(\alpha\, t)}{b_2 + \alpha\, b_1 \tan(\alpha\, t)}\right). \tag{4.12}$$

Notice that A and θ depend on the variables z_1 and z_2 to be estimated through $\hat{z}_1$ and $\hat{z}_2$, respectively, meanwhile α is determined from $\hat{z}_3$. Additionally, notice that no singularity issue is presented in (4.11)[2]. The time requirement in (4.11) and (4.12) is obtained from a phase-locked loop (PLL) mechanism, wherein the literature different efficient and fast PLL have been reported, as seen in [Ghartemani, 2014], even specialized electrical simulation tools include PLL as part of their simulation libraries (e.g., MATLAB/Simulink, PSCAD)®.

4.1.2. The n-Frequencies Case

One of the main novelties of this thesis is the proposal of a decentralized fast-convergent estimator (which requires less than a cycle of the fundamental harmonic to perform the estimation of an electrical waveform) for a signal composed of n harmonics, where the frequencies, amplitudes, and phases are unknown. The decentralized approach reduces the number of the estimator parameters to be tuned and the computational burden required for the harmonic computation, allowing a more straightforward implementation. This contribution is presented in the following Theorem.

Theorem 2. *Assume that signal* (2.1) *can be rewritten in terms of n individual harmonics/interharmonics as*

$$\hat{s} = \sum_{n=1}^{N} \hat{s}_n \tag{4.13}$$

where each harmonic is estimated using

$$\begin{aligned}
\dot{\hat{z}}_{n1} &= \lambda_n \hat{z}_{n2} + \frac{\lambda_n}{k_{n2}}(s - \hat{s}) \\
\dot{\hat{z}}_{n2} &= -\frac{\hat{z}_{n3}}{\lambda_n}\, \hat{z}_{n1} + \xi(s - \hat{s}) \\
\dot{\hat{z}}_{n3} &= -\gamma_n \hat{z}_{n1}(s - \hat{s}) \\
\hat{s}_n &= \frac{k_{n1}}{\lambda_n} \hat{z}_{n1} + k_{n2} \hat{z}_{n2}.
\end{aligned} \tag{4.14}$$

[2] *Considering that α is always different to zero (in the case of that signal s includes a DC component, it is possible to follow the procedure as described in subsection 4.1.1) then, it is possible to affirm that there is not a singularity issue in the estimation of the amplitudes of the harmonics.*

Then $\hat{s}$ asymptotically converges toward s. Hence, the parameters frequency, amplitude and phase for each harmonic/interharmonic can be determined from $\hat{z}_3$ in (4.6)*,* (4.11) *and* (4.12)*, respectively.*

Proof. See Appendix B. □

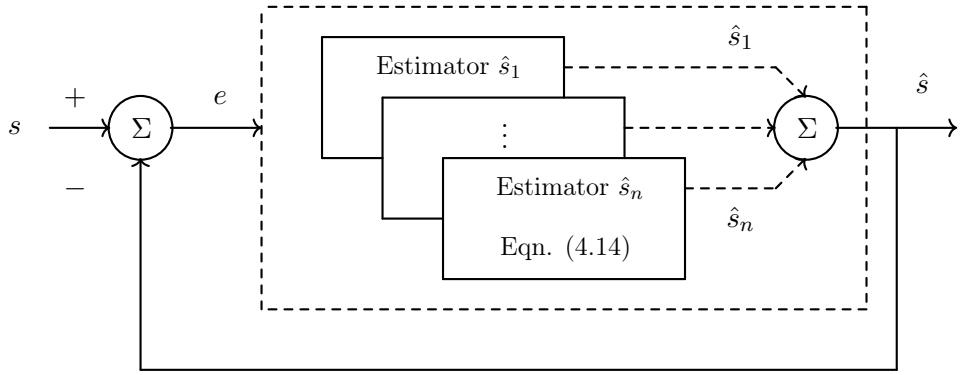

Figure 4.1: Decentralized harmonic estimator structure.

Figure 4.1 shows a graphic representation of how the decentralized estimator is implemented through a parallel configuration of n estimators for n harmonics. Notice that the estimator order should be selected according to a required application and the possible harmonics that may be contained in the signals and the available hardware to achieve a real-time implementation.

4.1.3. Typical Applications for the Proposed Harmonic Estimator

Shunt Power Conditioner

Figure 4.2 shows a typical application of the proposed harmonic estimator to suppress the harmonic content in a distorted waveform in a power system, through the nonlinear optimal control of a power conditioner device such as an active power filter. It is important to mention that the proposed shunt power conditioner can provide a wide range of ancillary services to a power system node, such as harmonic and reactive power compensation while taking advantage of the existing infrastructure of typical industrial applications such as the distributed generation systems.

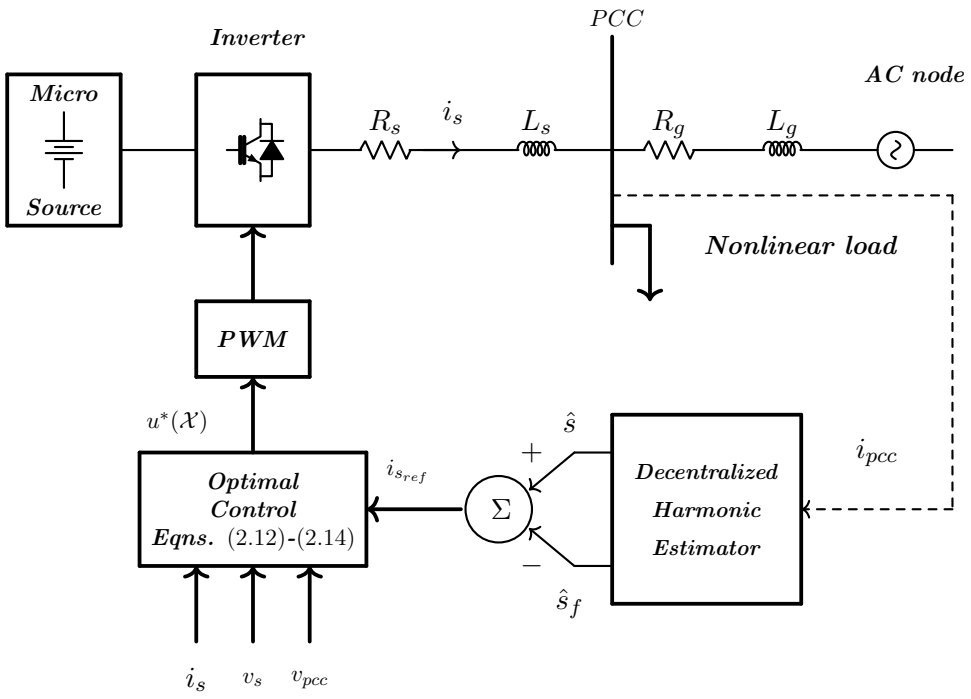

Figure 4.2: Harmonics compensation scheme.

Electric Motor Drives

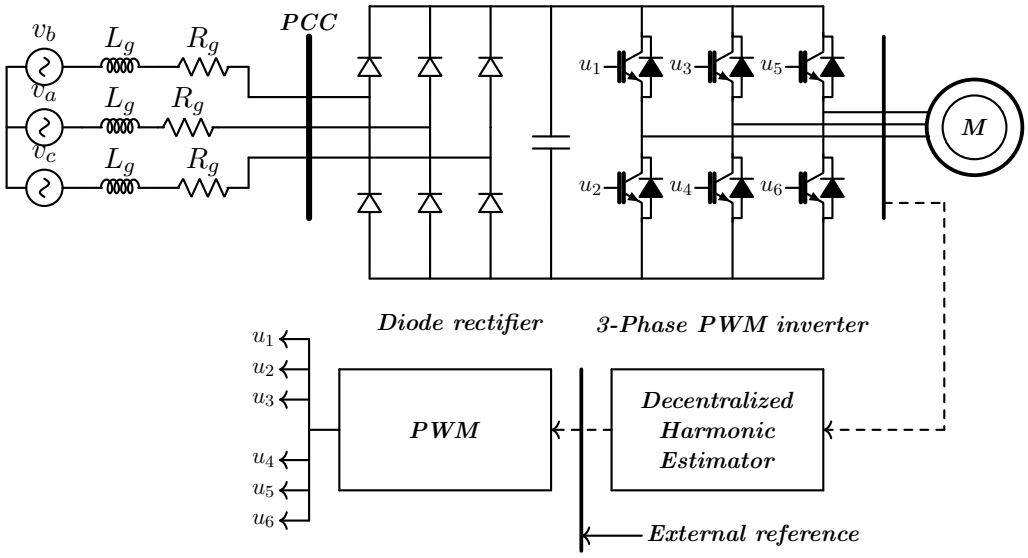

Figure 4.3: Reduction of harmonics in induction motor drives.

The proposed harmonic estimation strategy (4.14) can be used to control electric motor drives to suppress the harmonic distortion produced by large induction motors operation in a power system. In this way the estimated signals directly can be taken as reference signals for a modulation strategy (PWM) as shown in Figure 4.3 without using an extra control method.

4.1.4. A Case of Study: Three-Phase Harmonics Identification and Compensation through the Optimal Control of a Power Electronic Converter

The great flexibility offered by power electronics devices allows that through appropriate control strategies, different functionalities can be obtained. In this section, the proposed harmonic estimation strategy will be used, in combination with the nonlinear optimal control scheme, to achieve the trajectory tracking control of the output of an active power filter (APF), to significantly compensate the harmonic distortion of the current waveform demanded by a nonlinear load in a three-phase circuit.

System Description

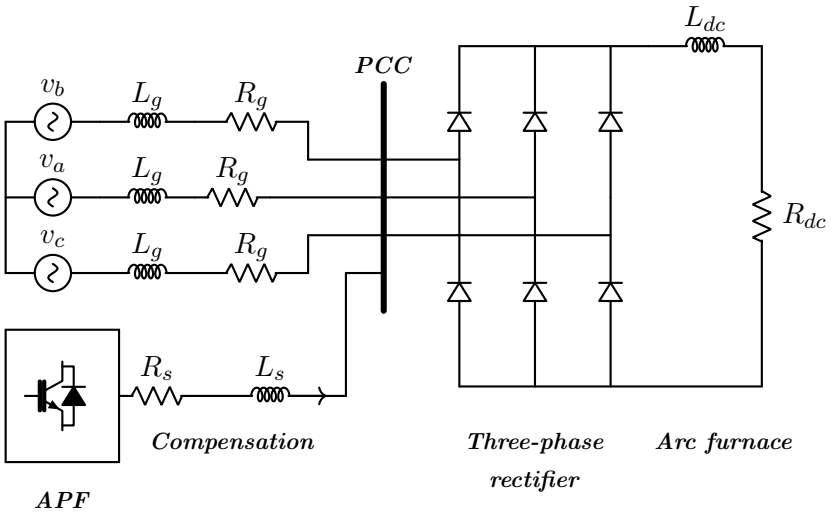

Figure 4.4: Proposed nonlinear load producing harmonic distortion.

To demonstrate the effectiveness of the proposed online harmonic estimator, consider a power system configuration, as depicted in Figure 4.5 and the nonlinear load as described in Figure 4.4. To suppress the harmonic distortion of the current waveform produced by the nonlinear load, a set of three individual APF are connected, each one to every single phase of the circuit at the point of common coupling, through an RL filter. A configuration based on three single-phase power electronic inverters instead of having an individual three-phase converter is for carrying out independent compensations at each phase. This thesis considers the general case of using a DC source V_{cc} for the APF (which for simulation purposes is considered as a constant DC source due to the time window in which the analysis is conducted considering slow variations of the distributed generation unit). However, for practical implementations, the DC-side energy could be obtained from a unitary power factor controlled rectifier or distributed renewable-based generation sources (e.g., PV, wind, batteries, among others) as seen in [Ornelas-Tellez et al., 2018] (or by considering energy storage devices as

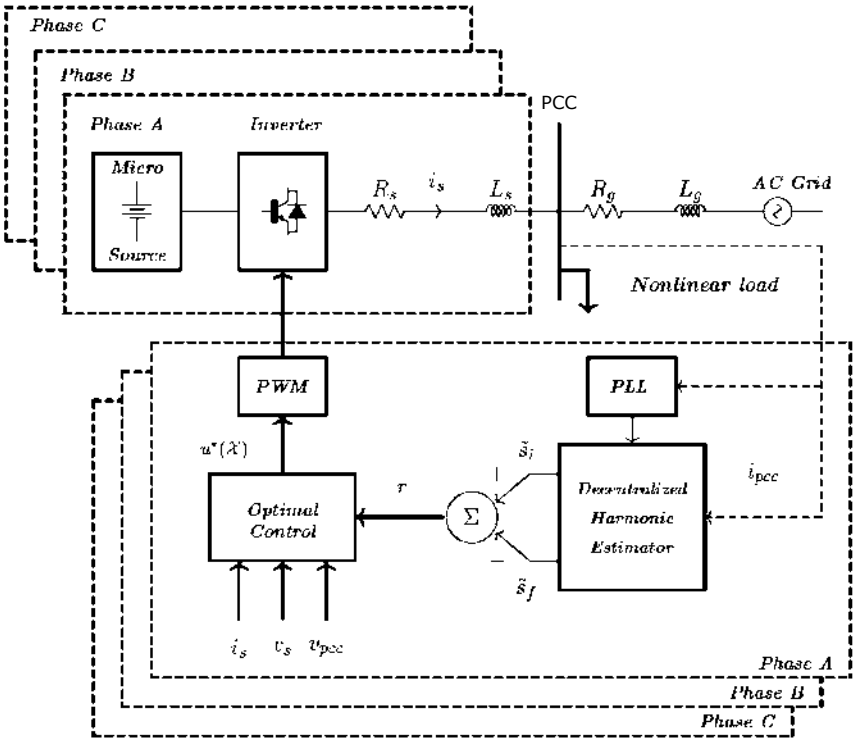

Figure 4.5: Proposed system configuration.

described in Chapter 3), where the associated dynamics should be taken into account in the control system to avoid possible DC-side voltage oscillations, which is an interesting topic for future research. For simulation purposes, load harmonic current injections at each circuit phase are considered. The load profile represents the harmonic current source drawn from a diode/thyristor rectifier feeding inductive loads. In this thesis, the considered load is depicted in Figure 4.4, which corresponds to an electric arc furnace, as reported in [Akagi, 2007]. Still, the analysis is equally valid for other applications such as DC motors or, ultimately, the variable speed drive of widespread use in the control of induction motors. Furthermore, to demonstrate the capabilities of the estimator to identify harmonics with non-multiple integer frequencies of the fundamental, an inter-harmonic and a sub-harmonic terms generated by a current source have been added to the current profile, which is approximated by the following signal, as

$$\begin{aligned} s =& A_i \sin(\alpha_l t + \theta_l) + A_h \sin(\alpha_h t + \theta_h) \\ &+ A_f \sin(\alpha_f t + \theta_f) + A_3 \sin(\alpha_3 t + \theta_3) \\ &+ A_5 \sin(\alpha_5 t + \theta_5) + A_7 \sin(\alpha_7 t + \theta_7) \end{aligned} \tag{4.15}$$

where $\alpha_n = 2\pi n f$ are the angular frequency rad/s for the n-th harmonic, being α_3, α_5, α_7 and α_f the odd and fundamental frequencies respectively, with α_i a low order interharmonic frequency (sub-harmonic) and α_h a high order interharmonic, both non-integer multiples w.r.t. the fundamental, which in this application is taken as

$f = 60Hz$, A_n are the amplitudes of the harmonics and θ_n the angle phases.

Remark 1: It is worth mentioning that signal (4.15) is composed of harmonic and interharmonic terms, whereby the use of the proposed online estimator is possible to estimate the frequency, amplitude, and phase for each harmonic component of a measured signal.

4.1.5. HIL Results

This section presents the results of a HIL-type[3] simulation for the harmonic estimator through its implementation in a low-cost microcontroller. The experimental results demonstrate the effectiveness of implementing the estimator for real-time applications.

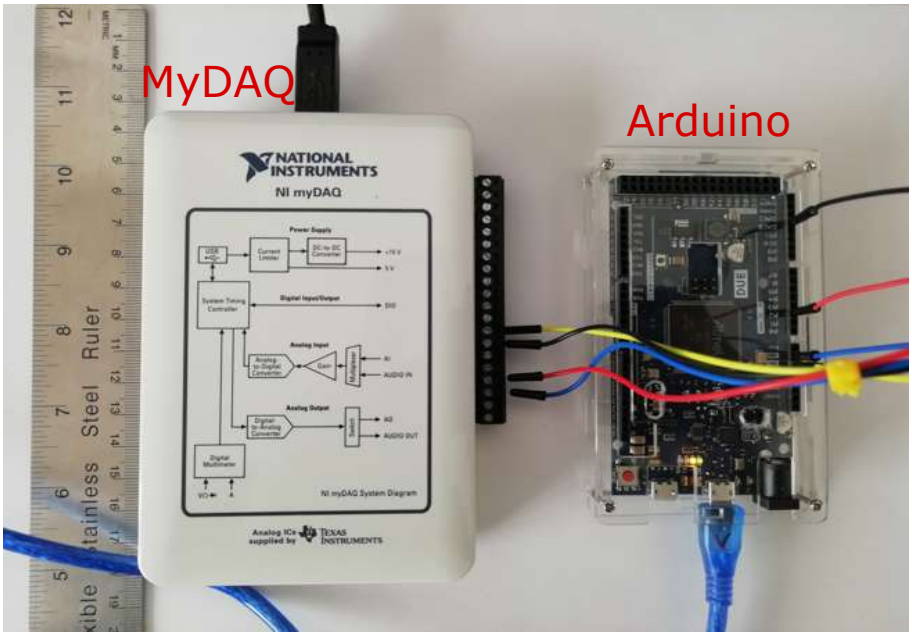

Figure 4.6: Hardware in the Loop system implementation.

As a complement of the main contribution of this thesis, to evaluate the effectiveness of the harmonic estimation (4.13), a HIL simulation was implemented considering the hardware setup as described in Figure 4.6, as follows: the current signals in the electrical grid, as depicted in Figure 4.5, are emulated by using a National Instruments MyDaq® and the LabView® environment; then, the generated signals were sent and measured in an Arduino® Due microcontroller (ATSAM3X8E-ARM Cortex-M3 @ 84 MHz), which performs the harmonic estimation by using the required programming in the Matlab/Simulink® interface. Where the estimator parameters for each phase

[3] *Hardware-in-the-loop HIL simulation, or HWIL, is a technique that is used in the development and test of complex real-time embedded systems. HIL simulation provides an effective platform by adding the complexity of the plant under control to the test platform. The complexity of the plant under control is included in test and development by adding a mathematical representation of all related dynamic systems.*

are given in Table I-III (see Appendix C). In addition, it is important to mention that the parameters (estimator gains) must be selected to fulfill the stability and its convergence rate of the estimator (see the stability analysis in Appendix B). Furthermore, if it is required, optimization techniques based on artificial intelligence, such as particle swarm optimization (PSO) [Jamshidi, 2014], could be applied to compute the optimal parameters of the estimator. However, it would require a more considerable computational effort for real-time implementations. The HIL results are given as follows.

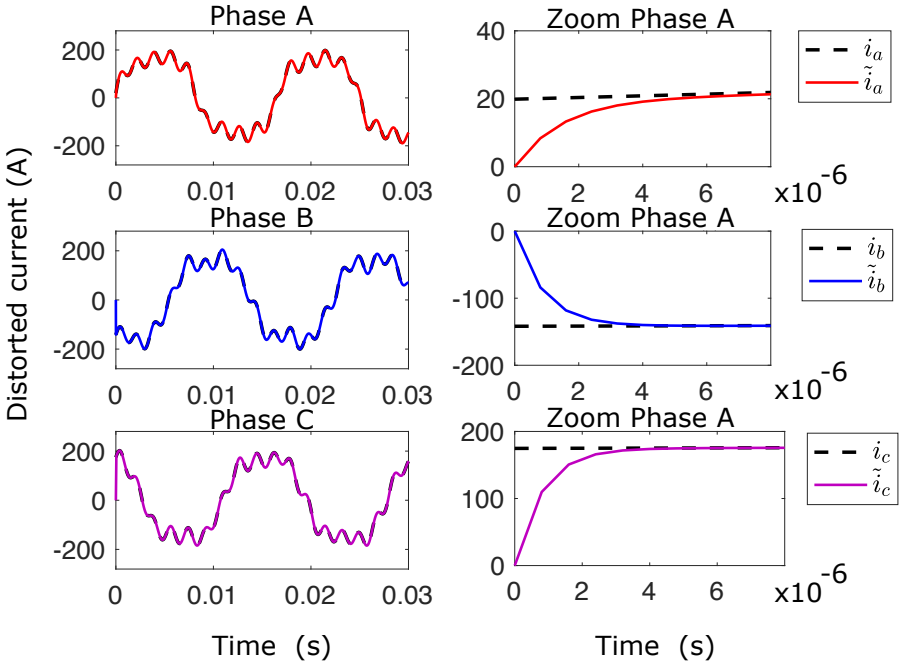

Figure 4.7: Distorted current estimation for each phase.

The results given in Figure 4.7 depict the time response evolution of the estimated current $\tilde{i}(t)$ to reach the measured current $i(t)$ for each phase of the three phase system. On the right-hand side of Figure 4.7, a zoom area presents the fast estimator convergence, where the convergence rate of the estimator can be seen in a time period of less than $5\mu s$, which is a desirable characteristic for feedback control applications. The speed convergence rate of the estimator is an important parameter because the estimator must be faster than the control algorithm to suppress the harmonic content of a distorted waveform successfully. Additionally, it is important to notice that the time response of the estimator is a characteristic that can be used for various applications such as power quality measurement instruments or the control of electric motor drives through PWM modulation strategies, which are applications that require fast estimation responses.

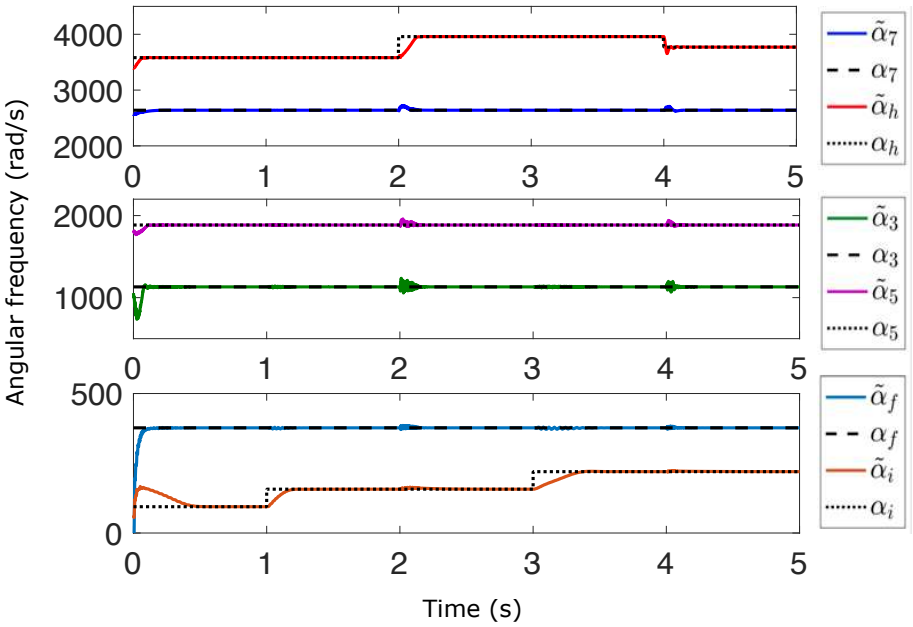

Figure 4.8: Estimated harmonic frequencies using HIL.

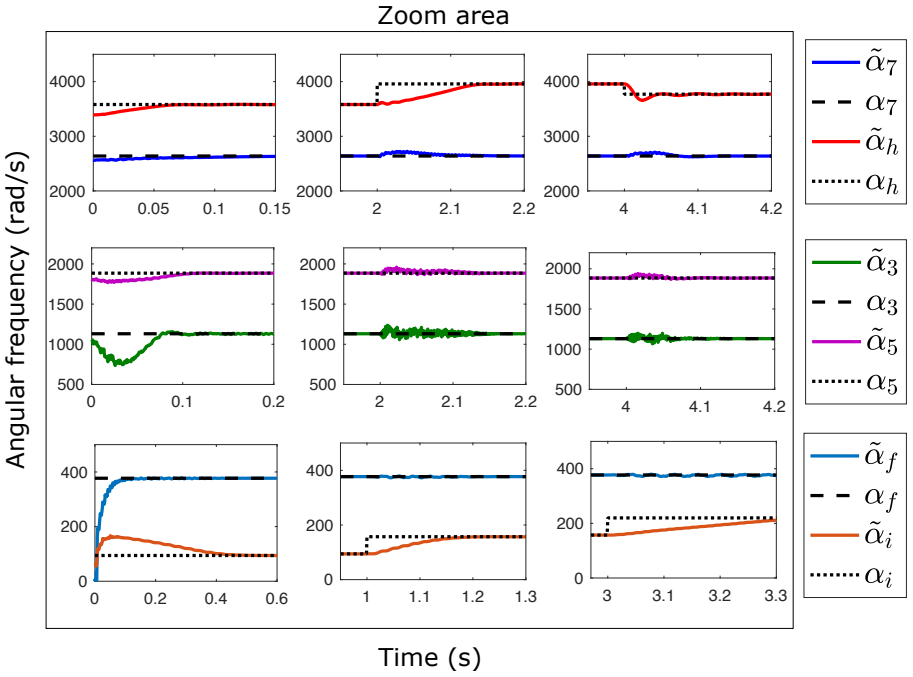

Figure 4.9: Estimated harmonic frequencies using HIL zoom area.

Figure 4.8 depicts one of the outstanding characteristics of the proposed harmonics estimator, which is the frequency estimation. Additional to the determination of the unknown harmonic frequencies, the interharmonic frequencies α_h and α_i are abruptly changed as

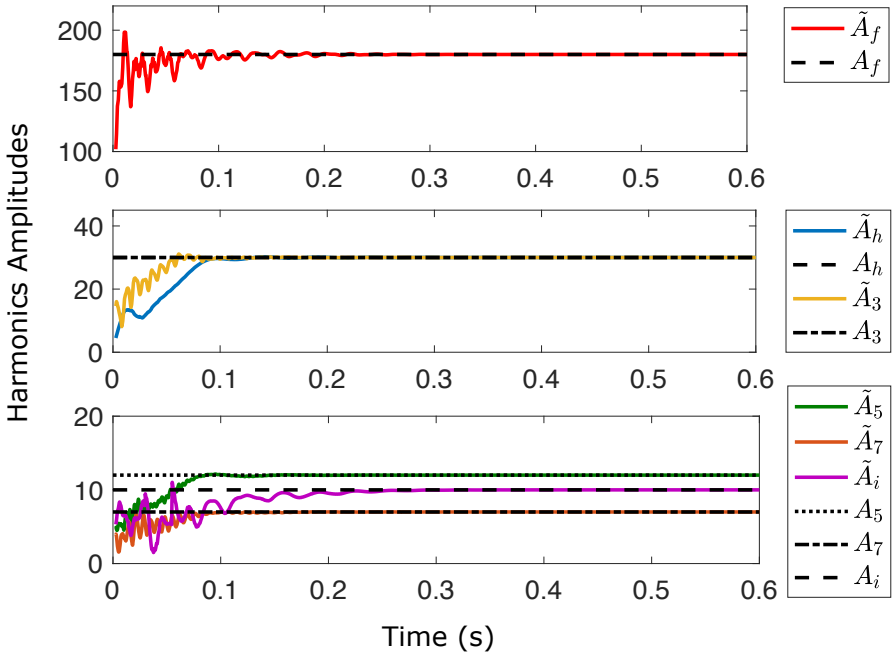

Figure 4.10: Estimated harmonics amplitudes using HIL.

$$\alpha_i = \begin{cases} 15 \times 2 \times \pi \, rad/s & t \leq 1s \\ 25 \times 2 \times \pi \, rad/s & 1s < t \leq 3s \\ 35 \times 2 \times \pi \, rad/s & t > 3s \end{cases} \tag{4.16}$$

$$\alpha_h = \begin{cases} 9.5 \times 2 \times \pi \times 60 \, rad/s & t \leq 2s \\ 10.5 \times 2 \times \pi \times 60 \, rad/s & 2s < t \leq 4s \\ 10 \times 2 \times \pi \times 60 \, rad/s & t > 4s \end{cases} \tag{4.17}$$

where $\alpha_f = 2 \times \pi \times 60$, $\alpha_3 = 6 \times \pi \times 60$, $\alpha_5 = 10 \times \pi \times 60$ and $\alpha_7 = 14 \times \pi \times 60$, all in rad/s, are kept constants. Notice that the frequency estimation exhibits a fast convergence rate as seen in the zoom area on the dynamic behavior during transients around $t = 0$, $t = 2$ and $t = 4$ shown in Figure 4.9.

Additionally, Figure 4.10 depicts the amplitudes of the estimated harmonics, where from (4.11), it is possible to appreciate the convergence of $\tilde{A}_n$ towards A_n, where $A_i = 10$, $A_h = 30$, $A_f = 180$, $A_3 = 30$, $A_5 = 12$ and $A_7 = 7$, respectively. It is important to mention that the results given in Figure 4.10 are experimental, using an Arduino® microcontroller, with limited features and possible numerical problems such as analog-digital conversion resolution. However, if a more sophisticated device or simulation level is used, a better performance could be obtained. In addition, for practical applications, the speed of convergence does not matter if the device ratings are not respected. Therefore, depending on the application requirements, it is possible to adjust the parameters of the estimator to achieve the desired behavior, reducing the

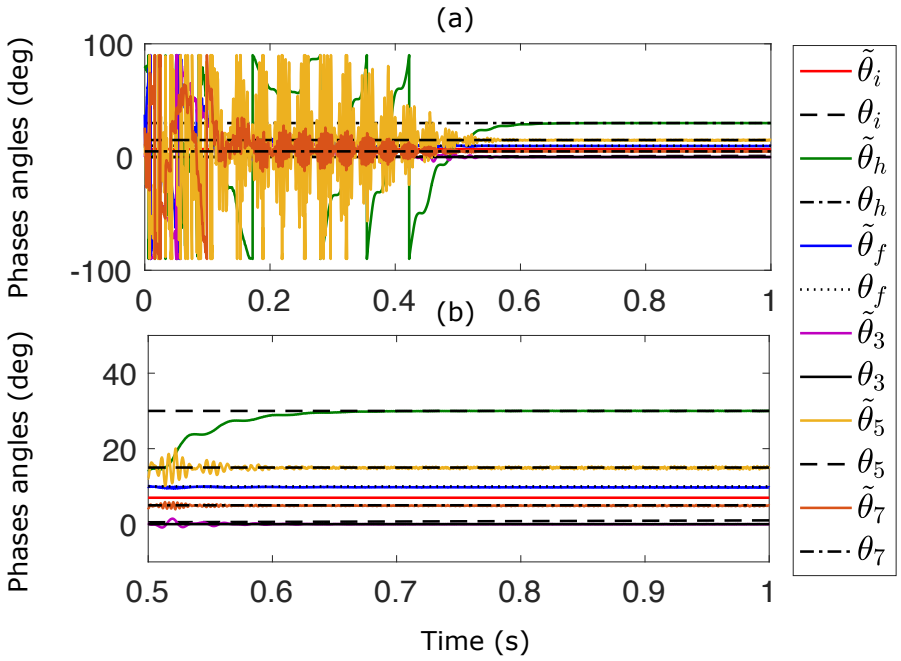

Figure 4.11: Phase angles estimation using HIL.

transient effects which in practical applications would shunt down the entire system by the activation of protection devices. In this sense, it is worth mentioning that it is possible to reduce the transient oscillations of the harmonic estimator by appropriately initializing the algorithm (by given initial conditions other than zero, close to the expected value), or alternatively, to use the estimation of the harmonics once the transient response has occurred.

An interesting result is shown in Figure 4.11, which depicts the estimation of the phase angles θ_n, where it is possible to appreciate the respective convergence of $\tilde{\theta}_n$ toward θ_n, where $\theta_i = 30$, $\theta_h = 10$, $\theta_f = 0$, $\theta_3 = 15$, $\theta_5 = 5$ and $\theta_7 = 7$, all in deg units. In addition, Figure 4.11(b) shows a zoom of the phases convergence. It is important to mention that the sampling rate for the Arduino® Due was established at 1M samples per second. Notice that during the estimation of the phase angles, a transient is presented, this is due to the way the in which the phase angles are calculated as described in (4.12) where an arctangent function is required. Nonetheless, this is a fast transient and can be modified from a proper tuning of the parameters of the estimate. However, the speed of convergence of the estimator may be affected. Depending on the desired application, in order to avoid the transient effect in the phase estimation, it is possible to wait for the estimator to converge and then, use the information given by the estimator for another application such as feedback control systems.

4.1.6. Simulation Results

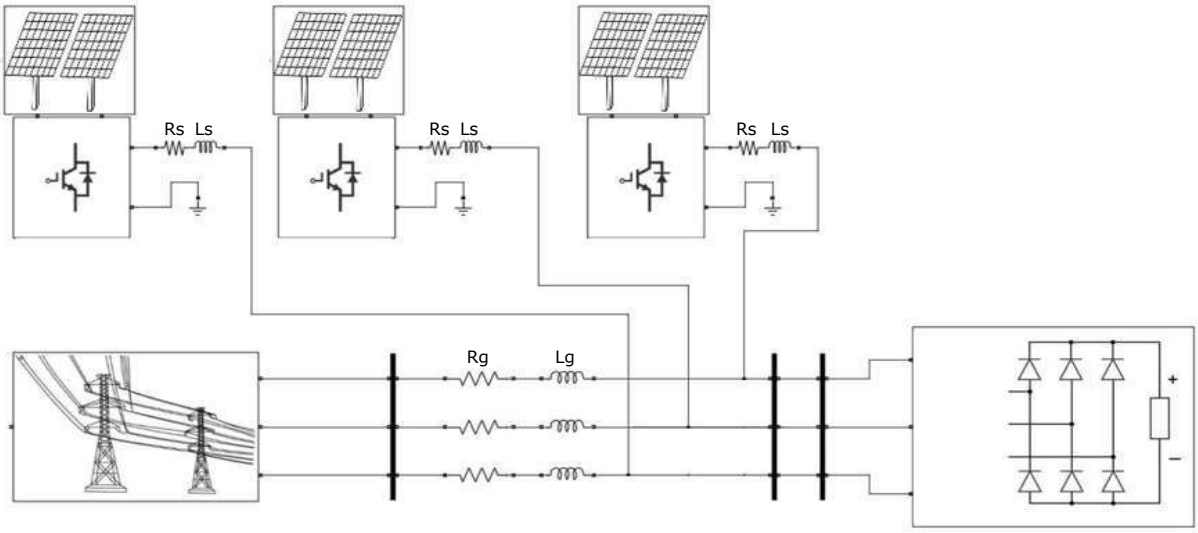

Figure 4.12: Microgrid harmonics compensation scheme through ancillary services.

In addition to the HIL results presented in the previous section, a complete simulation (including APF control for the harmonics suppression) with the system configuration shown in Figure 4.5 is carried out with MATLAB/Simulink®. Consider the system configuration shown in Figure 4.12, with the following results. For simulation purposes, the matrices of the cost functional (2.10) are chosen as $Q = 100$ and $R = 4$, where matrix Q weights the tracking error $\varepsilon = r - y$, while matrix R weights the control effort. The parameters of the APF are $L_s = 5.1mH$, $R_s = 0.2\Omega$, $V_{cc} = 500V$ and $V_s = 120V_{rms}$. The time-varying reference r to be tracked by the APF output is obtained from the harmonic estimator (4.6) as follows.

$$r = \sum_{i=1}^{m} \hat{s}_i - \hat{s}_f \tag{4.18}$$

where $\hat{s}_i$ are the estimated harmonics/interharmonics at the i-th frequency and $\hat{s}_f$ is the estimated fundamental harmonic component, i.e., the APF will suppress the undesired harmonics different to the fundamental, thus improving the power quality of the utility grid. Notice that the proposed optimal controller requires the complete model of the system. Nonetheless, if a more robust control design is required, it is possible to improve the nonlinear optimal tracking controller in order to reject parametric uncertainties and disturbances by adding an integral control action to the controller (as described in Chapter 2) or combining it with sliding mode control, as seen in [Ramos-Paz et al., 2019], or a different robust control technique could be used in combination with the harmonic estimator.

Remark 2: Notice that by means of the reference signal (4.18), if it is needed, it could accordingly suppress a selective i-th harmonic component due to the decentralized structure of the harmonic estimator.

Associated to the optimal tracking control, Figure 4.13 depicts the harmonic compensation in the power system through the APF output current control. The top of Figure 4.13(a) shows the distorted current waveform, and how by means of the harmonic estimation and suppression scheme, it is possible to suppress the undesired harmonic components of the electrical waveforms in a three phase system. Figure 4.13(b) shows the required injected currents to perform the harmonics suppression at each phase of the circuit. Notice that the signals are provided by the harmonic estimator and used as reference signals (i_{ref}). It is worth mentioning that the nonlinear optimal tracking controller provides a fast response to achieve the corresponding tracking of the time varying reference signals i_f for each phase as illustrated in the Figure 4.13.

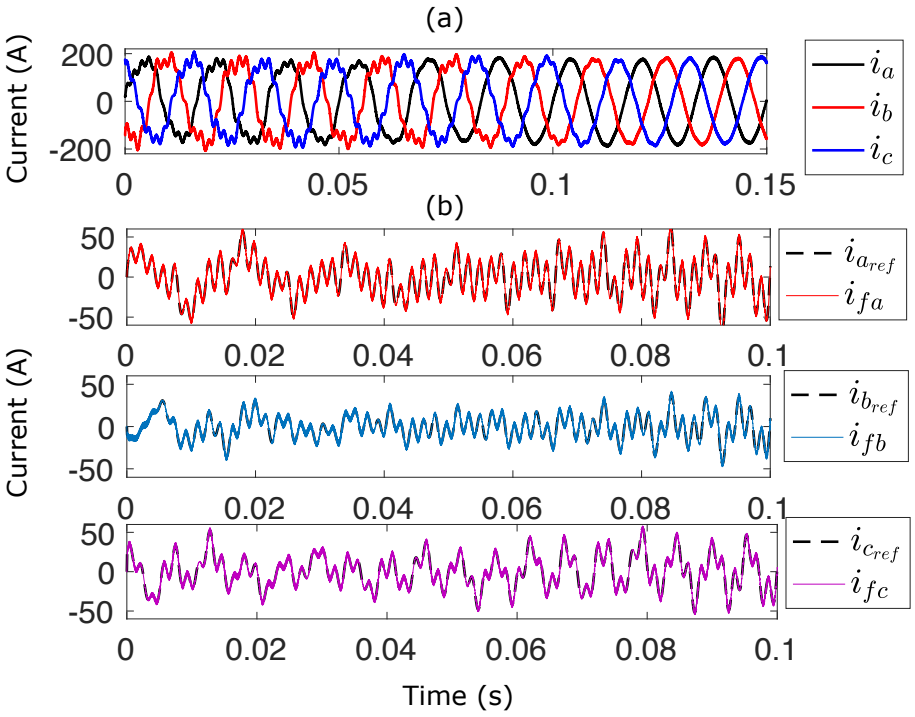

Figure 4.13: (a) Harmonic compensation over the three-phase current load. (b) Optimal tracking control of the estimated harmonic reference signals for the APFs.

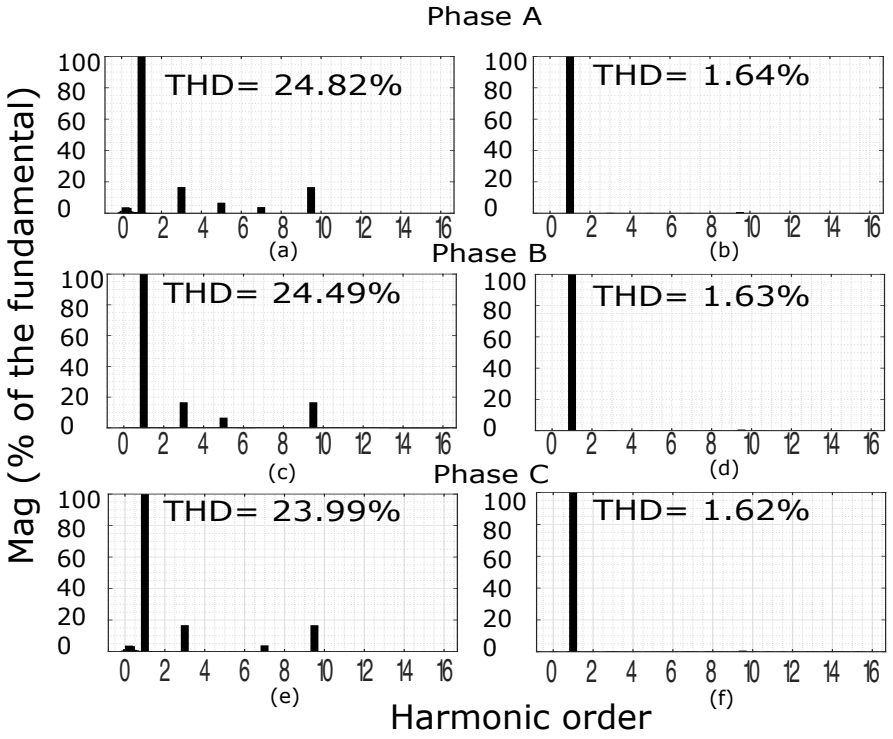

Figure 4.14: Total harmonic distortion before and after the dynamic compensation at each phase.

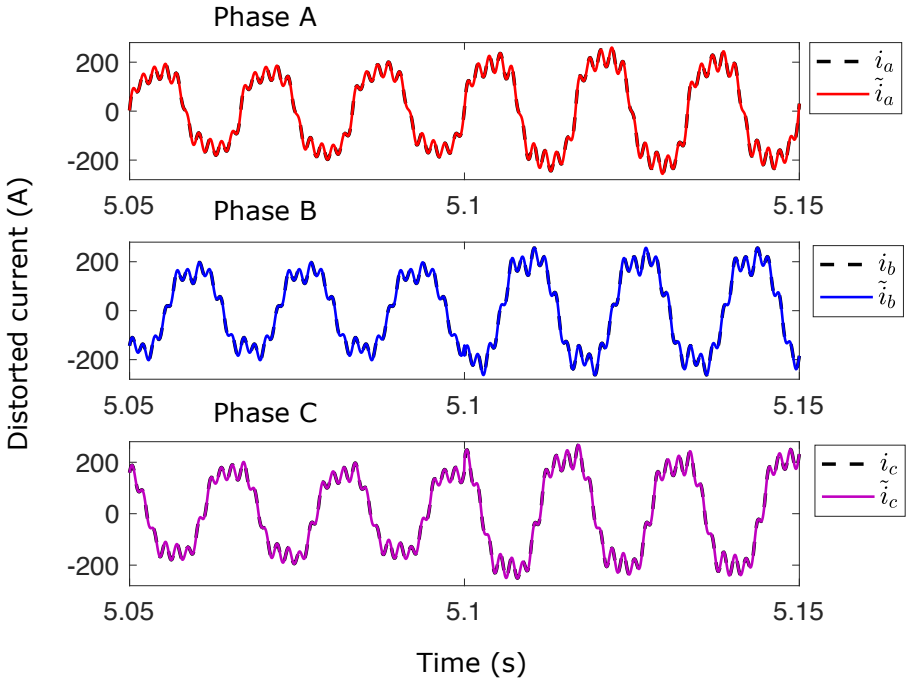

Figure 4.15: Distorted current estimation under abrupt load change.

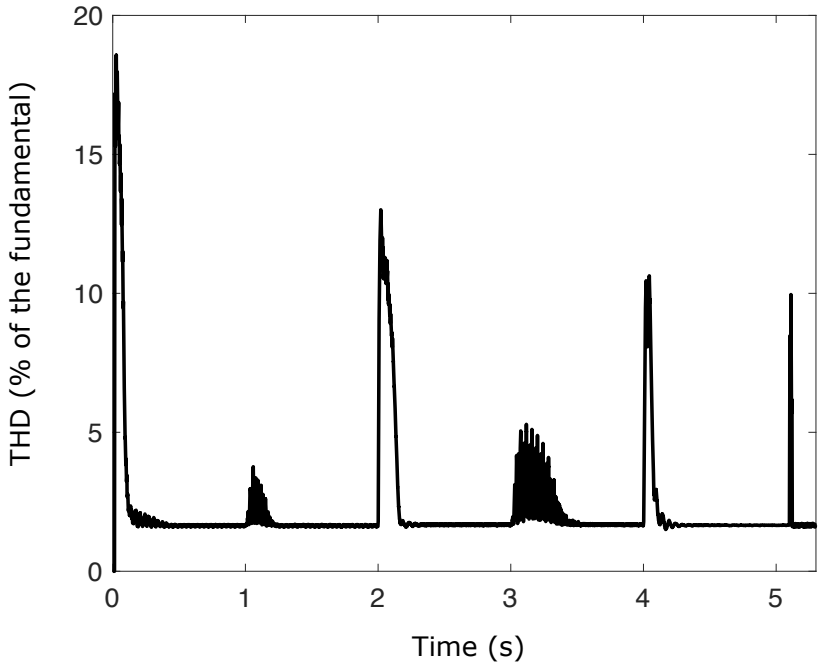

Figure 4.16: Total harmonic distortion during frequency and load changes.

The results given in Figures. 4.14(a),(c) and (e), show the THD per phase before the compensation, and in Figure 4.14(b),(d) and (f) is shown the THD after the usage of the proposed harmonic identification and compensation strategy. In addition, a significant decrease in the THD of the current waveforms can be seen, allowing compliance with standards in terms of harmonic distortion.

Figure 4.15 depicts the time response evolution of the estimated current $\tilde{i}(t)$ to reach the measured current $i(t)$ for each phase, which contains different harmonic content; as it may be observed, the estimator exhibits fast convergence properties and fast response during load steps changes, considering an abrupt load change of 30% at $t = 5.1s$.

Figure 4.16 shows the THD measured during frequency and load changes considering a sampling rate of 0.5μs based on a sampling moving window; the THD computation depicts how the harmonic estimation and suppression scheme can considerably reduce total harmonic distortion in the presence of abrupt frequency and load changes reducing the harmonic distortion at the time $t = 1, 2, 3, 4$s and $t = 5$s respectively. In the simulation results, transients can be observed. However, this may be due to the Gibbs phenomenon[4].

[4]The Gibbs phenomenon, discovered by Henry Wilbraham (1848) and rediscovered by J. Willard Gibbs (1899), is the peculiar manner in which the Fourier series of a piecewise continuously differentiable periodic function behaves at a jump discontinuity. The n th partial sum of the Fourier series has large oscillations near the jump, which might increase the maximum of the partial sum above that of the function itself. The overshoot does not die out as n increases, but approaches a finite limit.

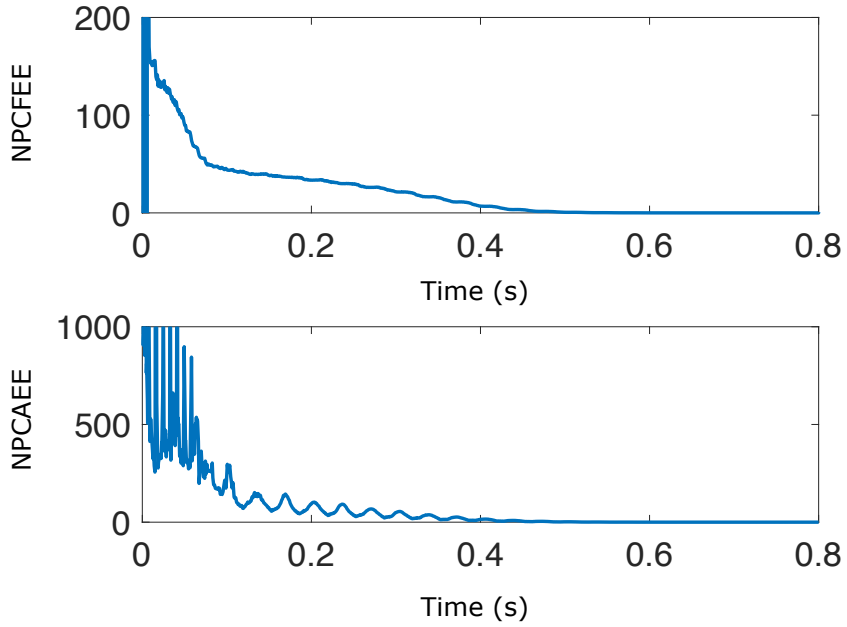

Figure 4.17: Performance indices of the proposed harmonic estimator.

In order to include performance indexes for the estimator to be compared with existing estimation methods, two indices of performance are defined in terms of the normalized percentage cumulative amplitude estimator error (NPCAEE) and the normalized percentage cumulative frequency estimation error (NPCAEE) are included as seen in [Mojiri et al., 2010] defined as follows.

$$\text{NPCAEE} = \sum_{n=1}^{N} \frac{|A_n - \tilde{A}_n|}{A_n} \times 100 \tag{4.19}$$

$$\text{NPCFEE} = \sum_{n=1}^{N} \frac{|\alpha_n - \tilde{\alpha}_n|}{\alpha_n} \times 100 \tag{4.20}$$

Figure 4.17 depicts the cumulative error of the estimation of the harmonics amplitudes and frequencies and how the error decay to zero in less than $0.5s$. Furthermore, despite a higher transient, the harmonic estimator proposed in this thesis exhibits a faster amplitude estimation than the results shown in [Mojiri et al., 2010].

4.2 The Power Factor Compensation Assessment

This section describes a novel control strategy applicable to power electronic converters intending to provide ancillary services to the electrical power grid in terms of power factor compensation. This objective is achieved through a nonlinear control strategy centered on nested control loops based on super-twisting sliding modes and nonlinear optimal tracking control. To make the power converter output track a desired reference

current to inject the required reactive power for the power factor compensation at a power system node. Simulation results demonstrate the effectiveness of the proposed control scheme by guaranteeing unitary power factor regulation in the face of abrupt load variations.

Traditionally, the power factor compensation is carried out through the parallel connection of capacitors banks to compensate the reactive power consumed by a load in the electrical power grid, commonly by inductive loads. These capacitors are sized according to the installed load, doing this configuration static. Nonetheless, if the load varies, two scenarios could happen; on the one hand, the installed capacitors would be insufficient to compensate the desired power factor required by the electrical power grid operators in compliance with the grid codes. On the other hand, the capacitors would be oversized if the load decreases, generating a leading power factor. In addition, in the presence of harmonic distortion, if the combination of the line reactance and the required capacitor for power factor correction has a resonance as the harmonic current generated by a nonlinear load, an overcurrent may flow through the capacitor, causing potential damage to the power system. In this sense, a dynamic power factor compensation scheme is proposed in this thesis through the robust nonlinear control of power electronic converters acting as ancillary services to the electrical power grid. This application can improve the power quality and thus, enable users mainly of industrial-type to avoid the fines imposed by the electrical power grid operators concerning the operation with an inappropriate power factor.

4.2.1. Proposed Dynamic Power Factor Compensation Scheme

Consider the power factor[5] p.f relationship between real P_a and apparent power S.

$$\text{p.f.} = \frac{P_a}{S} = \cos\left(\theta_v - \theta_i\right). \tag{4.21}$$

Being θ_v and θ_i, the voltage and current phase angle, respectively. The ideal power factor is obtained when the current and voltage waveforms are in phase. Since $P_a = S\cos(\theta_v - \theta_i)$ and $Q_r = S\sin(\theta_v - \theta_i)$, the only way in which unitary power factor is achieved, results when the reactive power is eliminated, this is $Q_r \to 0$. Otherwise, the remaining reactive power will produce a lagging or leading power factor due to the connection of inductive or capacitive loads. Therefore it is of interest the power factor correction to achieve efficient power consumption. The power factor correction proposed idea is depicted in Figure 4.18, which is based on the use of an electronic power converter (DC/AC), capable of injecting sufficient current at the PCC, in order

[5] *The power factor is the cosine of the phase difference between voltage and current it is also the cosine of the angle of the load impedance. The power factor is dimensionless since it is the ratio of the average power to the apparent power. The power factor may be seen as that factor by which the apparent power must be multiplied to obtain the real or average power. The value of the p.f. ranges between zero and unity[Alexander, 2017].*

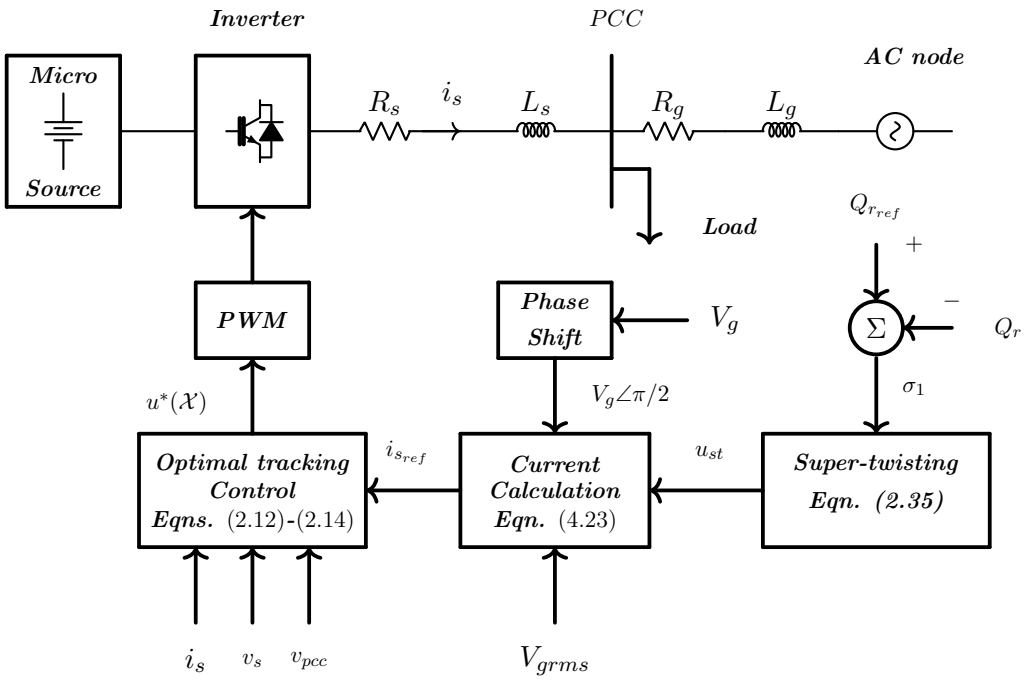

Figure 4.18: Power factor correction control scheme.

to regulate the power factor. This is achieved through the nonlinear optimal control in combination with sliding modes based on nested control loops, as described in Chapter 2, where an external control loop based on sliding modes, super-twisting (2.35), calculates the required reactive power reference that the converter must inject in order to reach the desired power factor (ideally p.f.=1). This is accomplished using the selection of a sliding surface σ_1 based on the difference between a desired reactive power reference $Q_{r_{ref}}$ and the reactive power Q_r measured at the PCC. Therefore the sliding surface for the super-twisting controller (2.35) is designed as $\sigma_1 = Q_{r_{ref}} - Q_r$. The super-twisting external control loop provides a power reference necessary to reach the sliding manifold in which the following conditions holds

$$\lim_{t\to\infty} \sigma_1 = 0 \implies Q_{r_{ref}} - Q_r = 0 \tag{4.22}$$

If the reactive power reference is defined as $Q_{r_{ref}} = 0$, the only possible solution to fulfill (4.22) is given by the elimination of the reactive power drawn at the PCC by the load; this is $Q_r = 0$. This means that only real power P_a will be drawn to the main utility grid, ensuring unitary power factor. Because the power converter output is a current signal, it is necessary to transform the power reference (generated by the S.T. control loop (2.35)) into a current reference in order to control the power factor through a current profile indirectly. The inner loop current control reference i_{ref} is calculated based on the idea given in [Ramos-Paz et al.,] as follows

$$i_{ref} = \frac{SV_s}{V_{s_{rms}}^2} \tag{4.23}$$

where S is the apparent power, V_s is the voltage measured at the PCC, $V_{s_{rms}}$ is the V_s RMS voltage. The equation above is derived from the expression, where a dummy variable is introduced.

$$S = V_{rms} i_{rms} \left(\frac{V_{rms}}{V_{rms}} \right) \tag{4.24}$$

then, by solving for i_{rms} and multiplying the left and right hand sides of (4.24) by $\sqrt{2}\sin(\omega t)$, it follows that

$$i_{rms}\sqrt{2}\sin(\omega t) = \frac{S V_{rms}}{V_{rms}^2}\sqrt{2}\sin(\omega t) \tag{4.25}$$

where $V_s \angle \Delta = V_{rms}\sqrt{2}\sin(\omega t + \Delta)$ and Δ is an arbitrary phase angle.

Remark 3: Notice that by multiplying by the factor $\sqrt{2}\sin(\omega t + \Delta)$, the resulting reference current i_{ref} will have an arbitrary Δ phase angle, which is assumed to be the same of V_s. However, for the purposes of p.f. correction, it is required to produce reactive power Q_r which is completely obtained when $|\theta_v - \theta_i| = \frac{\pi}{2}$, this means that all the apparent power $S = |\mathbf{S}| = |P_a + jQ_r|$ will be converted into reactive power. Therefore, it is necessary to shift the phase of the measured signal V_s by $\varphi = \frac{\pi}{2}$. For this purpose, the PCC voltage V_s can be modeled by defining $\Psi_1 = \mathcal{A}\sin(\omega t)$, and $\Psi_2 = \mathcal{A}\cos(\omega t)$, where $\mathcal{A}$ is the PCC voltage amplitude and $\omega = 2\pi f$ being f the fundamental grid frequency. Thus, the shifted signal by $\frac{\pi}{2}$, can be obtained from the following exosystem.

$$\begin{aligned} \frac{d\Psi_1}{dt} &= \omega\Psi_2 + \Gamma(V_s - \Psi_1), \qquad \Psi_1(0) = 0 \\ \frac{d\Psi_2}{dt} &= -\omega\Psi_1, \qquad \Psi_2(0) = \mathcal{A}. \end{aligned} \tag{4.26}$$

The term $\Gamma(V_s - \Psi_1)$ is used in order to identify the amplitude of the PCC voltage, where Γ is a constant parameter (tuned to synchronize the signal from the exosystem with the signal from the electrical grid). Therefore, it is possible to indirectly control the reactive power injected into the PCC through an inner current control loop. Finally, in order to track the desired reference current i_{ref} provided by the external control loop (2.35). An internal control loop based on optimal control (2.12)-(2.14), is used with the objective of directly controlling the output current of the power electronic converter.

4.2.2. Power Factor Correction Case of Study

Refer to the power system configuration shown in Figure 4.19, which consist of a single-phase AC node linked to the main utility grid, where a set of RL loads are connected at the PCC, which are switched at different time instances, demanding real and reactive power to the main utility grid. Then, as a consequence, the power factor drops. To

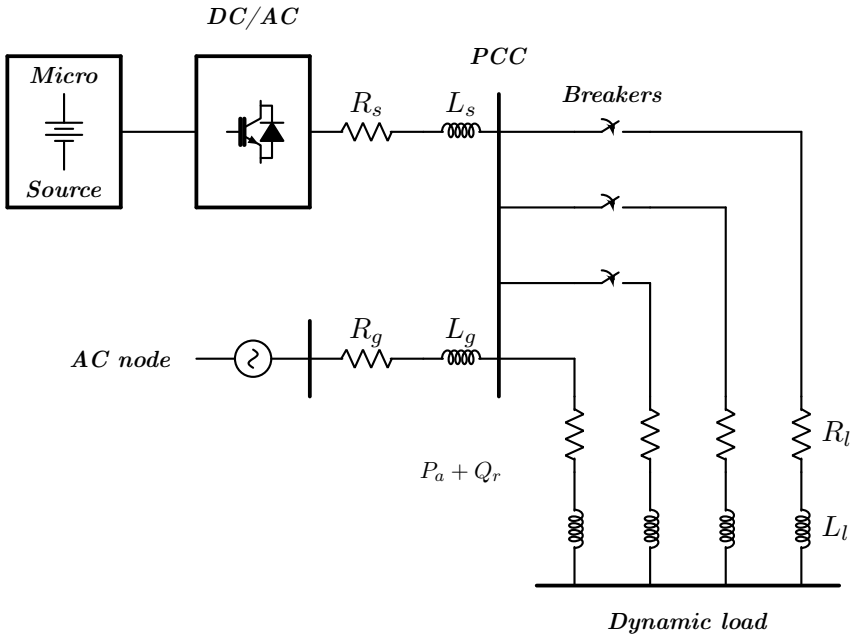

Figure 4.19: Power factor correction case of study, dynamic load.

deal with the power factor issue, a DC/AC power electronic inverter is connected to the PCC through an RL branch, to inject the required reactive power according to the power factor correction control scheme (Figure 4.18) to achieve unitary power factor.

Simulation Results

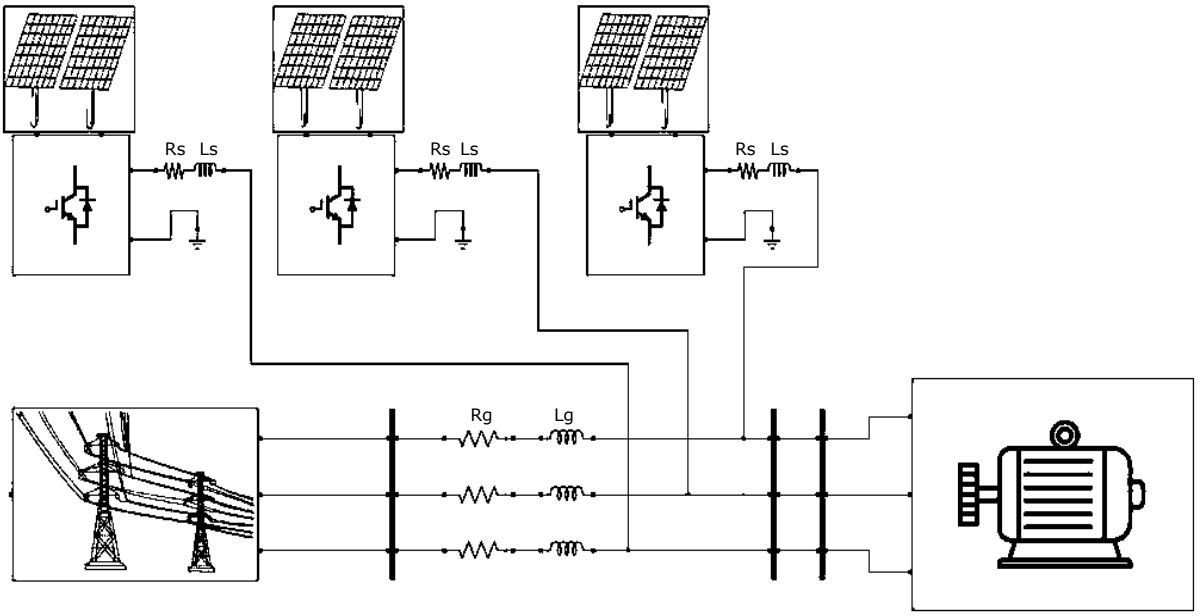

Figure 4.20: Microgrid power factor compensation scheme through ancillary services.

Table 4.1: Power system parameters,[Fan, 2017]

Parameter	Description	Units
V_{DC}	DC source voltage	$1000V$
R_s	Filter resistance	$1m\Omega$
L_s	Filter inductance	$18mH$
V_g	Grid voltage	$180V$
R_g	Grid resistance	0.01Ω
L_g	Grid inductance	$18\mu H$
f	Grid frequency	$60Hz$

In order to demonstrate the effectiveness of the proposed power factor correction control scheme, through a power electronic converter. A MATLAB/Simulink® simulation was conducted as follows: A power system configuration was implemented shown in Figure 4.19, considering a discrete step size of $1\mu s$ and the system parameters chosen as described in Table 4.1. In addition to the purpose of demonstrating the robustness properties of the controller, abrupt load changes were produced in accordance with

$$Load = \begin{cases} 10\,\text{KW} + 5\,\text{KVAR} & t \leq 0.8s \\ 11\,\text{KW} + 6.5\,\text{KVAR} & 0.8s < t \leq 1.6s \\ 12\,\text{KW} + 8\,\text{KVAR} & 1.6s < t \leq 2.4s \\ 13\,\text{KW} + 9.5\,\text{KVAR} & t > 2.4s \end{cases}$$

Therefore, by the increment in the power consumption, the system power factor will drop, and in this sense, it will be compensated by the proposed control scheme. For the outer control loop the super-twisting (2.35) gains were chosen as $\lambda_1 = 100$ and $\lambda_2 = 9000$. For the inner optimal control loop the performance index (2.10) gains were selected as $Q = 100$ and $R = 4$. In addition, for the phase shift exosystem, the gain for the grid synchronization function was chosen as $\Gamma = 2000$.

Figure 4.21(a) shows the convergence of the sliding surface σ towards zero, ensuring the elimination of the reactive power at the PCC. Fig 4.21(b) depicts the super-twisting outer control signal, which represents the required apparent power reference, which is transformed into a current reference.

Figure 4.22 represents the nonlinear optimal tracking control of i_{ref}, where it's possible to appreciate how the inverter output current i_s tracks the desired current reference, provided by the outer control loop.

Figure 4.23(a) depicts the elimination of the reactive power measured at the PCC, as a result of the convergence of the sliding surface $\sigma \to 0$, Figure 4.23(b) shows the active power consumption by the load which will be the only power that will be drawn to the AC utility grid, since the required reactive power will be provided by the inverter.

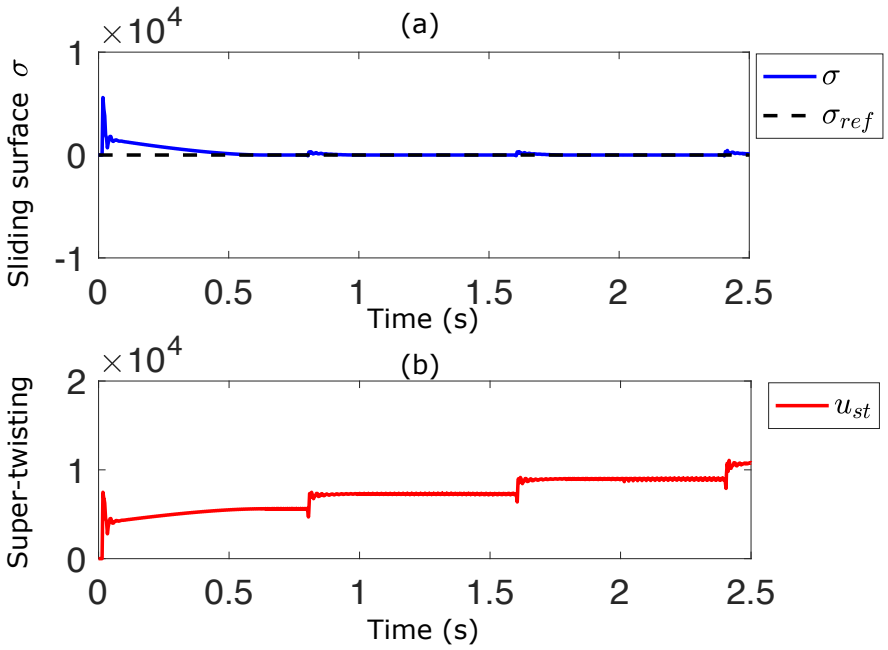

Figure 4.21: (a) Super-twisting sliding mode surface; (b) super-twisting generated reference signal.

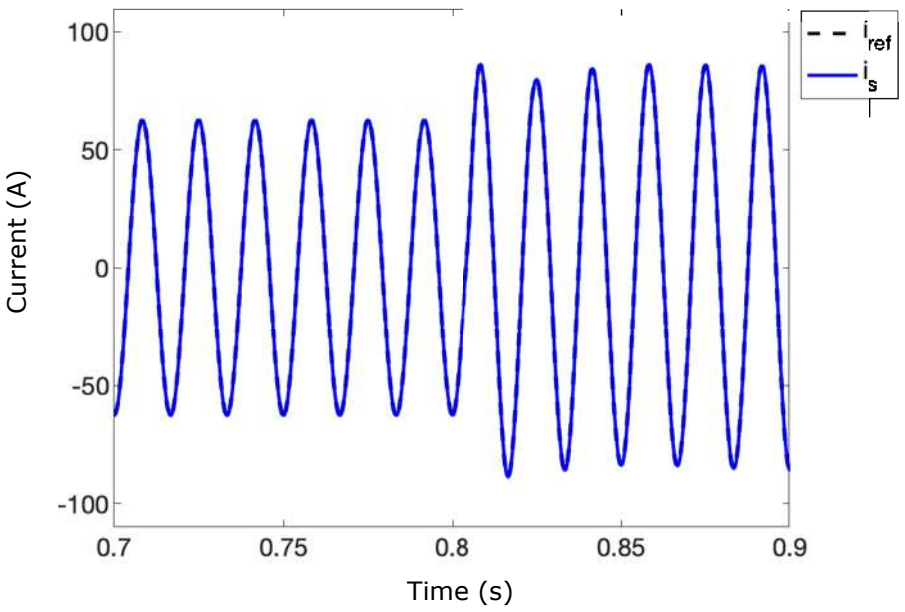

Figure 4.22: Optimal tracking control for the grid current reference.

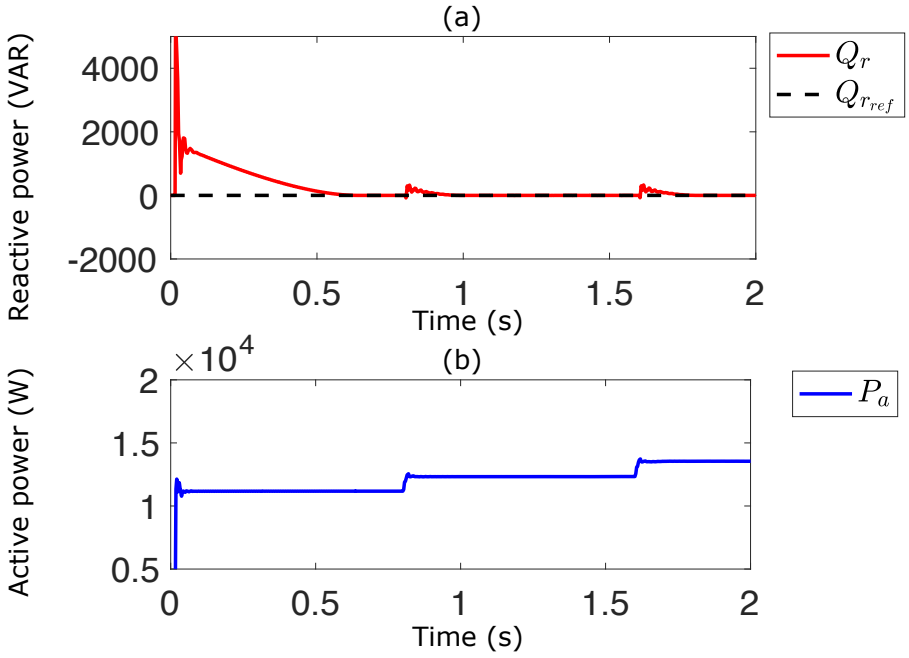

Figure 4.23: (a) Active power consumption, measured at the PCC; (b) reactive power consumption, measured at the PCC.

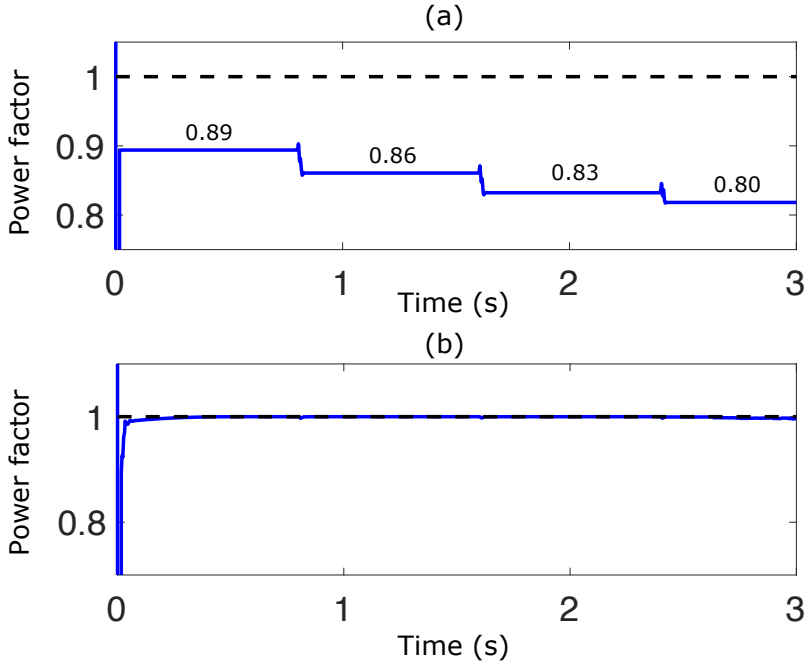

Figure 4.24: Power factor, without power factor correction (a) and with power factor correction (b).

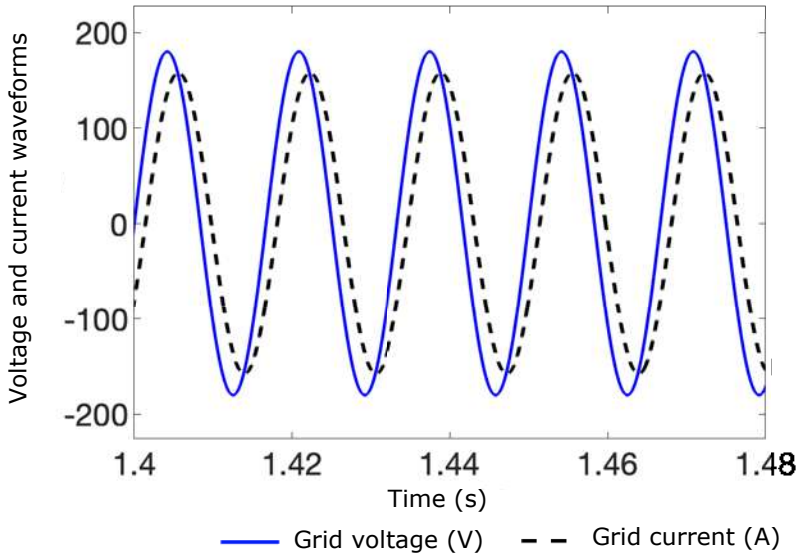

Figure 4.25: Phase angle between the grid voltage V_g and current i_g waveforms before the power factor correction.

Figure 4.24(a) shows the power factor, considering the abrupt load changes, without the proposed power factor correction scheme. On the other hand, Figure 4.24(b) depicts the achievement of the unitary power factor considering the proposed power factor correction scheme.

Figure 4.25 depicts the phase difference between the grid voltage V_g and the grid current i_g waveforms, resulting in a lower power factor. This is without the power factor correction. Nonetheless Figure 4.26 shows how, during the power factor correction, V_g and i_g are in phase, resulting in unitary power factor.

It is worth remarking that the dynamic power factor compensation is possible in a node of the electrical power grid with the proposed control strategy. Although the primary energy source for the power electronic converter can come from a renewable energy source, this scheme can also be implemented with a shunt configuration. The advantage of this proposal compared to solutions based on connecting capacitors in parallel is that this is a configuration is adapted to the needs or requirements based on the consumption of a power grid node. In the same way, this scheme can only be used when necessary. And then, during another operating condition, the electronic power converter can change its control objective to supply power to the electrical power grid or harmonic compensation, shown in the previous section of this Chapter.

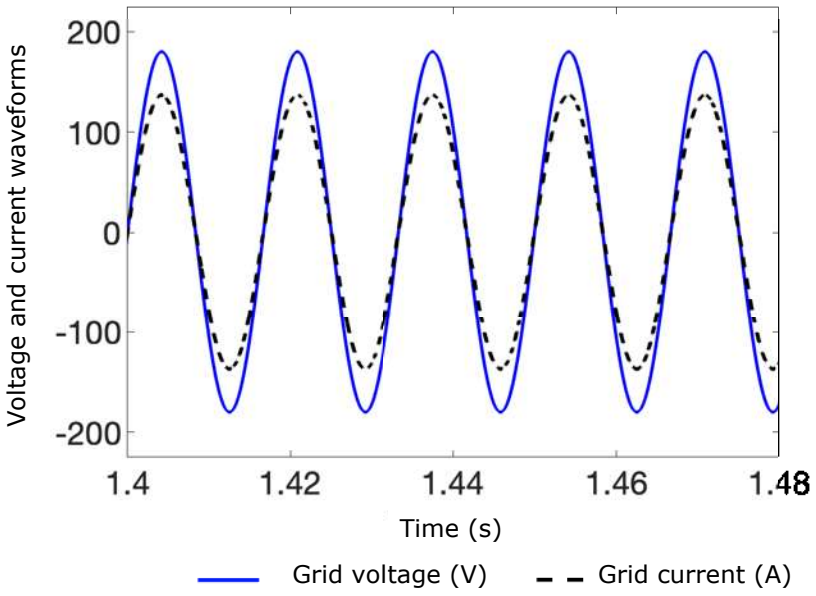

Figure 4.26: Grid voltage V_g and current i_g waveforms in phase after the power factor correction.

4.3 The Voltage Regulation Assessment

This section presents a nonlinear optimal and robust control scheme applied for voltage regulation in an electrical power grid node through power electronic converters acting as microgrid ancillary services. The voltage regulation is achieved by using a series of nested control loops based on nonlinear optimal tracking control and sliding mode control. In the event of voltage variations at the common coupling point (PCC), the proposed control scheme drives the electronic power converter to inject the necessary power to the grid node to perform voltage compensation. Simulation results demonstrate the effectiveness of the present control scheme.

4.3.1. Proposed Voltage Regulation Scheme

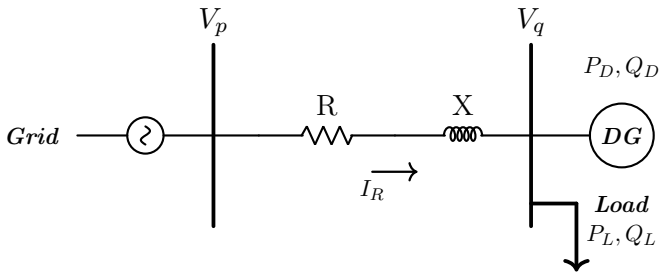

Figure 4.27: Simple radial electrical distribution system with a distributed generation node.

Consider a simple radial system as depicted in Figure 4.27, where X and R are the reactance and resistance of the line connecting the distributed generation (DG) node to the main utility grid, P_L and Q_L are the load active and reactive power consumption. DG is a distributed generation node that may be based on renewable power sources (i.e., solar, battery, etc.) with P_D and Q_D active and reactive power production, respectively, V_1 and V_2 are the sending and receiving end voltage.

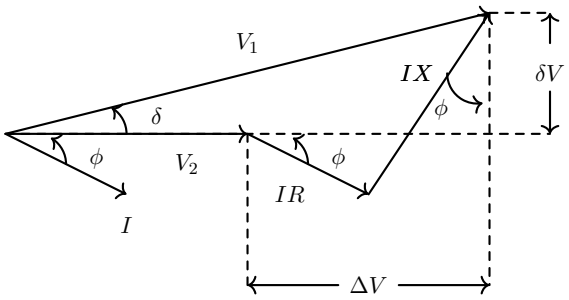

Figure 4.28: Voltage drop diagram.

Suppose that the receiver load behaves like a combination of resistors and coils (which is the most typical case for industrial consumers). In this sense, total current presents an angle of phase to the voltage between $0°$ and $-90°$ and thus, passage of this current through the resistance and inductance of the line represents a voltage drop, shown in Figure 4.28, where

$$\begin{aligned} V_1^2 &= (V_2 + \Delta V)^2 + \delta V^2 \\ V_1^2 &= (V_2 + IR\cos(\phi) + IX\sin(\phi))^2 + (IX\cos(\phi) - IR\sin(\phi))^2 \end{aligned} \tag{4.27}$$

then, defining the active and reactive power as

$$P_a = V_2 I\cos(\phi) \qquad Q_r = V_2 I\sin(\phi) \tag{4.28}$$

It follows that

$$V_1^2 = \left(V_2 + \frac{P_a R}{V_2} + \frac{Q_r X}{V_2}\right)^2 + \left(\frac{P_a X}{V_2} - \frac{Q_r R}{V_2}\right)^2 \tag{4.29}$$

Comparing (4.27) and (4.29)

$$\Delta V = \frac{P_a R + Q_r X}{V_2} \qquad \delta V = \frac{P_a X - Q_r R}{V_2} \tag{4.30}$$

It results that ΔV represents the voltage drop to the magnitude of V_1 and δV is the voltage drop for the voltage angle V_1.

Assumption 1: In general, the X/R ratio is relatively low in a distribution power grid, especially in a weak distribution feeder with high impedance [Mujal, 2019]. This

is because the geometric mean distance between the conductors is shorter within the distribution system than overhead transmission lines. Therefore according to (4.30), a significant amount of power injected by the distributed generation node will result in a voltage increase or drop in the electrical power system. Lower X/R ratios increase the voltage level, however, higher X/R ratios decrease the voltage profile at the PCC and imposes the need for more reactive power support [Alizadeh et al., 2016].

The voltage compensation will depend on several factors, such as the power capability of the distributed generation. Figure 4.29 depicts a typical voltage compensation application for power systems based on the proposed scheme. Where an outer control loop based on super-twisting sliding modes (2.35) generates the power reference, with a sliding surface designed based on the voltage drop measured at the PCC as $\sigma_2 = V_{ref} - V_{pcc}$. Then the required current to be injected at the PCC is calculated based on (4.23). Finally, the reference current i_{ref} its tracked by means of a nonlinear optimal tracking control (2.12)-(2.14) of a DC/AC converter.

The Voltage Controller Design

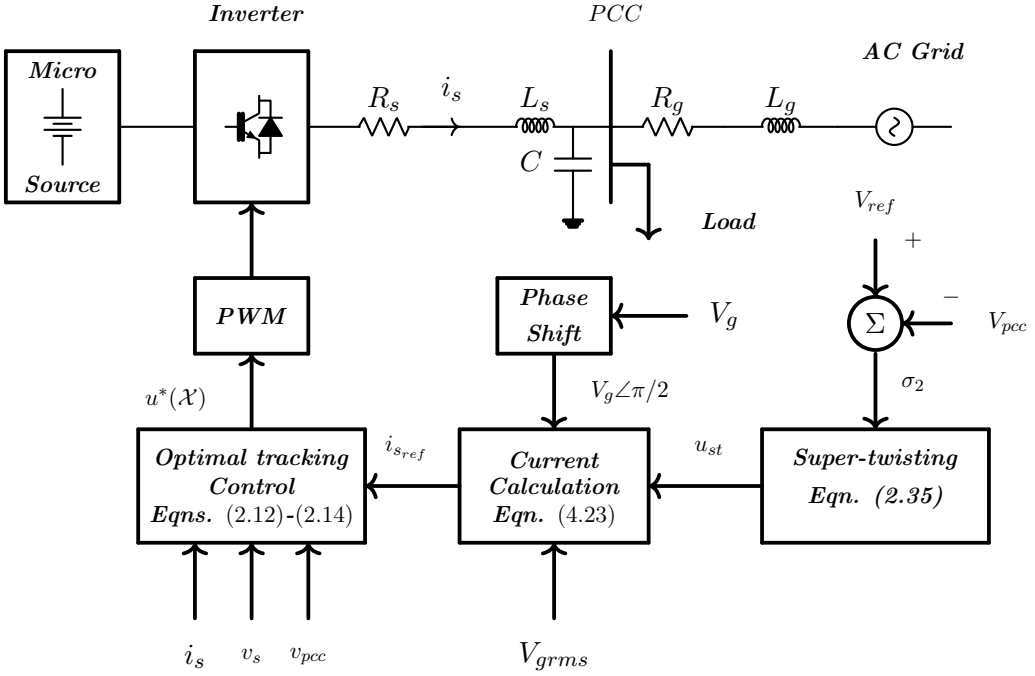

Figure 4.29: Voltage compensation control scheme.

Consider a single-phase grid-connected inverter shown in Figure 4.30. where L_s, R_s are the inductance and resistance on the inverter-side respectively, C is the filter capacitor, L_g and R_g are the inductance and equivalent resistance on the grid-side respectively, E represents the output voltage of the inverter, V_g is the AC voltage of the utility grid, i_s is the current flowing through the LC branch on the inverter side, i_g is the current flowing through the utility-grid branch and V_c is the voltage on the filter capacitor. In

addition, an RL load is connected to the system where R_l represents the load resistance and L_l is the load inductance.

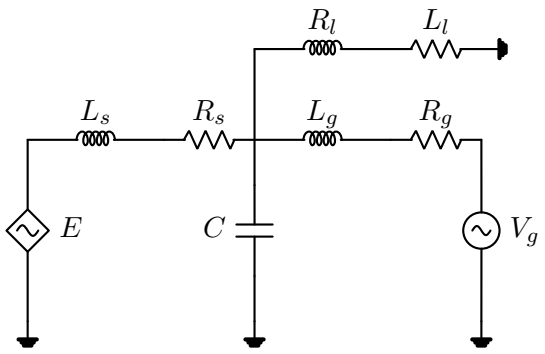

Figure 4.30: Single-phase equivalent circuit of a grid-tied power electronics converter with an LCL filter.

The dynamic equations of the circuit modeled on the abc reference frame by applying the Kirchhoff laws are described as

$$\begin{aligned}
\frac{di_s}{dt} &= \frac{1}{L_s}E - \frac{R_s}{L_s}i_s - \frac{1}{L_s}V_c \\
\frac{di_g}{dt} &= \frac{1}{L_g}V_c - \frac{R_g}{L_g}i_g - \frac{1}{L_g}V_g \\
\frac{di_l}{dt} &= \frac{1}{L_l}V_c - \frac{R_c}{L_l}i_l \\
\frac{dV_c}{dt} &= \frac{1}{C}i_s - \frac{1}{C}i_g - \frac{1}{C}i_l
\end{aligned} \tag{4.31}$$

The grid voltage V_g can be represented in terms of an exo-system, defining

$$V_g = A\sin(\omega t) \qquad W_g = A\cos(\omega t) \tag{4.32}$$

where

$$\begin{aligned}
\frac{dV_g}{dt} &= \omega W_g \\
\frac{dW_g}{dt} &- \omega V_g
\end{aligned} \tag{4.33}$$

Then, consider the nonlinear optimal and robust control system for voltage regulation shown in Figure 4.29, which consists of the following elements: 1) a direct current source (which can be generated from a distributed generation node based on renewable energies); 2) a single-phase inverter, which allows the conversion from DC to AC; 3) an LC type filter, which allows the interface of the electronic power converter with the common coupling point with the distribution line; 4) a distribution line whose

parameters are modeled in a lumped way and modeled as the series effect of a resistive and inductive element and finally, the main electrical power grid. The main objective of the proposed control system is to guarantee voltage regulation at the common coupling point; that is, in the event of a voltage fluctuation on the side of the main electrical grid, the distributed generation node must supply the necessary power to compensate the voltage variation, this is done by considering a nonlinear optimal control scheme in combination with sliding modes as described in Chapter 2 as follows: The rms voltage is measured at the PCC, then an error signal is obtained from the difference between the measured voltage at the PCC and a reference voltage.

$$\sigma_1 = V_{pcc} - v_{ref} \tag{4.34}$$

Then the error signal is used in order to generate a power reference for the inverter by means of an outer, super twisting control loop (2.35), by choosing σ_1 as the sliding surface. In order to compensate the voltage fluctuations at the PCC, the inverter is required to inject a significant amount of power. In this sense, the inverter output power is proposed to be indirectly controlled by using an inner current control loop, where the current reference is given in terms of the required reference power and the grid voltage as seen in [Ramos-Paz et al.,].

$$i_{ref} = \frac{P_{ref} V_g}{V_{g_{rms}}^2} \tag{4.35}$$

Where, P_{ref} is the reference power generated by the outer control loop. From (4.35) the inverter output power is indirectly controlled through the current inner control loop by means of a super-twisting controller (2.35) with the sliding surface selected as

$$\sigma_2 = i_{ref} - i_g \tag{4.36}$$

It is worth mentioning that the proposed control scheme has the characteristic of presenting elements of robustness in the face of parametric uncertainties of the electrical distribution power grid by only depending on measurements of the voltages and currents of the grid that in turn serve to generate the sliding surfaces internal and external control loops.

4.3.2. Simulation Results

This section presents the simulation results obtained for the validation of the proposed robust voltage regulation scheme. For this, the MATLAB/Simulink® software was used, where an electrical distribution grid was implemented shown in Figure 4.29. Together with the proposed control scheme. The simulation was carried out as follows:

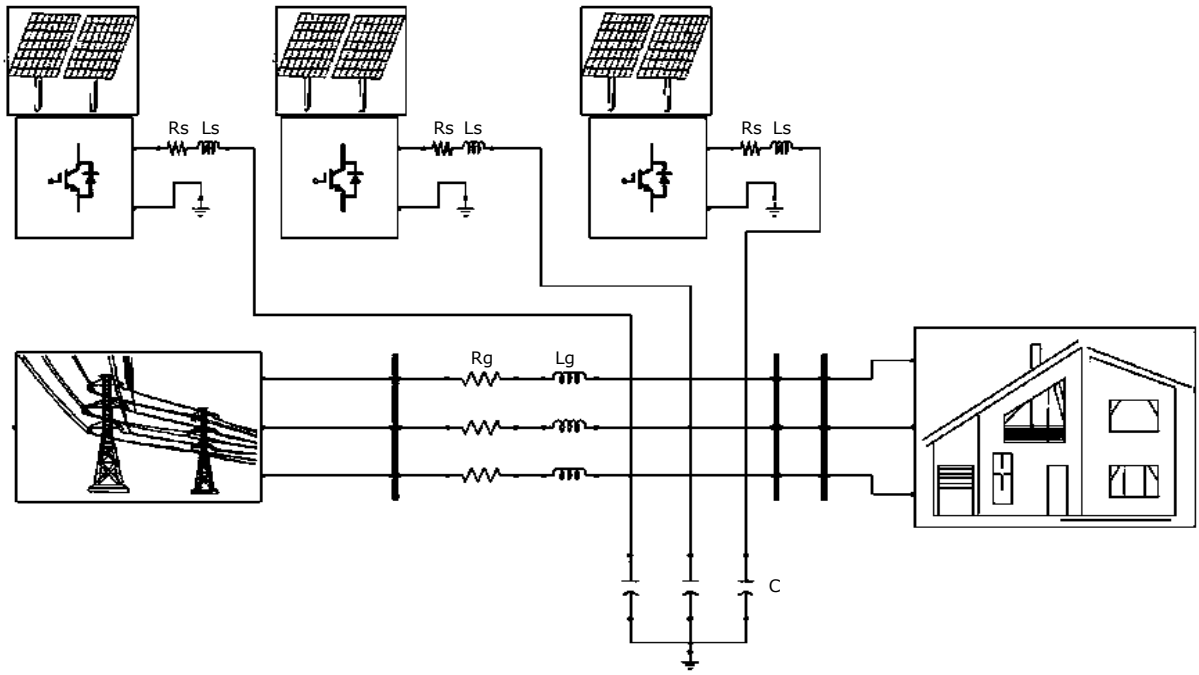

Figure 4.31: Microgrid voltage regulation scheme through ancillary services.

Consider a microgrid configuration as depicted in Figure 4.31. For the power electronic converters and the distribution grid, the simulation was performed considering the parameters as depicted in Table 4.2.

Table 4.2: Power system configuration parameters, [Fan, 2017]

Main parameters of the simulated system	
Filter	$L_s = 6.3mH$, $R_s = 3.5\Omega$
	$C = 10.3mF$, $V_{dc} = 800V$
Grid	$V_g = 120V_{rms}$, $R_g = 0.09\Omega$
	$L_g = 18mH$

Then a voltage variation was simulated at the main electrical grid side, where the grid voltage is represented as follows.

$$V_{g_{sag}} = \begin{cases} 0\% & t \leq 0.5s \\ 10\% & 0.5s < t \leq 1s \\ 0\% & 1s < t \leq 1.8s \\ 0.05\sin(\omega t) + 0.95\% & 1.8s < t \leq 2.5s \\ 0\% & 2.5s < t \leq 3s \end{cases}$$

In addition, an RL load is connected to the PCC, demanding 10 KVA, which, in order to demonstrate the robustness properties of the controller, has an abrupt change from 1 kVA to 2 kVA at $t = 2$s. Then, the proposed robust voltage control scheme is implemented considering the following controller parameters, for the outer power controller, the STA (2.35) was implemented by selecting the sliding surface as (4.34)

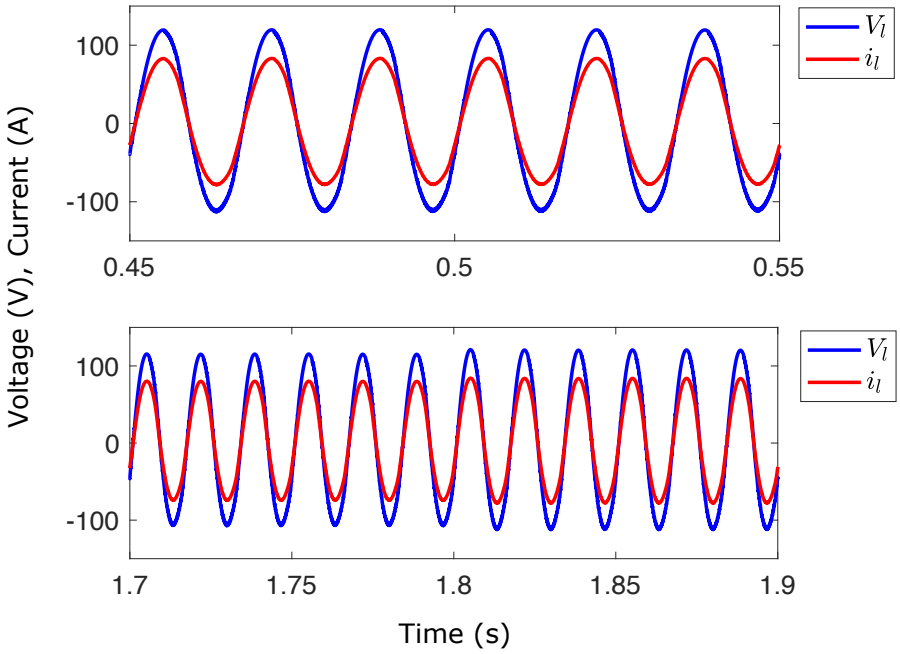

Figure 4.32: V_c and i_g measured at the PCC.

with $\lambda_1 = 100$ and $\lambda_2 = 10000$, finally, for the inner current control loop, the STA was implemented with the sliding surface as (4.36) with the controller gains selected as $\lambda_1 = 1000$ and $\lambda_2 = 20000$, and the optimal controller gain selected as $Q = 100$ and $R = 4$. The carrier frequency for the PWM inverter signal was selected to 100 kHz.

Figure 4.32 shows the voltage and the current measured at the PCC. It is important to notice that total harmonic distortion (THD) of the current signal is below 1.06%, which demonstrates that by using the proposed control strategy, it is possible to regulate the voltage al the PCC without compromising the harmonic distortion of the current waveform i_g.

Figure 4.33 Depicts the voltage regulation at the PCC, where it is possible to appreciate that despite the voltage variation in the main electrical power grid, the proposed control scheme guarantees voltage regulation, it is possible to appreciate that there is a certain error in steady-state, this is due to the fact that the system has a relative degree other than 1, which makes impossible for the super-twisting controller to achieve an asymptotic convergence to the reference. However, it can be considered that this control scheme allows voltage regulation within a window allowed by the voltage regulation standards (i.e., IEEE Vision for Smart Grid Controls: 2030 and Beyond [Annaswamy and Amin, 2013]).

Figure 4.34 shows the THD content measured at i_g, which demonstrates the effectiveness of the controller for the voltage regulation without a negative effect in the harmonic

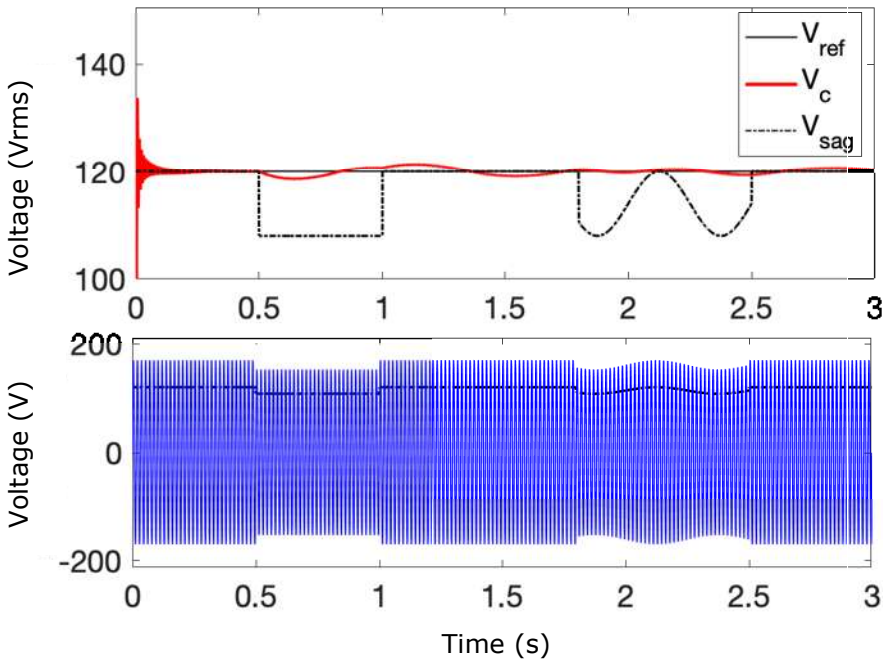

Figure 4.33: Voltage regulation at the PCC.

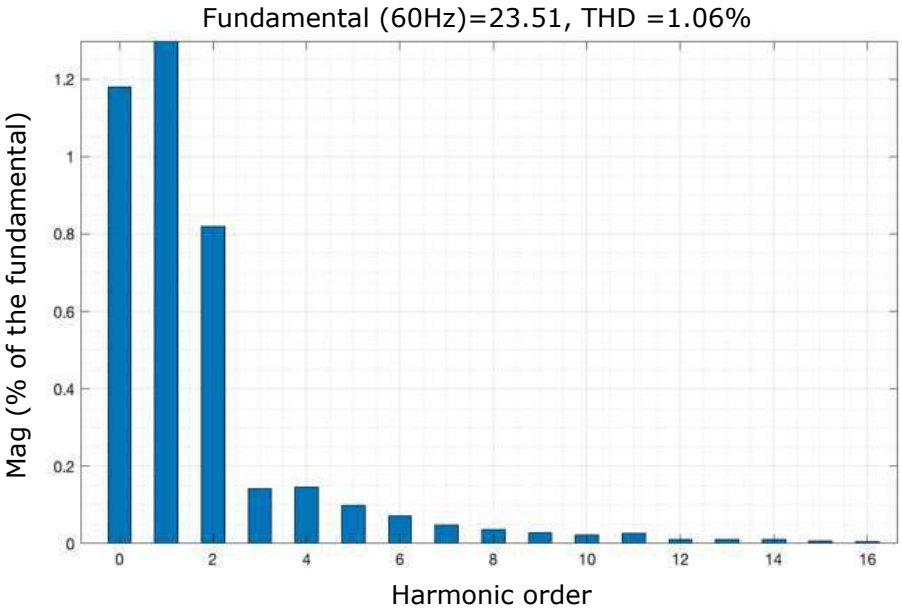

Figure 4.34: Total harmonic distortion measured at i_g.

distortion.

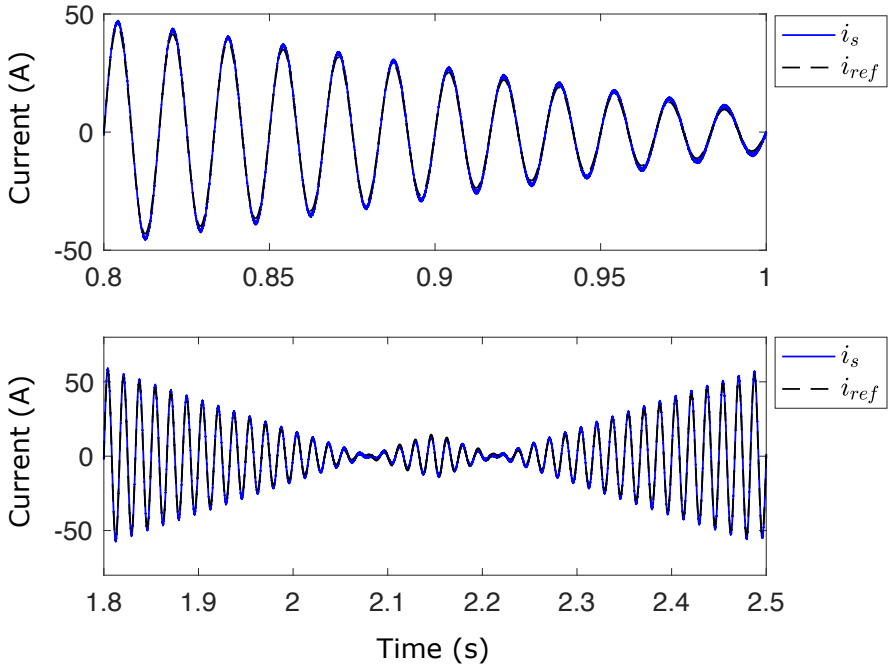

Figure 4.35: Robust tracking control for i_s.

Figure 4.35 shows the tracking control for the inverter output current i_s whose reference signal is generated by (4.35) by means of the outer power control loop. It is important to remark that the voltage compensation strategy is implemented by means of a single-phase inverter. Moreover, the aforementioned results can be expanded to three-phase electrical systems by using a parallel configuration of single-phase inverters, since each single-phase inverter has a dedicated or local controller for each phase, which enables the possibility to compensate unbalanced voltage fluctuations for three-phase systems.

4.3.3. The Three-phase Approach

The voltage regulation scheme presented in the section above is designed for single-phase power electronic converters. However, this section presents the control approach for three-phase power electronic converters that can support voltage regulation to a node of the electrical grid. As described in Chapter 2, the proposed control scheme is based on nonlinear optimal control combined with sliding modes. The controller design includes an external control loop based on sliding modes that emulate the dynamics of a drop-type controller in order to determine the power reference necessary to achieve voltage regulation. Subsequently, the power reference generated by the external control loop is given to the internal control loop based on nonlinear optimal control, which acts directly on the power electronic converter. Then, the power converter tracks a

reference power signal injected into the electrical power grid node. This control scheme is described in Figure 4.36.

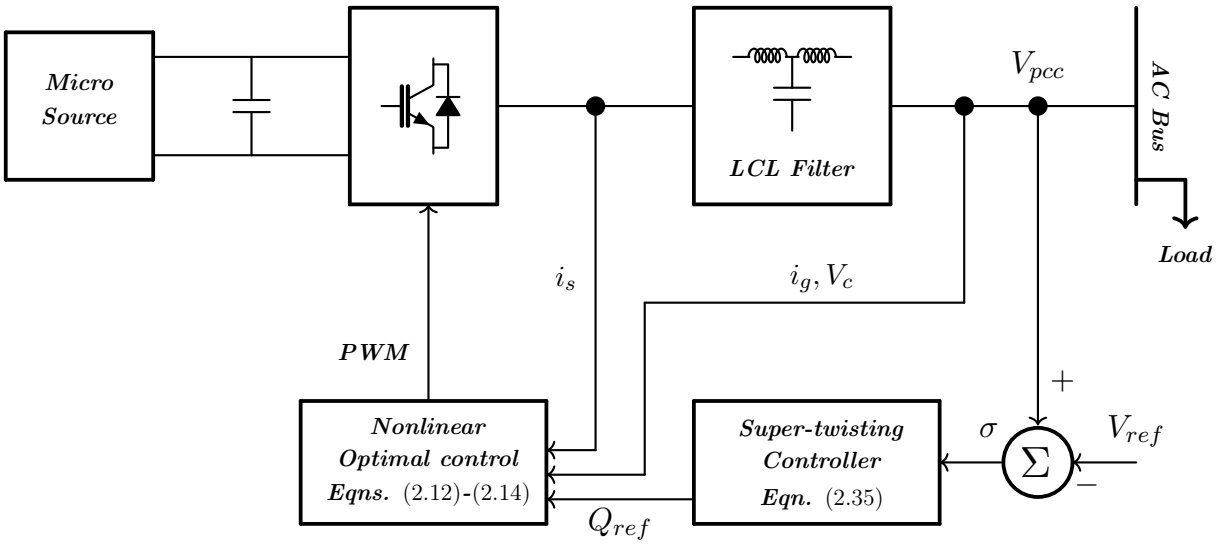

Figure 4.36: Proposed microgrid control system configuration.

Simulation Results

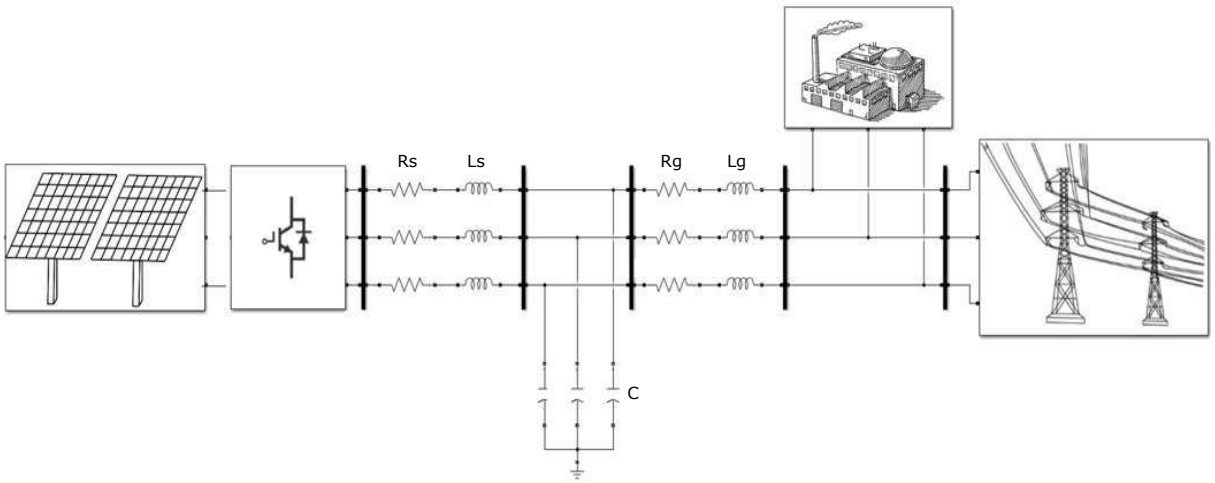

Figure 4.37: Microgrid voltage support scheme through ancillary services.

In order to demonstrate the effectiveness of the proposed control scheme, a simulation based on MATLAB/Simulink® was conducted as follows; Firstly, the simulation setup was done by using the power system Simulink® toolbox, based on the configuration depicted in Figure 4.36, implemented with the following system parameters, $V_g = 220V_{rms}$, $L_s = 0.002H$, $R_s = 3\Omega$, $C = 4\mu F$, $R_c = 10k\Omega$, $L_g = 0.002\Omega$, $R_g = 0.270\Omega$ and $E = 900V$. Then the nonlinear controllers (2.12) and (2.14) were programmed by using the MATLAB/Simulink® user-defined function block, with a simulation time step of $0.5\mu s$. Matrices for the nonlinear optimal control performance index (2.10) are

selected as $Q = [2000, 0; 0, 200]$ and $R = [0.001, 0; 0, 0.0005]$, with a reference vector $r = [P_a; Q_r]$. For the purposed of this work, $P_a = 0$ and $Q_r = u_{st}$ is commanded by the outer control loop (2.35), which is the output of the super-twisting controller; the super-twisting algorithm gains are $\lambda_1 = 10$ and $\lambda_2 = 200000$. Subsequently, an experiment was reproduced, where a swing generator type with a nominal voltage of 220 V_{rms} operating at a rated frequency of $60Hz$ is connected to a three-phase load, which demands 1 KVA and 5 KVAR with a nominal voltage of 220 V_{rms}, afterwards, a voltage variation is simulated at the PCC where $V_{pcc_{sag}}$ is defined as

$$V_{pcc_{sag}} = \begin{cases} 0\ \% & t \leq 0.5s \\ 50\% & 0.5s < t \leq 1s \\ 1\% & 1s < t \leq 1.5s \\ 30\% & 1.5s < t \leq 2s \\ 0\% & 2s < t \leq 2.5s \\ 0.2sin(2\pi t) + 0.8\% & 2.5s < t \leq 3.5s \\ 0\% & t > 3.5. \end{cases}$$

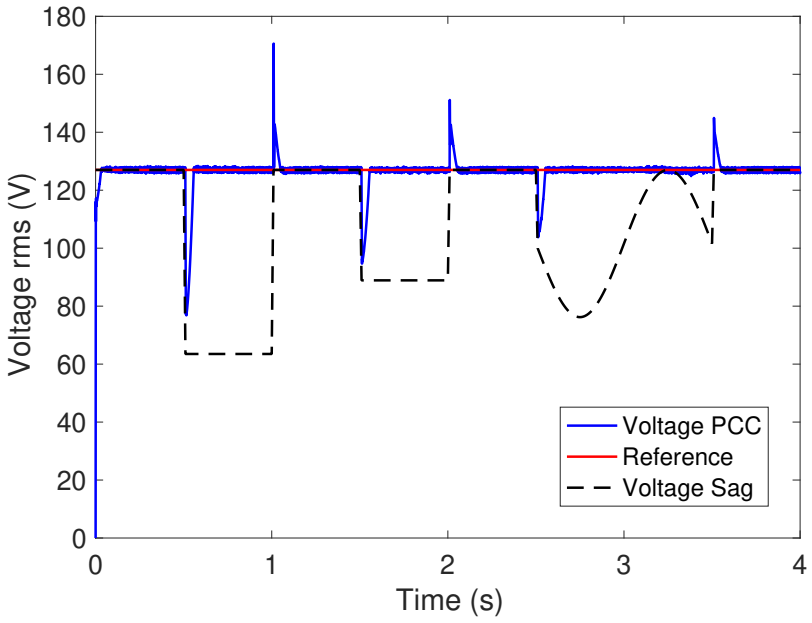

Figure 4.38: Voltage variation compensation and line to ground rms voltage at the PCC.

To evaluate the controller capabilities of rejecting time-varying voltage deviations, at the initial time $t = 2.5s$ to $t = 3.5s$ a sinusoidal function was simulated as a voltage fluctuation. Figure 4.38, depicts the line to ground rms voltage measured at the PCC, considering the voltage variation compensation strategy as is proposed in this thesis, where it is possible to observe the voltage compensation after a transient effect and how the voltage remains at a constant line to the ground value of $127V_{rms}$ which remains

within the allowable voltage range of about ±5%. In Figure 4.39, the active and reactive power delivered by the power electronic converter to the PCC is shown, where it is possible to observe how the inner control loop tracks the desired reactive power reference given by the outer control loop, while the active power was set to zero. Finally, Figure 4.40, depicts the three-phase line to the ground voltage, while the voltage variation compensation is measured at the PCC during the simulation.

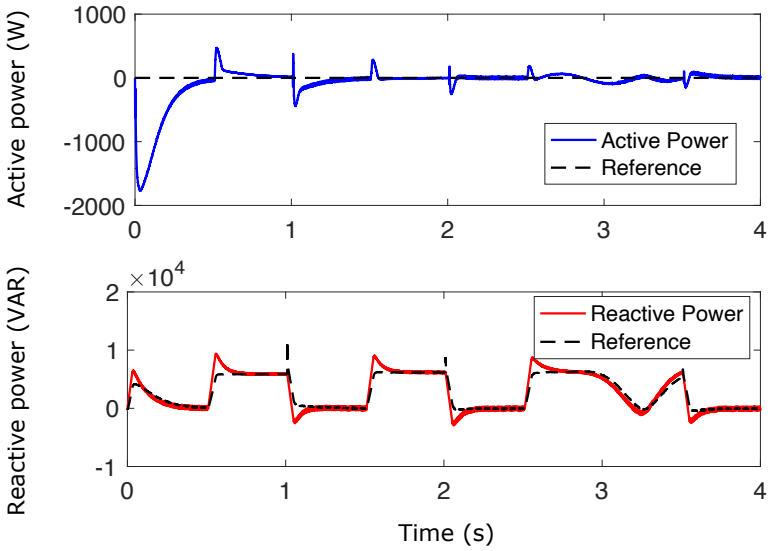

Figure 4.39: Active and reactive power tracking control, during the voltage variation compensation.

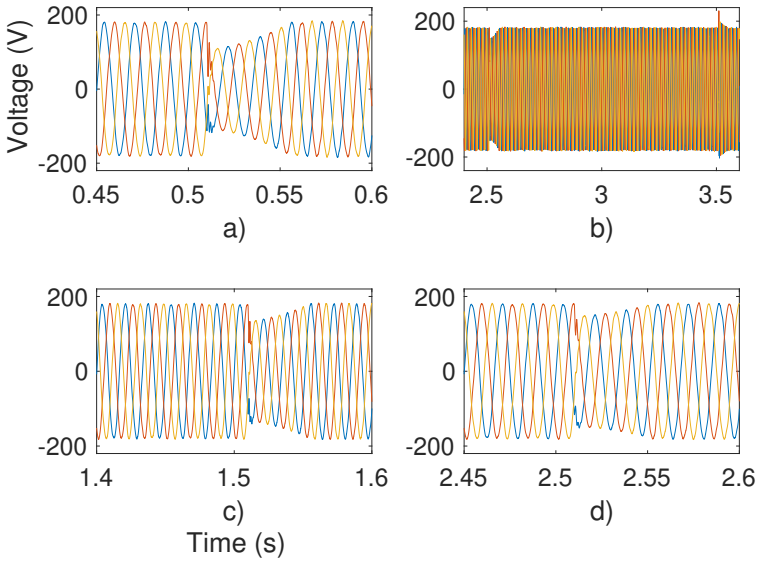

Figure 4.40: Three-phase measurement rms voltage variation compensation. a) 50% variation compensation, b) and d) time-varying voltage variation compensation and c) 30% voltage variation compensation.

4.4 The Multipurpose Approach

This section describes a typical application concerning the compensation of different power-quality phenomena as mentioned in the previous sections of this Chapter, considering an holistic approach.

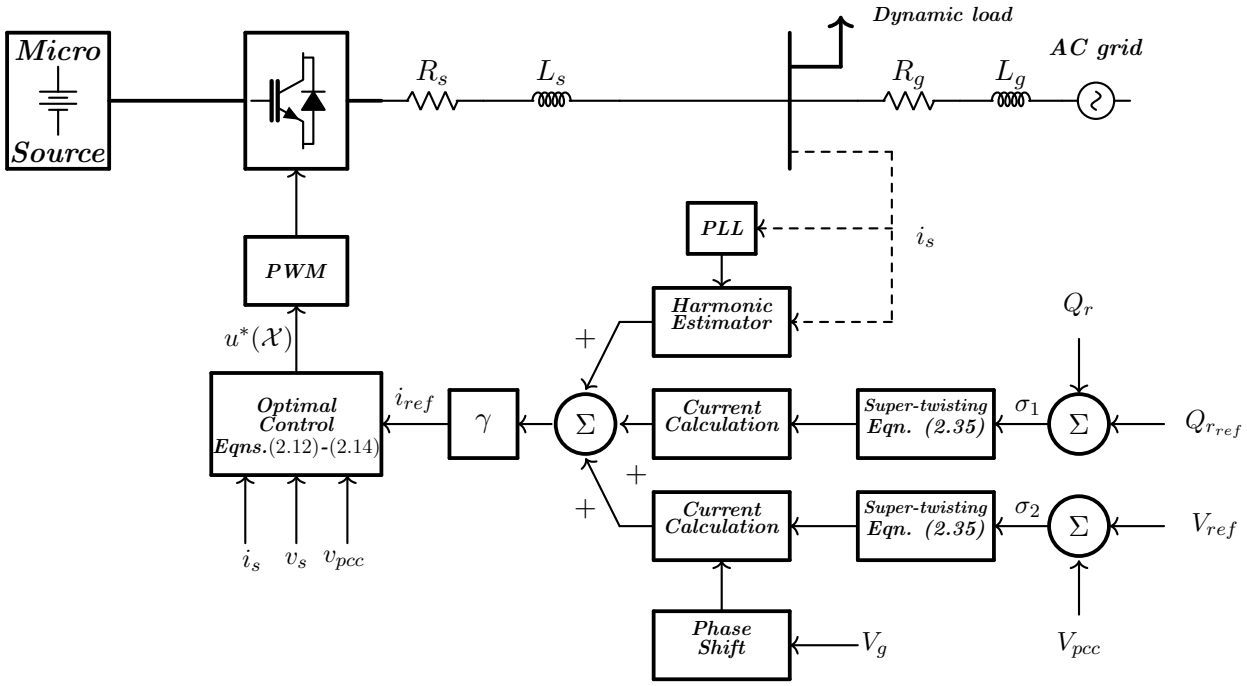

Figure 4.41: Proposed voltage Control System Configuration.

As depicted in Figure 4.41, consider a power system configuration with a nonlinear dynamic load connected to an AC power grid. This dynamic load may introduce harmonic distortion to the electrical power grid. In addition, it may vary its power consumption producing a lagging power factor or a voltage variation may occur at the grid-side. Then, to compensate the aforementioned power quality issues, a DC/AC electronic power conditioner is equipped with the proposed control schemes:

- Harmonic/interharmonic supresssion scheme as described in section 4.1.
- Power factor correction scheme as described in section 4.2.
- The voltage regulation scheme as described in section 4.3.

Along with a decision function Λ which prioresses the power quality issue to be solved. In this research, it is proposed that the function Λ is a boolean type variable that determines the activation of the required control scheme based on the power quality problem to be solved. In this sense the power conditioning application function as an ancillary device to the electrical power grid to compensate different power quality

problems with a single power electronic converter.

It is essential to highlight that the proposed power quality enhancement schemes (harmonics compensation, power factor correction, and voltage regulation) can be extended to the three-phase case by considering an individual single-phase inverter at each phase. This configuration has an essential characteristic since by doing so, it is possible to compensate different power quality issues at each phase, even for unbalanced three-phase systems.

4.4.1. Simulation Results

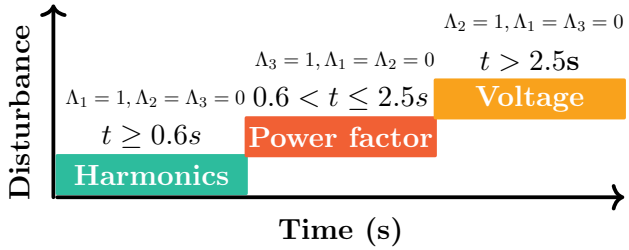

Figure 4.42: Simulated power quality disturbances at the PCC.

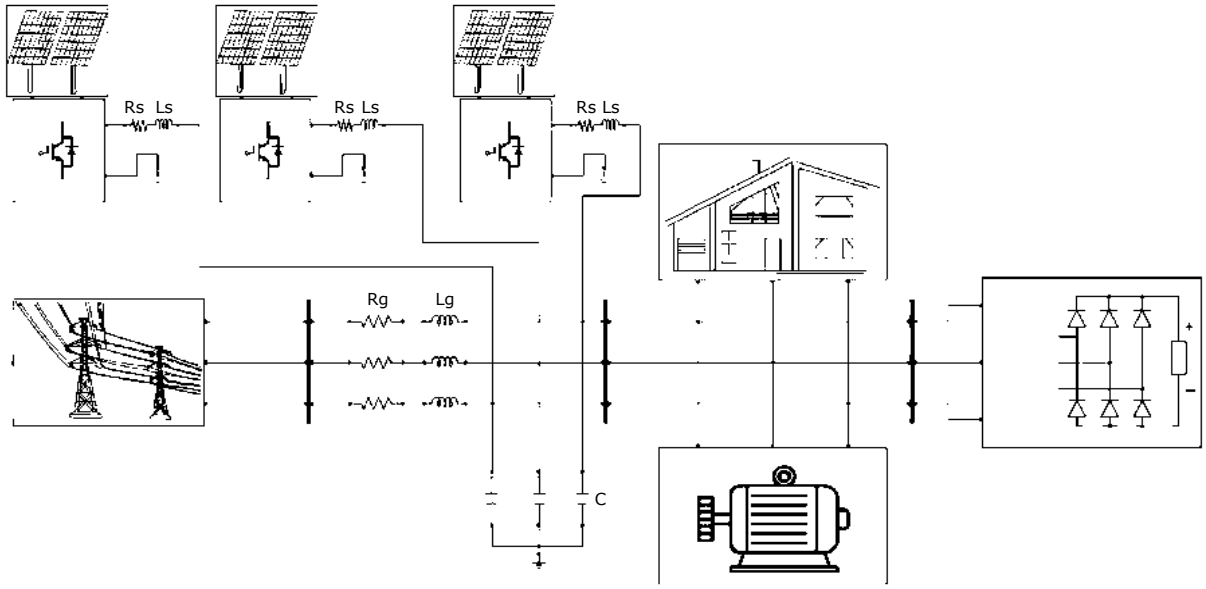

Figure 4.43: Microgrid power quality enhancement scheme through ancillary services.

In order to demonstrate the effectiveness of the proposed power-quality enhancement control scheme, a MATLAB/Simulink® simulation was conducted as follows: consider a microgrid configuration as described in Figure 4.43, with a discrete step size of

Table 4.3: Power system parameters, [Fan, 2017]

Parameter	Description	Units
V_{DC}	DC source voltage	$1000V$
R_s	Filter resistance	$1m\Omega$
L_s	Filter inductance	$18mH$
V_g	Grid voltage	$220V$
R_g	Grid resistance	$5.738m\Omega$
L_g	Grid inductance	$0.57mH$

Table 4.4: Simulated power quality issues at the PCC

Power quality issue	Duration	Λ_i value
Harmonic distortion	$t \leq 0.6s$	$\Lambda_1 = 1, \Lambda_2 = 0, \Lambda_3 = 0$
Lagging power factor	$0.6s < t \leq 2.5s$	$\Lambda_1 = 0, \Lambda_2 = 0, \Lambda_3 = 1$
Voltage variation	$t > 2.5s$	$\Lambda_1 = 0, \Lambda 2 = 1, \Lambda_3 = 0$

$0.8\mu s$ with the power system parameters as described in Table 4.3. Then different power-quality issues were simulated at the PCC at different time instants according to Table 4.4. Firstly, the harmonic distortion is produced by an uncontrolled rectifier load which is approximated by the following signal, as described in [Williams and Hoft, 1991].

$$\begin{aligned} s =& A_i \sin(\alpha_l t + \theta) + A_h \sin(\alpha_h t + \theta_h) + A_f \sin(\alpha_f t + \theta_f) + A_3 \sin(\alpha_3 t + \theta_3) \\ &+ A_5 \sin(\alpha_5 t + \theta_5) + A_7 \sin(\alpha_7 t + \theta_7) \end{aligned} \tag{4.37}$$

where $\alpha_n = 2\pi nf$ is the angular frequency in rad/s for the n-th harmonic, being $\alpha_3, \alpha_5, \alpha_7$ and α_f the odd and fundamental frequencies respectively, with α_i being a low order interhamonic frequency (sub-harmonic) and α_h a high order interharmonic, both non-integer multiples w.r.t the fundamental, which for this application is taken as $60Hz$. A_n are the amplitudes of the harmonics and θ_n the phases. The estimator parameters are given in Table C.1 (see Appendix C). Notice that (4.37) is composed of harmonic and interharmonic terms, whereby the use of the proposed online estimator is possible to estimate the frequency, amplitude, and phase for each harmonic component. Subsequently, in order to demonstrate the capability of the controller to compensate the power factor variation, abrupt load changes were produced as follows.

$$Load = \begin{cases} 10\,\text{KW} + 5\,\text{KVAR} & t \leq 0.8s \\ 11\,\text{KW} + 6.5\,\text{KVAR} & 0.8s < t \leq 1.6s \\ 12\,\text{KW} + 8\,\text{KVAR} & 1.6s < t \leq 2.4s \\ 13\,\text{KW} + 9.5\,\text{KVAR} & t > 2.4s. \end{cases}$$

Therefore, by the increment in the power consumption by the effect of the connection of inductive and resistive loads (simulated by power electronic elements in order to

increase the reactive power consumption), the power factor will drop, and in this sense, it will be compensated by the proposed control scheme. Finally, voltage variation is simulated as defined in Table 4.4 and Figure 4.42 the voltage variation is described by a 12% voltage reduction of the nominal PCC voltage.

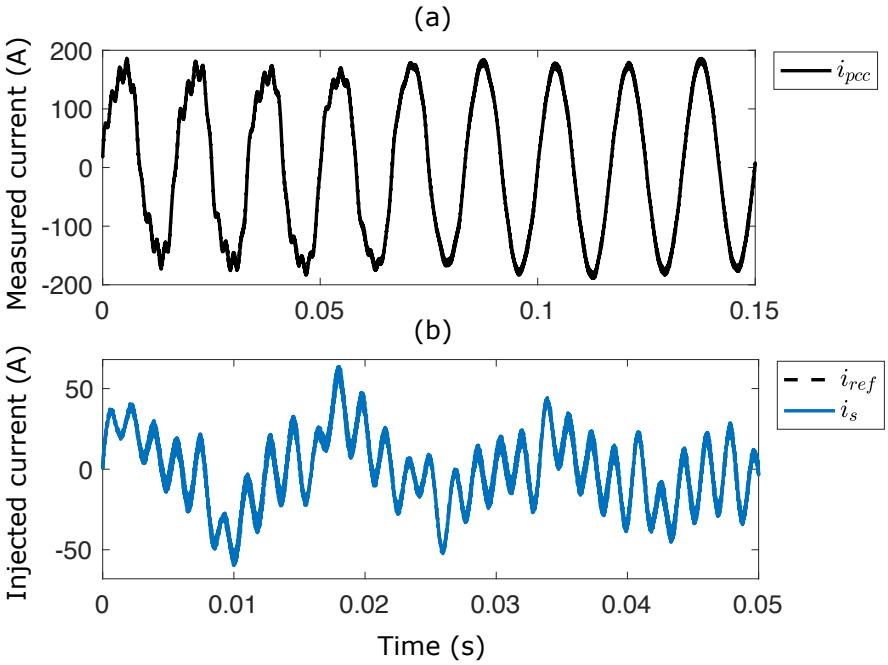

Figure 4.44: (a) Current waveform compensation at the PCC; (b) nonlinear optimal tracking control of the required injected current.

Figure 4.44(a) depicts the harmonic waveform compensation through the proposed scheme within a time interval of less than $0.1s$. Also, in Figure 4.44 (b) is depicted the effectiveness of the nonlinear optimal tracking control for the output current of the DC/AC inverter i_s tracking the required current profile i_{ref} for the harmonic compensation. In addition, Figure 4.45 shows the total harmonic distortion (THD) before and after the compensation with the proposed method with an initial THD = 24.79% and a compensated signal with a THD = 1.77% which represents a considerable reduction of the waveform distortion, which allows compliance with standards or grid codes [std, 1993], [I.E. Commission, 1998].

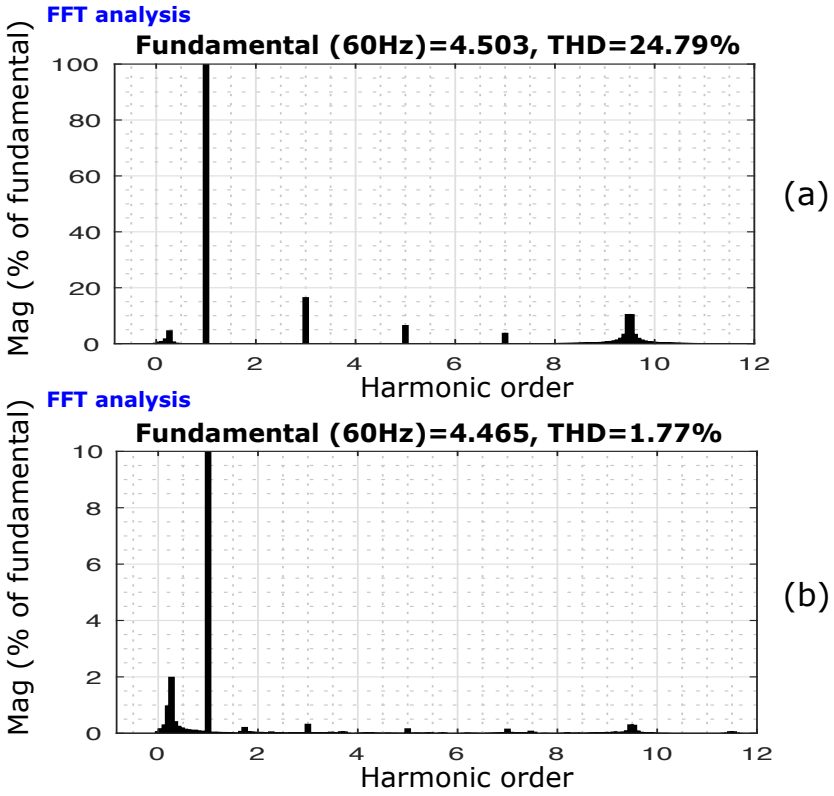

Figure 4.45: (a) Current waveform THD before compensation; (b) current THD after compensation.

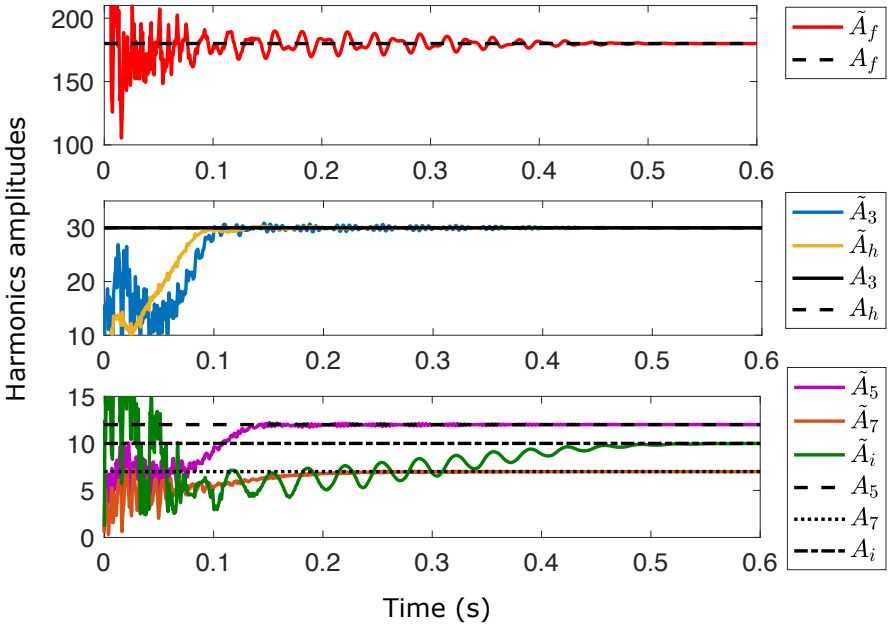

Figure 4.47: Estimated harmonics amplitudes.

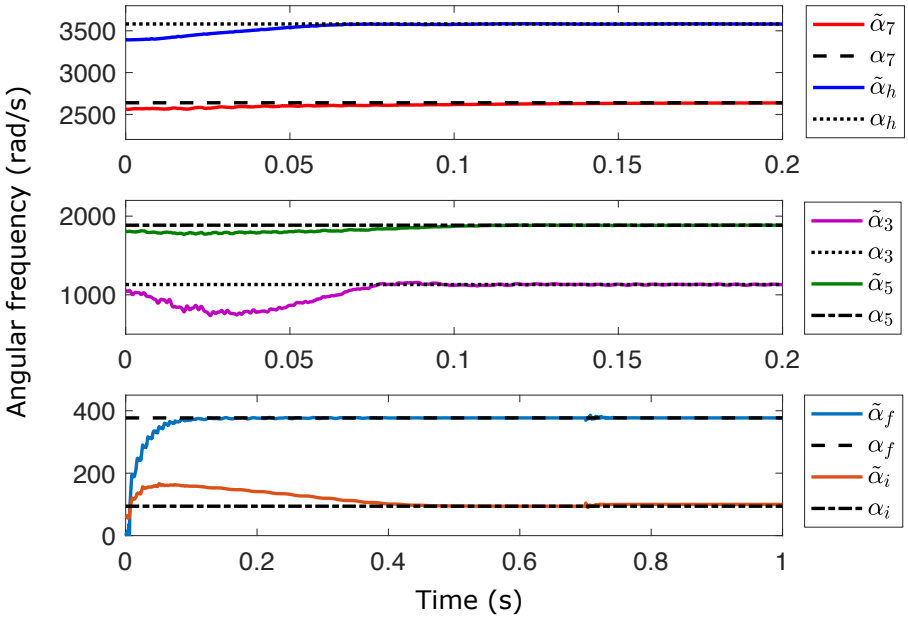

Figure 4.46: Estimated harmonic frequencies.

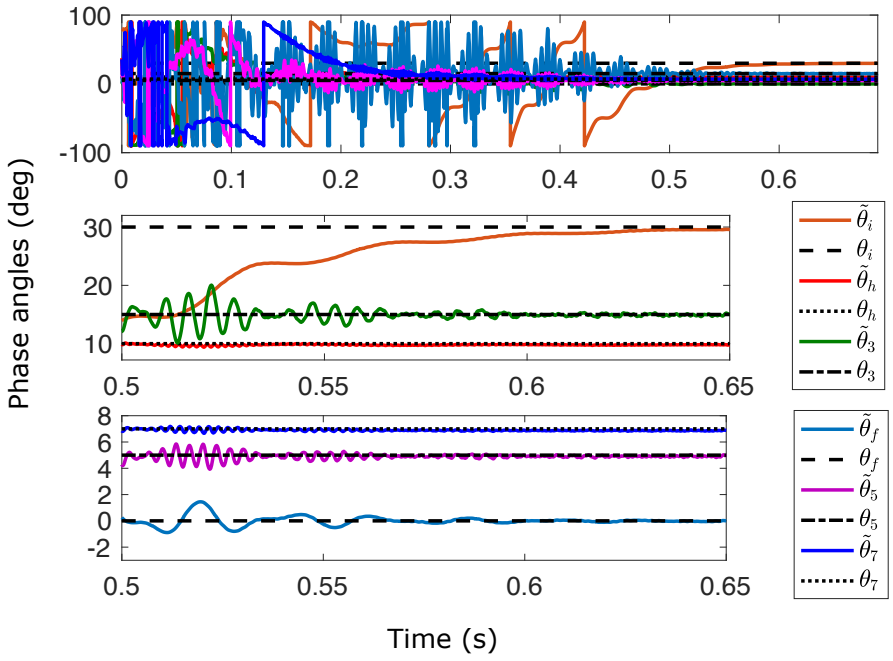

Figure 4.48: Phase angles estimation.

Figure 4.46 depicts the frequency estimation of the harmonic content of the distorted current signal demonstrating a fast convergence toward the following harmonic frequencies: $\alpha_1 = 15 \times 2 \times \pi$, $\alpha_h = 9.5 \times 2 \times \pi$, while $\alpha_f = 2 \times \pi \times 60$, $\alpha_3 = 6 \times \pi \times 60$, $\alpha_5 = 10 \times \pi \times 60$, and $a_7 = 14 \times \pi \times 60$, all in rad/s.

The results given in Figure 4.47, show the harmonics amplitudes estimation toward

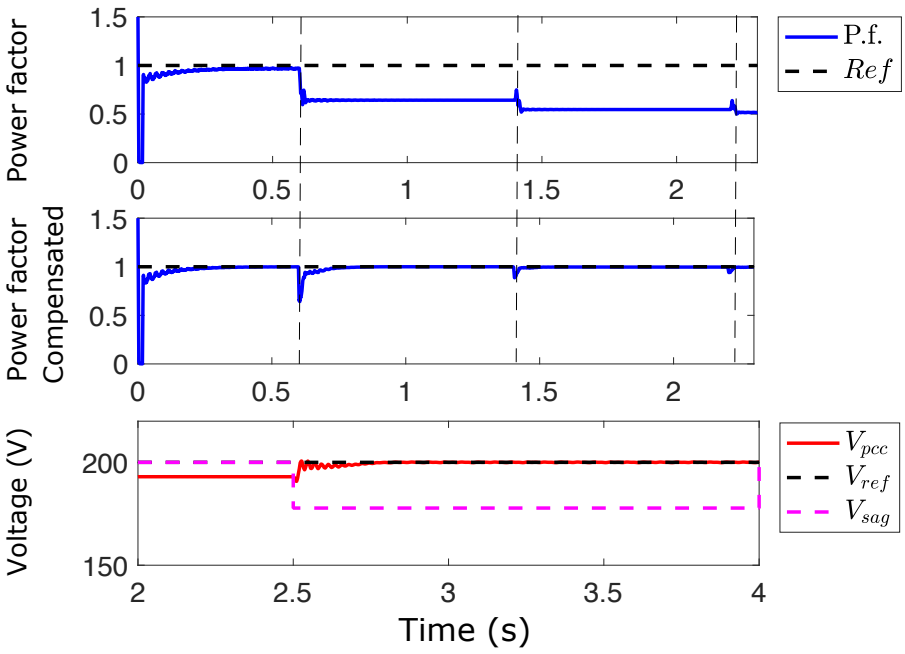

Figure 4.49: Power factor compensation (upper), and voltage regulation at the PCC (lower).

$\tilde{A}_i = 10$, $\tilde{A}_h = 30$, $\tilde{A}_f = 180$, $\tilde{A}_3 = 30$, $\tilde{A}_5 = 12$ and $\tilde{A}_7 = 7$. It is important to mention that the estimator exhibits a fast convergence for all the harmonic amplitudes, but the interharmonic which has the slowest convergence rate. Nonetheless, it is possible to appreciate that the proposed estimator can estimate interharmonic amplitude. A faster interharmonic convergence is a topic for a future work.

Figure 4.48 shows the harmonic phases estimation where the following results were obtained $\theta_i = 30$, $\theta_h = 10$, $\theta_f = 0$, $\theta_3 = 15$, $\theta_5 = 5$ and $\theta_7 = 7$, all in deg units.

Figure 4.50 depicts the voltage waveform measured at the PCC during harmonics compensation, power factor correction and voltage regulation respectively. Finally, Figure 4.49 (upper) shows the power factor regulation without the proposed control scheme and with the compensation scheme, where it is possible to appreciate the unitary power factor regulation in the presence of abrupt load changes. Finally, Figure 4.49 (lower) demonstrates the voltage regulation at the PCC in the presence of voltage variation. The results above demonstrate that through the proposed control scheme at different time instances, it is possible to compensate the power quality issues presented at the power system node.

It is important to mention that, for simulation purposes, the selection of the controller necessary to compensate each of the power quality problems was made through the selection of the parameter Λ shown in Table 4.4. However, the Λ function must come

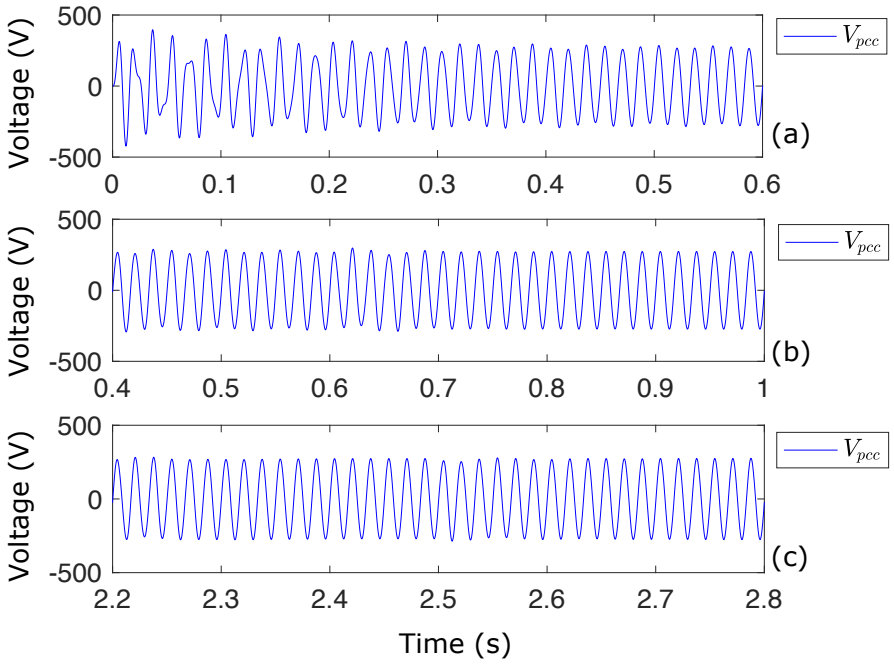

Figure 4.50: (a) Measured voltage at the PCC during harmonics compensations; (b) measured voltage during power factor corrections; (c) measured voltage during voltage regulation

from a higher hierarchical control level capable of automating the decision-making process and selecting which power quality problem to be solved as a priority. However, the design of this hierarchical level of control is proposed as a future work derived from this thesis.

4.5 Summary

This Chapter ascertains control strategies to provide ancillary services to a microgrid in harmonic suppression, power factor correction, and voltage regulation. The control objectives are achieved through a nested nonlinear robust control scheme based on nonlinear optimal control combined with sliding modes. In addition, a holistic solution for power quality enhancement is presented, related to the harmonic suppression scheme, a fast convergent harmonic and interharmonics estimator is presented, relying on a decentralized approach. In addition, the power quality enhancement control scheme's effectiveness through microgrid ancillary services is demonstrated via simulations.

Chapter 5

Conclusions and Future Work

5.1 Conclusions

This thesis has presented the design of nonlinear optimal and robust controllers for both microgrid operative modes and power conditioning applications mainly based on nonlinear optimal tracking control and super-twisting sliding modes. Case of study simulation results have demonstrated the effectiveness of the proposed control schemes applied for power electronic converters. Derived from the work of this thesis, the following has been concluded: a) the use of nonlinear optimal control for the primary control of microgrids in their different modes of operation has allowed the control of the variables of frequency, voltage, and power in an effective way, improving the results offered by linear controllers such as PID-type controls; b) the proposed energy storage scheme based on supercapacitors has been considered as a design block that can be integrated into different microgrid elements such as those proposed in this thesis to deal with the power generation intermittency produced by renewable energy sources or to provide ancillary services to the electrical grid in terms of power conditioning; c) The proposed harmonic identification scheme based on a decentralized structure has proved to be efficient for real-time implementation, which makes it feasible for feedback control applications such as dynamic harmonic suppression in conjunction with control strategies such as nonlinear optimal control; d) in this thesis, a novel control scheme based on nonlinear optimal control in combination with sliding modes has been presented. This control scheme has allowed to control variables of complex coupled dynamic systems such as power factor and voltage regulation in a power node of the electrical power grid through electronic power converters; e) the power conditioning strategies described in this thesis have been integrated into the same control scheme by acting on a single power electronic converter capable of compensating for different problems in terms of power quality depending on the power grid requirements.

The contributions of this thesis have been:

- The design of a nonlinear optimal controller for an energy storage unit based on

supercapacitors considering a proper charging strategy along with an intelligent controller.

- The design of a power conditioning scheme based on an online fast-convergent harmonic estimator with a decentralized structure. Which, along with a nonlinear optimal tracking controller for a power electronic converter, is capable of mitigating the harmonic waveform distortion in a power system node.
- The design of a controller for power conditioning applications. Capable of compensating for voltage deviations and power factor correction. The controller is based on nonlinear optimal tracking control and sliding mode super-twisting controller within a nested control structure capable of rejecting structural and parametric model uncertainties and external disturbances.

5.2 Future work

The results shown in this thesis aim to lay the foundations for future research in nonlinear control of microgrids, harmonics estimation, and power conditioning applications. In this sense, the following activities are proposed as future work and research.

- Concerning the nonlinear control of microgrids, it is proposed to integrate different distributed generation nodes considering a superior hierarchical control level, such as their coordination to share electrical power between different parallel converters and the power flow optimization. In addition, it is proposed to perform real-time experiments for an energy storage system based on supercapacitors.
- Laboratory tests of the nonlinear optimal controller applied for harmonic suppression, as described in Chapter 4, are possible to perform. However, for this thesis, this topic is considered to be a future work since, at the time this thesis was written, the Laboratory did not have the required equipment to perform the complete HIL setup. Nonetheless, within this thesis, it is demonstrated that through a HIL experiment, by using a low-cost microcontroller, it is possible the implementation of the harmonic estimator, which is the element that demands a more significant computational effort than the control algorithm.
- In Chapter 4 of this thesis, a control scheme capable of providing ancillary services to the electrical power grid in terms of harmonic compensation, power factor correction, and voltage regulation with a holistic approach is presented. However, as future work, it is proposed to design a control scheme with a higher intelligent control layer capable of making decisions depending on which power quality problem should be prioritized to solve, depending on various parameters of the power grid or energy efficiency.

- The design of harmonic estimators based on sliding modes is proposed in such a way as to be able to compare the performance of the identification scheme presented in this thesis against the proposed strategy. It is proposed that the estimator might be able to identify the amplitude, phase, and frequency of electrical waveforms but with the particularity of not considering the frequency as constant but considering fast frequency variations, since the harmonic estimation problem can not only be applied to electrical power systems but also to other areas of interest for feedback control systems.

Appendix A

Proof of Theorem 1

Consider the Hamiltonian function as

$$\mathcal{H}(x,u,t) = \frac{1}{2}e^T Q e + \frac{1}{2}u^T R u + \frac{\partial V(x,t)^T}{\partial x}\left[A(x)x + B(x)u\right] \tag{A.1}$$

where $V(x,t)$ is the optimal value function. The Hamiltonian is used to obtain the control law u by applying the maximum principle condition

$$\frac{\partial \mathcal{H}(x,u)}{\partial u} = Ru + B^T(x)\frac{\partial V(x,t)}{\partial x} = 0 \tag{A.2}$$

then the optimal control law results in

$$u^*(x) = -R^{-1}(t)B^T(x)\frac{\partial V(x,t)}{\partial x} \tag{A.3}$$

for the optimal control solution based on (A.1) and (A.3), the following Hamilton-Jacobi-Bellman equation must be fulfilled

$$\begin{aligned} 0 =& \frac{\partial V(x,t)}{\partial t} + \mathcal{H}(x,u^*,t) \\ =& \frac{\partial V(x,t)}{\partial t} + \frac{1}{2}e^T Q e + \frac{1}{2}u^{*T}(x) R u^*(x) + \frac{\partial V(x,t)^T}{\partial x}\left[A(x)x + B(x)u^*(x)\right] \\ =& \frac{\partial V(x,t)}{\partial t} + \frac{1}{2}r^T Q r - r^T Q C(x)x + \frac{1}{2}x^T C^T(x) Q C(x)x - \frac{1}{2}\frac{\partial V(x,t)^T}{\partial x}B(x) \\ & \times R^{-1}B^T(x)\frac{\partial V(x,t)}{\partial x} + \frac{\partial V(x,t)^T}{\partial x}A(x)x. \end{aligned} \tag{A.4}$$

Searching for a solution such that (A.4) is satisfied; $V(x,t)$ is proposed as

$$V(x,t) = \frac{1}{2}x^T P x - z^T x + \varphi, \qquad P = P^T > 0. \tag{A.5}$$

Therefore

$$\frac{\partial V(x,t)}{\partial t} = \frac{1}{2}x^T \dot{P} x - \dot{z}^T x + \dot{\varphi} \qquad \text{and} \qquad \frac{\partial V(x,t)}{\partial x} = Px - z. \tag{A.6}$$

Then, the HJB equation becomes

$$\begin{aligned}
0 =& \frac{1}{2}x^T\dot{P}x - \dot{z}^T x + \dot{\varphi} + \frac{1}{2}r^T Q r - r^T Q C(x)x + \frac{1}{2}x^T C^T(x)QC(x)x \\
& - \frac{1}{2}\left(Px - z\right)^T B(x)R^{-1}B^T(x)(Px - z) + \left(Px - z\right)^T A(x)x \\
=& \frac{1}{2}x^T\left[\dot{P} + C^T(x)QC(x) - PB(x)R^{-1}B^T(x)P + A^T(x)P + PA(x)\right]x \\
& - \left[\dot{z}^T + r^T QC(x) + z^T\left(A(x) - B(x)R^{-1}B^T(x)P\right)\right]x + \dot{\varphi} + \frac{1}{2}r^T Q r \\
& - \frac{1}{2}z^T(x)B(x)R^{-1}B^T(x)z.
\end{aligned} \tag{A.7}$$

The dynamic behavior of the optimal closed-loop-tracking system

$$\dot{x} = \left[A(x) - B(x)R^{-1}B^T(x)P\right]x + B(x)R^{-1}B^T z \tag{A.8}$$

can be analyzed as a dynamical system with a forcing function z. Hence due to the fact that (2.13) does not depend on the solution of z, the stability analysis for the nominal system

$$\dot{x} = \left[A(x) - B(x)R^{-1}B^T(x)P\right]x \tag{A.9}$$

can be established as follows: Assuming controllability and observability for system (2.9), there exists a differentiable symmetric and positive definite matrix P as a solution of (2.13). Considering the positive definite and radially unbounded candidate Lyapunov function $W = x^T Px$ and taking the time derivate for W along the nominal system, results in

$$\begin{aligned}
\dot{W} &= x^T\dot{P}x + x^T P\dot{x} \\
&= x^T\dot{P}x + x^T\left[PA(x) + A^T(x)P - 2PB(x)R^{-1}B^T(x)P\right]x
\end{aligned} \tag{A.10}$$

From (2.13) consider that

$$PA(x) + A^T(x)P = -\dot{P} - C^T(x)QC(x) + PB(x)R^{-1}B^T(x)P \tag{A.11}$$

Then (A.11) becomes

$$\begin{aligned}
\dot{W} &= x^T\dot{P}x + x^T\left[-\dot{P} - C^T(x)QC(x) - PB(x)R^{-1}B^T(x)P\right]x \\
&= -x^T\left[C^T(x)QC(x) + PB(x)R^{-1}B^T(x)P\right]x
\end{aligned} \tag{A.12}$$

Therefore, $\dot{W}$ is negative semidefinte. Since the pair $[A(x), C(x)]$ is observable and by LaSalle's theorem, asymptotic stability for the nominal system is ensured. □

Appendix B

Proof of Theorem 2

The estimator stability is based on the analysis of interconnected systems, as exposed in [Khalil, 2002]. To this end, let us consider that the n-th sub-system associated with the generation of the n-signal is described by

$$\begin{aligned} \dot{z}_{n1} &= \lambda_n z_{n2} \\ \dot{z}_{n2} &= -\frac{z_{n3}}{\lambda_n} z_{n1} \\ \dot{z}_{n3} &= 0 \\ s_n &= \frac{k_{n1}}{\lambda_n} z_{n1} + k_{n2} z_{n2}. \end{aligned} \tag{B.1}$$

Then, the corresponding state estimator structure for (B.1) is defined as

$$\begin{aligned} \dot{\hat{z}}_{n1} &= \lambda_n \hat{z}_{n2} + \frac{\lambda_n}{k_{n2}}(s_n - \hat{s}_n) \\ \dot{\hat{z}}_{n2} &= -\frac{\hat{z}_{n3}}{\lambda_n}\hat{z}_{n1} + \xi(s_n - \hat{s}_n) \\ \dot{\hat{z}}_{n3} &= -\gamma_n \hat{z}_{n1}(s_n - \hat{s}_n) \\ \hat{s}_n &= \frac{k_{n1}}{\lambda_n}\hat{z}_{n1} + k_{n2}\hat{z}_{n2}. \end{aligned} \tag{B.2}$$

By defining the estimator error variables as $e_{n1} = z_{n1} - \hat{z}_{n1}$, $e_{n2} = z_{n2} - \hat{z}_{n2}$ and $e_{n3} = z_{n3} - \hat{z}_{n3}$, thus $e_n = [e_{n1} \;\; e_{n2} \;\; e_{n3}]^T$, then their corresponding time derivatives become

$$\dot{e}_{n1} = \lambda_n e_{n2} - \frac{\lambda_n}{k_{n2}}\left(\frac{k_{n1}}{\lambda_n} e_{n1} + k_{n2} e_{n2}\right) \tag{B.3}$$

$$\begin{aligned}\dot{e}_{n2} = &-\left(\frac{z_{n3}}{\lambda_n}+\frac{\xi_n k_{n1}}{\lambda_n}\right)e_{n1}-\xi_n k_{n2}e_{n2}+\frac{z_{n3}}{\lambda_n}\hat{z}_{n1}\\ &-\frac{\hat{z}_{n1}e_{n3}}{\lambda_n}-\frac{z_{n3}}{\lambda_n}\hat{z}_{n1}\end{aligned} \tag{B.4}$$

$$\dot{e}_{n3} = \dot{z}_{n3}+\gamma_n\hat{z}_{n1}\left(\frac{k_{n1}}{\lambda_{n1}}e_{n1}+k_{n2}e_{n2}\right). \tag{B.5}$$

Therefore, the n-th error dynamics becomes

$$\dot{e}_{n1} = -\frac{k_{n1}}{k_{n2}}e_{n1} \tag{B.6a}$$

$$\dot{e}_{n2} = -\frac{1}{\lambda_n}(\alpha_n+\xi_n k_{n1})e_{n1}-\xi_n k_{n2}e_{n2}-\frac{\hat{z}_{n1}}{\lambda_n}e_{n3} \tag{B.6b}$$

$$\dot{e}_{n3} = \gamma_n\frac{k_{n1}}{\lambda_n}\hat{z}_{n1}e_{n1}+\gamma_n k_{n2}\hat{z}_{n1}e_{n2}. \tag{B.6c}$$

Consider the candidate Lyapunov function to establish the asymptotic stability to the origin of (B.6), as

$$V_n(e_n) = \frac{1}{2}\Big(e_{n1}^2+\lambda_n^2\,k_{n2}\,e_{n2}^2+\frac{\lambda_n}{\gamma_n}e_{n3}^2\Big). \tag{B.7}$$

From (B.6a), with positive constants k_{n1} and k_{n2}, it is immediate to see that $e_{n1}\to 0$ as $t\to\infty$, then by taking this fact in (B.6b)–(B.6c), the time derivative of (B.7) becomes

$$\begin{aligned}\dot{V}_n(e_n) = &-\frac{k_{n1}}{k_{n2}}e_{n1}^2+\lambda_n^2 k_{n2}e_{n2}\left(-\xi_n k_{n2}e_{n2}-\frac{\hat{z}_{n1}}{\lambda_n}e_{n3}\right)\\ &+\frac{\gamma_n}{\lambda_n}e_{n3}\left(\gamma_n k_{n2}\hat{z}_{n1}e_{n2}\right)\\ = &-\frac{k_{n1}}{k_{n2}}e_{n1}^2-\lambda_n^2 k_{n2}^2\xi_n e_{n2}^2.\end{aligned} \tag{B.8}$$

Therefore, $\dot{V}_n(e_n)$ is negative semidefinite, and by using the LaSalle's theorem [Khalil, 2002], function $\dot{V}_n(e_n)=0$ for $e_{n1}=0$ and $e_{n2}=0$, consequently $\dot{e}_{n2}=0$ and $\dot{e}_{n2}=0$, and from (B.6b) it follows that $0=-\dfrac{\hat{z}_{n1}}{\lambda_n}e_{n3}$, then the trivial solution $e_{n3}=0$ is fulfilled. Hence, the estimation error (B.6) is asymptotically stable [Khalil, 2002]. Recognize that (B.6) can be rewritten as

$$\dot{e}_n = \underbrace{\begin{bmatrix} -\frac{k_{n1}}{k_{n2}} & 0 & 0\\ -\frac{1}{\lambda_n}(z_{n3}+\xi_n k_{n1}) & -\xi_n k_{n2} & -\frac{\hat{z}_{n1}}{\lambda_n}\\ \gamma_n\frac{k_{n1}}{\lambda_n}\hat{z}_{n1} & \gamma_n k_{n2}\hat{z}_{n1} & 0\end{bmatrix}}_{\mathcal{A}_1(z_{n3},\hat{z}_{n1})}\begin{bmatrix}e_{n1}\\ e_{n2}\\ e_{n3}\end{bmatrix} \tag{B.9a}$$

$$= \mathcal{A}_n(z_{n3},\hat{z}_{n1})e_n. \tag{B.9b}$$

Because the asymptotic stability of system (B.6) has been demonstrated through (B.7),

it is assumed that there exists a positive definite Lyapunov function of the form $V(e_n)$ such that its time derivative can be represented as $\dot{V}(e_n) = -\eta_n \|e_n\|^2$, where η_n becomes a stability degree [Khalil, 2002], defining its amount of negativeness.

Then the estimator stability analysis can be extended to the case when n signals (harmonics and inter-harmonics) are involved in a signal $s(t)$. In this case, the interconnection terms appear in the analysis by considering that a signal $s = \sum_{n=1}^{N} s_n = \sum_{n=1}^{N} \left(\frac{k_{n1}}{\lambda_n} z_{n1} + k_{n2} z_{n2} \right)$. Particularly, for the error e_1 one obtains the interconnection described as

$$\begin{aligned}
\dot{e}_{11} &= -\frac{k_{11}}{k_{12}} e_{11} + b_{11} e \\
\dot{e}_{12} &= -\frac{1}{\lambda_1} \left(z_{13} + \xi_1 k_{11} \right) e_{11} - \xi_1 k_{12} e_{12} - \frac{\hat{z}_{11}}{\lambda_1} e_{13} + b_{12} e \\
\dot{e}_{13} &= \gamma_1 \frac{k_{11}}{\lambda_1} \hat{z}_{11} e_{11} + \gamma_1 k_{12} \hat{z}_{11} e_{12} + b_{13} e.
\end{aligned} \tag{B.10}$$

where

$$\begin{aligned}
b_{11} &= \left[0, 0, 0, -\frac{\lambda_1}{\lambda_2} \frac{k_{22}}{k_{12}}, 0, \ldots, \frac{\lambda_1}{\lambda_n} \frac{k_{n1}}{k_{12}}, -\lambda_1 \frac{k_{n1}}{k_{12}}, 0 \right] \\
b_{12} &= \left[0, 0, 0, -\xi_1 \frac{k_{21}}{\lambda_2}, -\xi k_{22}, 0, \ldots, -\xi_1 \frac{k_{n1}}{\lambda_n}, -\xi_1 k_{n2}, 0 \right] \\
b_{13} &= \Big[0, 0, 0, \gamma_1 \hat{z}_{11} \frac{k_{21}}{\lambda_2}, \gamma_1 \hat{z}_{11} k_{22}, 0, \ldots, \\
&\quad \gamma_1 \hat{z}_{11} \frac{k_{n1}}{\lambda_n}, \gamma_1 \hat{z}_{11} k_{n2}, 0 \Big]
\end{aligned}$$

Notice that system (B.10) can be rewritten into a compact form as

$$\dot{e}_1 = \mathcal{A}_1(z_1, \hat{z}_1) e_1 + b_1 e \tag{B.11}$$

where

$$\mathcal{A}_1(z_1,\, \hat{z}_1) = \begin{bmatrix} -\frac{k_{11}}{k_{12}} & 0 & 0 \\ -\frac{1}{\lambda_1} \left(z_{13} + \xi_1 k_{11} \right) & -\xi_1 k_{12} & -\frac{\hat{z}_{11}}{\lambda_1} \\ \gamma_1 \frac{k_{11}}{\lambda_1} \hat{z}_{11} & \gamma_1 k_{12} \hat{z}_{11} & 0 \end{bmatrix}$$

$$b_1 = [b_{11} \;\; b_{12} \;\; b_{13}]^T$$

with $e_1 = [e_{11} \;\; e_{12} \;\; e_{13}]^T$ and $e = [e_{11} \;\; e_{12} \;\; e_{13} \;\; e_{21} \;\; e_{22} \;\; e_{23} \;\; \ldots \;\; e_{n1} \;\; e_{n2} \;\; e_{n3}]^T$. In a similar way, the error e_2 can be analyzed, resulting in

$$
\begin{aligned}
\dot{e}_{21} &= -\frac{k_{21}}{k_{22}} e_{11} + b_{21} e \\
\dot{e}_{22} &= -\frac{1}{\lambda_2}(z_{23} + \xi_2 k_{21}) e_{21} - \xi_2 k_{22} e_{22} - \frac{\hat{z}_{21}}{\lambda_2} e_{23} + b_{22} e \\
\dot{e}_{23} &= \gamma_2 \frac{k_{21}}{\lambda_2} \hat{z}_{21} e_{21} + \gamma_2 k_{22} \hat{z}_{21} e_{22} + b_{23} e.
\end{aligned} \tag{B.12}
$$

where

$$
\begin{aligned}
b_{21} =& \Big[-\frac{\lambda_2}{\lambda_1}\frac{k_{12}}{k_{22}}, -\lambda_2 \frac{k_{12}}{k_{22}}, 0, -\frac{\lambda_1}{\lambda_2}\frac{k_{21}}{k_{12}}, \lambda_1 \frac{k_{22}}{k_{12}}, 0, \\
& \ldots, -\frac{\lambda_2}{\lambda_n}\frac{k_{n1}}{k_{22}}, 0 \Big] \\
b_{22} =& \Big[-\xi_2 \frac{k_{11}}{\lambda_1}, -\xi_2 k_{12}, 0, -\xi_1 \frac{k_{21}}{\lambda_2}, \xi_1 k_{22}, 0, \ldots \\
& -\xi_1 \frac{k_{n1}}{\lambda_n}, -\xi_1 k_{n2}, 0 \Big] \\
b_{23} =& \Big[\gamma_2 \hat{z}_{21} \frac{k_{11}}{\lambda_1}, \gamma_2 \hat{z}_{21} k_{12}, 0, \gamma_1 \hat{z}_{11} \frac{k_{21}}{\lambda_2}, \gamma_1 \hat{z}_{11} k_{22}, 0, \ldots \\
& \gamma_2 \hat{z}_{21} \frac{k_{n3}}{\lambda_3}, \gamma_2 \hat{z}_{21} k_{n2}, 0 \Big]
\end{aligned}
$$

Therefore, generalizing for n harmonics, one can describe the whole estimation error system as

$$
\dot{e} = \mathcal{A}\, e + \mathcal{B}\, e \tag{B.13}
$$

where $\mathcal{A} = \text{diag}\{\mathcal{A}_1(z_1, \hat{z}_1), \mathcal{A}_2(z_2, \hat{z}_2), \ldots, \mathcal{A}_n(z_n, \hat{z}_n)\}$, $\mathcal{B} = [b_1, b_2, \ldots, b_n]^T$ and $e = [e_1, e_2, \ldots, e_n]^T$. Then it is possible to state the following general Lyapunov function

$$
V(e) = e^T P e, \qquad P = P^T > 0 \tag{B.14}
$$

with time derivative

$$
\dot{V}(e) = \dot{e}^T P e + e^T P \dot{e} \tag{B.15}
$$

which can be described in terms of its nominal part (already demonstrated to be asymptotically stable through (B.7)–(B.8) for an n estimator, with stability degree given as η_n), and now with the inclusion of the interconnection part as

$$
\begin{aligned}
\dot{V}(e) &\leq e^T (A^T P + P A) e + 2 \|P\| \|\mathcal{B}\| \|e_n\|^2 && \text{(B.16a)} \\
&\leq -\eta_P \|e_n\|^2 + 2 \|P\| \|\mathcal{B}\| \|e_n\|^2 && \text{(B.16b)} \\
&\leq -\left(\eta_P - 2 \|P\| \|\mathcal{B}\|\right) \|e_n\|^2 && \text{(B.16c)}
\end{aligned}
$$

where η_P is the general stability degree for the nominal part. Hence, if $\eta_P > 2 \|P\| \|\mathcal{B}\| \implies \dot{V}(e) < 0$, then the error motion in (B.13) is asymptotically stable. □

Appendix C

Estimator Gains

Table C.1: Estimator gains for phase A

Phase A	h_f	h_i	h_h	h_3	h_5	h_7
λ	5000	400	1×10^5	1×10^6	8×10^5	8×10^5
γ	2×10^5	7×10^5	5×10^5	1×10^6	8×10^5	8×10^5
ξ	1×10^5	1×10^5	10000	10000	17000	17000
k_1	1000	10	10000	12000	5000	5000
k_2	5	0.9	1	1	1	1

Table C.2: Estimator gains for phase B

Phase B	h_f	h_i	h_h	h_3	h_5	h_7
λ	5000	–	1×10^6	1×10^6	–	–
γ	2×10^5	–	5×10^5	1×10^5	–	–
ξ	2×10^5	–	10000	10000	–	–
k_1	200	–	10000	12000	–	–
k_2	5	–	1	1	–	–

Table C.3: Estimator gains for phase C

Phase C	h_f	h_i	h_h	h_3	h_5	h_7
λ	5000	400	1×10^6	1×10^6	–	8×10^5
γ	2×10^5	7×10^5	1×10^4	10000	–	8×10^5
ξ	2×10^5	1×10^5	5×10^5	1×10^6	–	17000
k_1	20	10	10000	12000	–	5000
k_2	5	0.9	1	1	–	1

Estimator Parameter Selection Guidance

- λ Weights the rising time, improving the tendency to the estimated variable.
- γ Weights the convergence to the estimated frequency.
- ξ A larger value improves the tendency to the estimated variable.
- k_1 Improves the tendency to the estimated variable. However, its value must be smaller than those selected for λ and γ.
- k_2 Weights the amplitude of the oscillations in the estimate of the variable in steady state.

Also, optimization techniques based on artificial intelligence, such as PSO [Mercangoz, 2021], could be applied to compute the optimal parameters of the estimator. However, it would require a more considerable computational effort for real-time implementations.

Bibliography

[std, 1993] (1993). *IEEE Recommended Practices and Requirements for Harmonic Control in Electrical Power Systems*. IEEE Std 519-1992.

[619, 2012] (2012). Ieee guide for application of power electronics for power quality improvement on distribution systems rated 1 kv through 38 kv. *IEEE Std 1409-2012*, pages 1–90.

[CHI, 2013] (2013). Temperature and state-of-charge estimation in ultracapacitors based on extended kalman filter. *Journal of Power Sources*, 234:234–243.

[853, 2018] (2018). Ieee guide for identifying and improving voltage quality in power systems. *IEEE Std 1250-2018 (Revision of IEEE Std 1250-2011)*, pages 1–0.

[lit, 2018] (2018). Ieee guide for the characterization and evaluation of lithium-based batteries in stationary applications. *IEEE Std 1679.1-2017*, pages 1–47.

[ESM, 2022] (2022). A system dynamics approach to study the long-term interaction of the natural gas market and electricity market comprising high penetration of renewable energy resources. *International Journal of Electrical Power Energy Systems*, 139:108021.

[Aamir et al., 2019] Aamir, A., Qiao, L., Guo, C., Rehman, A. U., and Yang, Z. (2019). Impact of synchronous condenser on the dynamic behavior of lcc-based uhvdc system hierarchically connected to ac system. *CSEE Journal of Power and Energy Systems*, 5(2):190–198.

[Ahshan et al., 2020] Ahshan, R., Saleh, S. A., and Al-Badi, A. (2020). Performance analysis of a dq power flow-based energy storage control system for microgrid applications. *IEEE Access*, 8:178706–178721.

[Akagi, 2007] Akagi, H. (2007). *Instantaneous power theory and applications to power conditioning*. Wiley IEEE Press, Hoboken, N.J. Piscataway, USA.

[Alexander, 2017] Alexander, C. (2017). *Fundamentals of electric circuits*. McGraw-hill Education, New York, NY,USA.

[Alizadeh et al., 2016] Alizadeh, S. M., Ozansoy, C., and Alpcan, T. (2016). The impact of x/r ratio on voltage stability in a distribution network penetrated by wind farms. In *2016 Australasian Universities Power Engineering Conference (AUPEC)*, pages 1–6.

[Anderson and Moore, 1990] Anderson, B. and Moore, J. (1990). *Optimal Control: Linear Quadratic Methods*. Prentice-Hall, Englewood Cliffs, NJ, USA.

[Annaswamy and Amin, 2013] Annaswamy, A. M. and Amin, M. (2013). Ieee vision for smart grid controls: 2030 and beyond. *IEEE Vision for Smart Grid Controls: 2030 and Beyond*, pages 1–168.

[Arrillaga and Watson, 2004] Arrillaga, J. and Watson, N. (2004). *Power Systems Harmonics*. Wiley, West Sussex PO19 8SQ, England.

[Astrom, 2006] Astrom (2006). *Introduction to stochastic control theory*. Dover Publications, Mineola, N.Y, USA.

[Athans, 2007] Athans, M. (2007). *Optimal control : an introduction to the theory and its applications*. Dover Publications, New York, USA.

[Bakke, 2017] Bakke, G. (2017). *The grid : the fraying wires between Americans and our energy future*. Bloomsbury, New York, NY.

[Bertsekas, 2005] Bertsekas, D. (2005). *Dynamic programming and optimal control*. Athena Scientific, Belmont, Massachusetts, USA.

[Bidram et al., 2017] Bidram, A., Nasirian, V., Davoudi, A., and Lewis, F. (2017). *Cooperative Synchronization in Distributed Microgrid Control*. Springer, Arlington, TX, USA.

[Can and Sayan, 2018] Can, E. and Sayan, H. H. (2018). A novel sspwm controlling inverter running nonlinear device. *Electrical Engineering*, 100(1):39–46.

[Carlson, 2015] Carlson, W. (2015). *Tesla inventor de la era eléctrica*. Crítica, México.

[Carnevale and Astolfi, 2011] Carnevale, D. and Astolfi, A. (2011). A hybrid observer for frequency estimation of saturated multi-frequency signals. In *2011 50th IEEE Conference on Decision and Control and European Control Conference*, Orlando, Florida, USA.

[Chen, 2013] Chen (2013). *Linear system theory and design*. Oxford University Press, New York.

[Chen et al., 2018] Chen, B., Pin, G., Ng, W. M., Li, P., Parisini, T., and Hui, S.-Y. R. (2018). Online detection of fundamental and interharmonics in ac mains for parallel operation of multiple grid-connected power converters. *IEEE Transactions on Power Electronics*, 33(11):9318–9330.

[Chen and Fei, 2019] Chen, Y. and Fei, J. (2019). Dynamic sliding mode control of active power filter with integral switching gain. *IEEE Access*, 7:21635–21644.

[Chun et al., 2018] Chun, T.-W., Kim, H.-G., and Nho, E.-C. (2018). Charging and discharging strategies of grid-connected super-capacitor energy storage systems. In *2018 IEEE International Conference on Industrial Technology (ICIT)*, pages 1743–1747.

[Cloutier, 1997] Cloutier, J. R. (1997). State-dependent riccati equation techniques: an overview. In *Proceedings of the 1997 American Control Conference*, volume 2, pages 932–936 vol.2, Albuquerque, New Mexico, USA.

[Cornea et al., 2017] Cornea, O., Andreescu, G., Muntean, N., and Hulea, D. (2017). Bidirectional power flow control in a dc microgrid through a switched-capacitor cell hybrid dc-dc converter. *IEEE Transactions on Industrial Electronics*, 64(4):3012–3022.

[Dash and Ray, 2018] Dash, S. K. and Ray, P. K. (2018). Power quality improvement utilizing pv fed unified power quality conditioner based on uv-pi and pr-r controller. *CPSS Transactions on Power Electronics and Applications*, 3(3):243–253.

[Díaz-González et al., 2016] Díaz-González, F., Sumper, A., and Gomis-Bellmunt, O. (2016). *Energy Storage in Power Systems*. willey, West Sussex, United Kingdom.

[Dugan, 2012] Dugan, R. (2012). *Electrical power systems quality*. McGraw Hill, New York, USA.

[Elmetwaly et al., 2020] Elmetwaly, A. H., Eldesouky, A. A., and Sallam, A. A. (2020). An adaptive d-facts for power quality enhancement in an isolated microgrid. *IEEE Access*, 8:57923–57942.

[Fan, 2017] Fan, L. (2017). *Control and Dynamics in Power Systems and Microgrids*. CRC Press Taylor and Francis, Florida, USA.

[Fedele and Ferrise, 2014] Fedele, G. and Ferrise, A. (2014). A frequency-locked-loop filter for biased multi-sinusoidal estimation. *IEEE Transactions on Signal Processing*, 62(5):1125–1134.

[Ferrara, 2017] Ferrara, A. (2017). *Sliding mode control of vehicle dynamics*. Institution of Engineering and Technology, London, United Kingdom.

[Franklin et al., 2010] Franklin, G., Powell, J., and Emami-Naeini, A. (2010). *Feedback Control of Dynamic Systems*. Pearson, London, United Kingdom.

[Freeman, 1996] Freeman, R. (1996). *Robust Nonlinear Control Design : State-Space and Lyapunov Techniques*. Birkhauser Boston, Boston, MA.

[Fridman, 2014] Fridman, L. (2014). *Robust output LQ optimal control via integral sliding modes*. Birkhauser, New York, NY, USA.

[Gates, 2021] Gates, B. (2021). *How to avoid a climate disaster : the solutions we have and the breakthroughs we need*. Alfred A. Knopf, New York, USA.

[Geering, 2007] Geering, H. P. (2007). *Optimal control with engineering applications*. Springer, Berlin, Germany.

[Ghartemani, 2014] Ghartemani, M. (2014). *Enhanced phase-locked loop structures for power and energy applications*. John Wiley & Sons Inc, Hoboken, New Jersey, USA.

[Gonzalo et al., 2020] Gonzalo, G., Aguila, A., Gonzalez, D., and Ortiz, L. (2020). Optimum location and sizing of capacitor banks using volt var compensation in micro-grids. *IEEE Latin America Transactions*, 18(03):465–472.

[Grama, 2003] Grama, A. (2003). *Introduction to parallel computing.* Addison-Wesley, Harlow, England New York, USA.

[Grbovic et al., 2010] Grbovic, P. J., Delarue, P., Le Moigne, P., and Bartholomeus, P. (2010). A bidirectional three-level dc-dc converter for the ultracapacitor applications. *IEEE Transactions on Industrial Electronics*, 57(10):3415–3430.

[Hajimolahoseini et al., 2008] Hajimolahoseini, H., Taban, M. R., and Abutalebi, H. R. (2008). Improvement of extended kalman filter frequency tracker for nonstationary harmonic signals. In *2008 International Symposium on Telecommunications*, pages 592–597, Iran, Tehran.

[Hashmi et al., 2020] Hashmi, M. U., Deka, D., Busić, A., Pereira, L., and Backhaus, S. (2020). Arbitrage with power factor correction using energy storage. *IEEE Transactions on Power Systems*, 35(4):2693–2703.

[Hatziargyriou, 2014] Hatziargyriou, N. (2014). *Microgrid, Arquiterctures and Control.* Wiley, West Sussex, United Kingdom.

[Holmes, 2003] Holmes, D. (2003). *Pulse width modulation for power converters : principles and practice.* John Wiley, Hoboken, NJ.

[Housseini et al., 2018] Housseini, B., Okou, A. F., and Beguenane, R. (2018). Robust nonlinear controller design for on-grid/off-grid wind energy battery-storage system. *IEEE Transactions on Smart Grid*, 9(6):5588–5598.

[Huang et al., 2018] Huang, C., Wang, Z., Zhao, Z., Wang, L., Lai, C. S., and Wang, D. (2018). Robustness evaluation of extended and unscented kalman filter for battery state of charge estimation. *IEEE Access*, 6:27617–27628.

[Hwang and Liu, 2014] Hwang, J. K. and Liu, Y. (2014). Noise analysis of power system frequency estimated from angle difference of discrete fourier transform coefficient. *IEEE Transactions on Power Delivery*, 29(4):1533–1541.

[I.E. Commission, 1998] I.E. Commission (1998). *IEC 61000-3-2- Electromagnetic Compatibility (EMC)-Part 3-2: Limits-Limits for Harmonic Current Emissions.*

[Jamshidi, 2014] Jamshidi, M. (2014). *Advance trends in soft computing : proceedings of WCSC 2013, December 16-18, San Antonio, Texas, USA.* Springer, Cham.

[Karimi-Ghartemani et al., 2012] Karimi-Ghartemani, M., Khajehoddin, S. A., Jain, P. K., Bakhshai, A., and Mojiri, M. (2012). Addressing dc component in pll and notch filter algorithms. *IEEE Transactions on Power Electronics*, 27(1):78–86.

[Karimi-Ghartemani and Ziarani, 2004] Karimi-Ghartemani, M. and Ziarani, A. (2004). A nonlinear time-frequency analysis method. *IEEE Transactions on Signal Processing*, 52(6):1585–1595.

[Keyhani, 2019] Keyhani, A. (2019). *Design of smart power grid renewable energy systems.* Wiley, River Street, Hoboken, USA.

[Khalil, 2015] Khalil, H. (2015). *Nonlinear control*. Pearson, Boston, Massachusetts, USA.

[Khalil, 2002] Khalil, H. K. (2002). *Nonlinear systems*. Prentice Hall, Upper Saddle River, NJ, USA.

[Khan et al., 2018] Khan, A., Memon, S., and Sattar, T. P. (2018). Analyzing integrated renewable energy and smart-grid systems to improve voltage quality and harmonic distortion losses at electric-vehicle charging stations. *IEEE Access*, 6:26404–26415.

[Kim, 2017] Kim, S.-H. (2017). Chapter 7 - pulse width modulation inverters. In Kim, S.-H., editor, *Electric Motor Control*, pages 265–340. Elsevier.

[Kirk, 2004] Kirk, D. (2004). *Optimal Control Theory an Introduction*. Dover, Upper Saddle River, NJ, USA.

[Levant, 1993] Levant, A. (1993). Sliding order and sliding accuracy in sliding mode control. *International Journal of Control*, 58(6):1247–1263.

[Liu et al., 2018] Liu, K., Lu, J., and Lin, Z. (2018). Design of distributed observers in the presence of arbitrarily large communication delays. *IEEE Transactions on Neural Networks and Learning Systems*, 29(9):4447–4461.

[Lo et al., 2008] Lo, Y.-K., Lee, T.-P., and Wu, K.-H. (2008). Grid-connected photovoltaic system with power factor correction. *IEEE Transactions on Industrial Electronics*, 55(5):2224–2227.

[Madtharad and Premrudeepreechacharn, 2002] Madtharad, C. and Premrudeepreechacharn, S. (2002). Active power filter for three-phase four-wire electric systems using neural networks. *Electric Power Systems Research*, 60:179–192.

[Mahamad et al., 2004] Mahamad, N., Hadzer, C., and Masri, S. (2004). Application of lc filter in harmonics reduction. In *PECon 2004. Proceedings. National Power and Energy Conference, 2004.*, pages 268–271.

[Mahendran et al., 2017] Mahendran, S., Nagapavithra, S., and Umamaheswari, S. (2017). Fuzzy based power factor correction for bldc motor using hybrid inverter. In *2017 Conference on Emerging Devices and Smart Systems (ICEDSS)*, pages 286–290, Mallasamudram, Tiruchengode, India.

[Mallick, 2020] Mallick, P. (2020). *Electronic systems and intelligent computing : proceedings of ESIC 2020*. Springer, Singapore.

[Mercangoz, 2021] Mercangoz, B. (2021). *Applying particle swarm optimization : new solutions and cases for optimized portfolios*. Springe, Cham, Switzerland.

[Moghbel et al., 2018] Moghbel, M., Masoum, M. A. S., Fereidouni, A., and Deilami, S. (2018). Optimal sizing, siting and operation of custom power devices with statcom and aplc functions for real-time reactive power and network voltage quality control of smart grid. *IEEE Transactions on Smart Grid*, 9(6):5564–5575.

[Mohan, 2003] Mohan, N. (2003). *Power electronics : converters, applications, and design*. John Wiley & Sons, Hoboken, NJ, USA.

[Mojiri et al., 2010] Mojiri, M., Karimi-Ghartemani, M., and Bakhshai, A. (2010). Processing of harmonics and interharmonics using an adaptive notch filter. *IEEE Transactions on Power Delivery*, 25(2):534–542.

[Molla and Kuo, 2020] Molla, E. M. and Kuo, C.-C. (2020). Voltage sag enhancement of grid connected hybrid pv-wind power system using battery and smes based dynamic voltage restorer. *IEEE Access*, 8:130003–130013.

[Moreno and Osorio, 2008] Moreno, J. A. and Osorio, M. (2008). A lyapunov approach to second-order sliding mode controllers and observers. In *2008 47th IEEE Conference on Decision and Control*, pages 2856–2861, Cancún, México.

[Mujal, 2019] Mujal, R. (2019). *Cálculo de lineas y redes eléctricas*. Barcelona, España.

[Obregon-Pulido et al., 2002] Obregon-Pulido, G., Castillo-Toledo, B., and Loukianov, A. (2002). A globally convergent estimator for n-frequencies. *IEEE Transactions on Automatic Control*, 47(5):857–863.

[Olivares et al., 2014] Olivares, D. E., Mehrizi-Sani, A., Etemadi, A. H., Canizares, C. A., Iravani, R., Kazerani, M., Hajimiragha, A. H., Gomis-Bellmunt, O., Saeedifard, M., Palma-Behnke, R., Jimenez-Estevez, G. A., and Hatziargyriou, N. D. (2014). Trends in microgrid control. *IEEE Transactions on Smart Grid*, 5(4):1905–1919.

[Ornelas-Tellez et al., 2014] Ornelas-Tellez, F., Rico, J. J., and Ruiz-Cruz, R. (2014). Optimal tracking for state-dependent coefficient factorized nonlinear systems. *Asian Journal of Control*, 16(3):890–903.

[Ornelas-Tellez et al., 2018] Ornelas-Tellez, F., Rico-Melgoza, J., Espinosa-Juarez, E., and Sanchez, E. (2018). Robust control in dc microgrids. *IEEE Transactions on Smart Grid*, 9(6):5543–5553.

[Ornelas-Tellez et al., 2019] Ornelas-Tellez, F., Rico-Melgoza, J. J., Morfin-Magana, R., and Ramos-Paz, S. (2019). Optimal dynamic harmonic extraction and suppression in power conditioning applications. *IEEE Transactions on Industrial Electronics*, pages 1–12.

[Ornelas-Tellez et al., 2020] Ornelas-Tellez, F., Rico-Melgoza, J. J., Morfin-Magana, R., and Ramos-Paz, S. (2020). Optimal dynamic harmonic extraction and suppression in power conditioning applications. *IEEE Transactions on Industrial Electronics*, 67(9):7909–7918.

[Ornelas-Tellez et al., 2013] Ornelas-Tellez, F., Rico-Melgoza, J. J., and Sanchez, E. N. (2013). Optimal tracking for a class of nonlinear systems based on the state-dependent riccati equation. In *2013 10th International Conference on Electrical Engineering, Computing Science and Automatic Control (CCE)*, pages 42–47, México City, México.

[Pahlevaninezhad et al., 2012] Pahlevaninezhad, M., Das, P., Drobnik, J., Moschopoulos, G., Jain, P. K., and Bakhshai, A. (2012). A nonlinear optimal control approach based on the

control-lyapunov function for an ac/dc converter used in electric vehicles. *IEEE Transactions on Industrial Informatics*, 8(3):596–614.

[Perruquetti and Barbot, 2002] Perruquetti, W. and Barbot, J. (2002). *Sliding Mode Control in Engineering*. Marcel Dekker, New York, NY, USA.

[Pinto et al., 2013] Pinto, J. G., Monteiro, V., Goncalves, H., Exposto, B., Pedrosa, D., Couto, C., and Afonso, J. L. (2013). Bidirectional battery charger with grid-to-vehicle, vehicle-to-grid and vehicle-to-home technologies. In *IECON 2013 - 39th Annual Conference of the IEEE Industrial Electronics Society*, pages 5934–5939, Venn, Austria.

[Qin et al., 2019] Qin, S., Lei, Y., Ye, Z., Chou, D., and Pilawa-Podgurski, R. C. N. (2019). A high-power-density power factor correction front end based on seven-level flying capacitor multilevel converter. *IEEE Journal of Emerging and Selected Topics in Power Electronics*, 7(3):1883–1898.

[Rachid et al., 2017] Rachid, A., Fadil, H. E., Gaouzi, K., and Belhaj, F. Z. (2017). Output feedback control of bidirectional dc-dc power converter for bev charger. In *International Conference on Automation Control Engineering and Computer Science*, Hammamet, Tunisia.

[Radulović et al., 2020] Radulović, M., Zecević, Z., and Krstajić, B. (2020). Dynamic phasor estimation by symmetric taylor weighted least square filter. *IEEE Transactions on Power Delivery*, 35(2):828–836.

[Rameshkunar et al., 2017] Rameshkunar, K., Indragandhi, V., and Arunkumari, T. (2017). Model predictive current control of single phase shunt active power filter. *Energy Procedia*, 117:658–665.

[Ramos-Paz et al., 2017] Ramos-Paz, S., Ornelas-Tellez, F., and Loukianov, A. G. (2017). Nonlinear optimal tracking control in combination with sliding modes: Application to the pendubot. In *2017 IEEE International Autumn Meeting on Power, Electronics and Computing (ROPEC)*, pages 1–6.

[Ramos-Paz et al., 2019] Ramos-Paz, S., Ornelas-Tellez, F., and Rico-Melgoza, J. J. (2019). Robust nonlinear optimal control for voltage-frequency and active-reactive power regulation in microgrids. In *2019 North American Power Symposium (NAPS)*, pages 1–6, Wichita, KS, USA.

[Ramos-Paz et al.,] Ramos-Paz, S., Ornelas-Tellez, F., Rico-Melgoza, J. J., and Ramos-Yépez, A. A robust control strategy for voltage regulation in electrical distribution networks by means of power electronic converters. In *2020 IEEE International Autumn Meeting on Power, Electronics and Computing (ROPEC)*, Ixtapa, Guerrero, México.

[Rao, 2010] Rao, K. (2010). *Fast Fourier transform : algorithms and applications*. Springer, Dordrecht New York.

[Rasol Jannesar et al., 2019] Rasol Jannesar, M., Sedighi, A., Savaghebi, M., Anvari-Mogjaddam, A., and Guerrero, J. (2019). Optimal probabilistic planning of passive harmonic

filters in distribution networks with high penetration of photovoltaic generation. *Electrical Power and Energy Systems*, 110:332–348.

[Rauf and Khadkikar, 2015] Rauf, A. M. and Khadkikar, V. (2015). An enhanced voltage sag compensation scheme for dynamic voltage restorer. *IEEE Transactions on Industrial Electronics*, 62(5):2683–2692.

[Rodriguez-Lopez et al., 2019] Rodriguez-Lopez, E., Ramos-Paz, S., Rico-Melgoza, J. J., and Otnelas-Tellez, F. (2019). Parametric passive-filter optimization based on the determinant decision diagram. In *2019 IEEE International Autumn Meeting on Power, Electronics and Computing (ROPEC)*, pages 1–6, Ixtapa, México.

[Romero-Aragon et al., 2014] Romero-Aragon, J. C., Sánchez, E. N., and Alanis, A. Y. (2014). Glucose level regulation for diabetes mellitus type 1 patients using fpga neural inverse optimal control. In *2014 IEEE Symposium on Computational Intelligence in Control and Automation (CICA)*, Orlando, Florida, USA.

[Sanchez-Squella et al., 2010] Sanchez-Squella, A., Ortega, R., Grino, R., and Malo, S. (2010). Dynamic energy router. *IEEE Control Systems Magazine*, 30(6):72–80.

[Sangwongwanich and Blaabjerg, 2019] Sangwongwanich, A. and Blaabjerg, F. (2019). Mitigation of interharmonics in pv systems with maximum power point tracking modification. *IEEE Transactions on Power Electronics*, 34(9):8279–8282.

[Sayadi et al., 2018] Sayadi, M., Kosari, A., and Zadeh, P. M. (2018). Robust optimal control for precision improvement of guided gliding vehicle positioning. *IEEE Access*, 6:25797–25815.

[Sctessel et al., 2012] Sctessel, Y., Edwards, C., Fridman, L., and Levant, A. (2012). *Sliding mode control and observation*. Birkhauser, Bassin, Suisse.

[Sepulchre, 1997] Sepulchre, R. (1997). *Constructive nonlinear control*. Springer, New York, NY, USA.

[Sharkh et al., 2014] Sharkh, S., Abusara, M., Orfanoudakis, G., and Hussain, B. (2014). *Power Electronic Converters for Microgrids*. Wiley, West Sussex, United Kingdom.

[Smil, 2017] Smil, V. (2017). *Energy transitions : global and national perspectives*. Praeger, Santa Barbara, California, USA.

[Sontag, 1998] Sontag, E. (1998). *Mathematical control theory : deterministic finite dimensional systems*. Springer, New York.

[Tolstov, 1962] Tolstov, G. (1962). *Fourier Series*. Prentice Hall, Englewood Cliffs, NJ, USA.

[Topputo et al., 2015] Topputo, F., Miani, M., and Bernelli-Zazzera, F. (2015). Optimal selection of the coefficient matrix in state-dependent control methods. *Journal of Guidance, Control, and Dynamics*, 38(5):861–873.

[Verma et al., 2011] Verma, A. K., Singh, B., and Shahani, D. T. (2011). Grid to vehicle and vehicle to grid energy transfer using single-phase bidirectional ac-dc converter and

bidirectional dc-dc converter. In *2011 International Conference on Energy, Automation and Signal*, pages 1–5, Bhubaneswar, India.

[Wang et al., 2015] Wang, B., Shang, J., Dai, N., and Chen, H. (2015). Harmonic reference currents balancing method for delta-connected static synchronous compensator. *Electronics Letters*, 51(25):2134–2136.

[Williams and Hoft, 1991] Williams, S. M. and Hoft, R. G. (1991). Adaptive frequency domain control of pwm switched power line conditioner. *IEEE Transactions on Power Electronics*, 6(4):665–670.

[Winfield et al., 2018] Winfield, M., Shokrzadeh, S., and Jones, A. (2018). Energy policy regime change and advance energy storage: A comparative analysis. *Energy Policy*, 115:572–583.

[Xiao et al., 2015] Xiao, J., Wang, P., and Setyawan, L. (2015). Hierarchical control of hybrid energy storage system in dc microgrids. *IEEE Transactions on Industrial Electronics*, 62(8):4915–4924.

[Xiao-li and Da-qiang, 2012] Xiao-li, C. and Da-qiang, L. (2012). Braking energy recovery for electric traction based on super-capacitor and bidirectional dc-dc converter. *IEEE International Power Electronics and Motion Control Conference*, pages 879–883.

[Xin and Pan, 2012] Xin, M. and Pan, H. (2012). Indirect robust control of spacecraft via optimal control solution. *IEEE Transactions on Aerospace and Electronic Systems*, 48(2):1798–1809.

[Yang et al., 2015] Yang, K., Bollen, M. H. J., and Larsson, E. O. A. (2015). Aggregation and amplification of wind-turbine harmonic emission in a wind park. *IEEE Transactions on Power Delivery*, 30(2):791–799.

[Yeetum and Kinnares, 2019] Yeetum, W. and Kinnares, V. (2019). Parallel active power filter based on source current detection for antiparallel resonance with robustness to parameter variations in power systems. *IEEE Transactions on Industrial Electronics*, 66(2):876–886.

[Zhang et al., 2018a] Zhang, L., Hu, X., and Wang, Z. (2018a). A review of supercapacitor modeling, estimation, and applications: A control/management perspective. *Renewable and Sustainable Energy Reviews*, pages 1868–1878.

[Zhang et al., 2018b] Zhang, L., Hu, X., Wang, Z., Sun, F., and Dorrell, D. G. (2018b). A review of supercapacitor modeling, estimation, and applications: A control/management perspective. *Renewable and Sustainable Energy Reviews*, 81:1868–1878.

[Zhang and Li, 2016] Zhang, Y. and Li, Y. W. (2016). Grid harmonics compensation using high-power pwm converters based on combination approach. *IEEE Journal of Emerging and Selected Topics in Power Electronics*, 4(1):186–197.

[Zhao et al., 2020] Zhao, F., Li, Y., Wang, X., Bai, L., and Liu, T. (2020). Lithium-ion batteries state of charge prediction of electric vehicles using rnns-cnns neural networks. *IEEE Access*, 8:98168–98180.